Northeastern University

Graduate School of Arts and Sciences

Production of High Transverse Momentum π° Mesons
in Interactions of 530 GeV/c proton and π^{-} Beams
on Beryllium and Copper targets.

Author: Carlos M. Yosef

Department: Physics

FERMILAB
LIBRARY

Approved for Thesis Requirements of the Doctor of Philosophy Degree.

G. A. Loew	2-Aug-1990
William J. Fawler	8/2/90
Marie E. Machacek	8/2/90
David Gavelick	8/2/90
Thesis Committee	Date
Department Head	Date

Graduate School Notified of Acceptance

Dean	Date

Copy Deposited in Library

Signed	Date

Gift AAF-5092 Thesis
24839074

Production of High Transverse Momentum π° Mesons
in Interactions of 530 GeV/c Proton and π^- Beams
on Beryllium and Copper Targets.

by

Carlos M. Yosef

ABSTRACT

The inclusive cross section for π° production by 530 GeV/c π^- and proton beams on beryllium and copper targets, have been measured as a function of rapidity (y) and transverse momentum (p_T). The data were collected during the 1987-88 experimental run of experiment E706 at Fermilab, using a finely grained electromagnetic calorimeter and a charged particle spectrometer. The transverse momentum and rapidity ranges covered are $3.25 < p_T < 10$ GeV/c and $-0.7 < y < 0.7$ respectively. The cross section dependence on the atomic number (A) and the beam type has been examined. Results have been compared with leading order QCD calculations.

Submitted in partial fulfillment of the requirements for the degree
of Doctor of Philosophy in Physics in the Graduate School of
Arts and Sciences of Northeastern University, August, 1990

Production of High Transverse Momentum π° Mesons in Interactions of 530 GeV/c Proton and π^- Beams on Beryllium and Copper Targets.

A Dissertation presented

by

Carlos M. Yosef

to

The Department of Physics

In partial fulfillment of the requirements
for the degree of

Doctor of Philosophy

in the field of

Physics

Northeastern University
Boston, Massachusetts

August 1990

* Work supported in part by NSF grant number PHY-851-7612

Northeastern University

Graduate School of Arts and Sciences

Production of High Transverse Momentum π° Mesons
in Interactions of 530 GeV/c proton and π^{-} Beams
on Beryllium and Copper targets.

Author: Carlos M. Yosef

Department: Physics

Approved for Thesis Requirements of the Doctor of Philosophy Degree.

J. Alves	2-Aug-1990
William J Fassler	8/2/90
Marie E Machacek	8/2/90
David Garelick	8/2/90
Thesis Committee	Date
Department Head	Date

ACKNOWLEDGMENTS

The work presented in this thesis has been possible thanks to the many people in the E706 collaboration who, with much dedication and good work, made the experiment a reality. I would like to thank my thesis advisor, Professor George Alverson, and Professors David Garelick, Michael Glaubman and William Faissler for their support and encouragement during my years as a graduate student. I extend my gratitude to my fellow graduate students, post-docs, and the senior collaborators, a hardworking and enjoyable group of people.

I would like to thank George Ginther, Joey Huston, Marek Zielinski, Carl Bromberg, and Robert Miller for their friendship and guidance, always willing to share their experience and knowledge. Much valuable assistance was provided by non physicists. David Cosgrove, Bud Koecher, Bud Dickerson and Jerry Sasek are some of the names in the list of people whose role in the construction and implementation of the experiment is greatfully acknowledged.

My wife Jamie deserves much credit for her patience and support through all these years. I am sure that this long process has been as demanding for her as it has been for me. And last but not least, I want to thank my father for providing me with the tools to get to this point in my life. Finally, I wish to dedicate this work to the memory of my mother.

Table of Contents

1. INTRODUCTION 1

1.1 Hadronic Interactions and QCD 2

1.2 Direct Photons 6

1.3 Nuclear Dependence 11

2. E706 APPARATUS 12

2.1 MW Beamline 13

2.2 Target 18

2.3 The Tracking System 18

2.4 Liquid Argon Calorimeter 22

2.5 The Forward Calorimeter 43

2.6 Data Acquisition System 45

3. TRIGGER DESCRIPTION 47

3.1 Overview 47

3.2 Data Acquisition Controls 53

3.3 Beam and Interaction Definition 54

3.4 Event Selection 60

3.5 Latches 80

4. EVENT RECONSTRUCTION 83

4.1 Discrete Logic Reconstruction 84

4.2 Tracking reconstruction 85

4.3 EMLAC data reconstruction 88

5. TRIGGER PERFORMANCE 94

5.1 Pretrigger 96

5.2 SLOC Trigger 97

5.3 Veto Wall 101

6. DATA ANALYSIS 112

6.1 Event Selection 114

6.2 π° Signal Definition 115

6.3 Monte Carlo 121

6.4 π° Cross Section Calculation 124

7. RESULTS 134

7.1 Cross Section Measurements 134

7.2 Nuclear Dependence 146

7.3 Beam Dependence of the Cross Sections 151

7.4 Comparison with Theoretical Predictions 155

7.5 Summary 162

FIGURE CAPTIONS

1.1) Two-body scattering process. 6

1.2) Leading order subprocess diagrams for direct photon production. 7

1.3) Angular separation of the π° decay photons in the lab system as a function of asymmetry, for a π° energy of 50 GeV. 9

2.1) Layout of the M West spectrometer. 13

2.2) Cherenkov detector response curve for incident 530 GeV/c positive beam. 16

2.3) The Veto Wall planes. The beam travels in the direction indicated by the arrow. Each square corresponds to one scintillation counter. 17

2.4) Layout of the target area. The target consists of twenty 2 mm-thick layers of target material, and is surrounded by an array of SSD planes. 20

2.5) LAC cryostat. The beam is incident from the right. Suspended within the cryostat are the electromagnetic and hadron calorimeters. The cryostat is supported by the gantry. 24

2.6) EMLAC anode boards: (a) R-view and (b) Φ-view. The figures show the geometrical design of the boards. 28

2.7) Summing of signals for each longitudinal section. The sum is performed by ganging corresponding strips together using connector strings. Signals are summed separately for each view. 30

2.8) Readout board for the outer 128 strips in the R-view of the detector. The connector strings used to gang the strips are connected to the readout board. The signals are then taken to the top of the gantry via cables attached to the connectors in the periphery. 31

2.9) Readout board for the strips in the Φ-view of the detector. The connector strings used to gang the strips are connected to the readout board. The signals are then taken to the top of the gantry via cables attached to the connectors in the periphery. 32

2.10) Structure of the EMLAC. The figure shows the final configuration of the calorimeter. 34

2.11) Exploded view of a HALAC cookie. 37

2.12) Triangular readout pattern of a cookie. 38

2.13) LAC Amplifier Module Diagram. 41

2.14) The Forward Calorimeter. 44

2.15) Data acquisition system diagram. 45

3.1) Layout of the Trigger System Counters. The size of the counters has been exagerated with respect of the surrounding spectrometer components. 49

3.2) Beam and Interaction logic definition diagram. 56

3.3) Early/Late filter and Live Interaction definition diagrams. 58

3.4) E706 P_T Summing Card. 62

3.5) E706 Local P_T discriminator module. 63

3.6) E706 Octant P_T Signal Summing. 64

3.7) EMLAC charge collection. 66

3.8) Effects of the image charge on the global p_T signal. The top curve corresponds to the p_T signal from the shower. The middle curve corresponds to the image charge induced in the strips away from the shower. The bottom curve is the sum of the two signals, and corresponds to the global p_T signal as seen by the trigger. 67

3.9) Pretrigger Logic diagram. 72

3.10) LGHI, LGLO and SLOC trigger diagrams. 76

3.11) Final Trigger and Readout logic diagrams. 79

3.12) Trigger reset logic. 80

4.1) Reconstructed vertex Z–position. 89

5.1) Octant 6 Inner Region Pretrigger Efficiency. 98

5.2) LAC outer region pretrigger efficiency. 99

5.3) Octant 8 SLOC trigger efficiency for the lowest threshold set- ting. 100

5.4) Concept of photon directionality. A particle traveling parallel to the beam, such as a muon-bremsstrahlung photon, will have a larger directionality than a photon originating at the target. 105

5.5) Photon P_T distribution vs directionality for events in which the veto wall quadrant, geometrically corresponding to the triggering quadrant, had a signal. A substantial number of photons, including the majority of the high p_T photons, have large directionalities, indication of objects not originated in the target. 106

5.6) Photon P_T distribution vs directionality for events in which the veto wall quadrant corresponding to the triggering quadrant did not have a signal. The band of large directionality photons observed in figure 5.5 is not present here. 107

5.7) Photon arrival time distribution. (a) events in which the veto wall did not have a signal in the quadrant corresponding to the triggering EMLAC quadrant, and (b) events in which the veto wall had a signal in the quadrant corresponding to the triggering quadrant. 108

5.8) Photon arrival time vs directionality for events in which the veto wall had a signal in the quadrant corresponding to the triggering EMLAC quadrant. 109

5.9) Photon arrival time vs directionality for events in which no signals were observed in the veto wall quadrant corresponding to the triggering EMLAC quadrant. 110

6.1) Mass distribution for $\gamma\gamma$ pairs with $P_T > 3.5\,\mathrm{GeV/c}$. The π^0 and η mass peaks are clearly visible. 116

6.2) Radial position dependence of the reconstructed π^0 mass. 118

6.3) Azimuthal distribution of the reconstructed π^0 mass. The dips observed are due to energy losses at the quadrant and octant boundaries. 120

6.4) Asymmetry distribution for (a) $\gamma\gamma$ pairs in the π^0 mass peak region, and (b) $\gamma\gamma$ pairs in the sideband region. A p_T cut of $3.5\,\mathrm{GeV/c}$ was required in both cases. 121

6.5) π^0 asymmetry distribution with background subtracted. A p_T cut of $3\,\mathrm{GeV/c}$ has been imposed. 122

6.6) $M_{\gamma\gamma}$ distribution in the M_{π^0} region for $P_T \geq 3\,GeV/c$. The dotted line includes only $\gamma\gamma$ pairs whose asymmetries are smaller than 0.75. Notice how a good fraction of the background is removed by the asymmetry requirement. 123

7.1) Invariant differential inclusive cross sections per nucleon as a function of p_T for the process $\pi^- + Be \rightarrow \pi^0 + X$ for different rapidity regions. The distributions are successively scaled down by powers of 10. The dashed lines correspond to the function in equation (7.5), integrated over the corresponding rapidity and p_T intervals. 141

7.2) Invariant differential inclusive cross sections per nucleon as a function of p_T for the process $p + Be \rightarrow \pi^0 + X$ for different rapidity regions. The distributions are successively scaled down by powers of 10. The dashed lines correspond to the function in equation (7.5), integrated over the corresponding rapidity and p_T intervals. 142

7.3) Invariant differential inclusive cross section per nucleon as a function of p_T for the process $\pi^- + Cu \rightarrow \pi^0 + X$, for different rapidity regions. The distributions are successively scaled down by powers of 10. The dashed lines correspond to the function in equation (7.5), integrated over the corresponding rapidity and p_T intervals. 143

7.4) Invariant differential inclusive cross section per nucleon as a function of rapidity (y) for the process $\pi^- + Be \rightarrow \pi^0 + X$, for different p_T intervals. The dashed lines correspond to the function in equation (7.5), integrated over the corresponding rapidity and p_T intervals. 144

7.5) Invariant differential inclusive cross section per nucleon as a function of rapidity (y) for the process $p + Be \rightarrow \pi^0 + X$, for different p_T intervals. The dashed lines correspond to the function in equation (7.5), integrated over the corresponding rapidity and p_T intervals. 145

7.6) Invariant differential inclusive cross section per nucleon as a function of p_T for the process $\pi^- + Be \rightarrow \pi^0 + X$ integrated over the interval $-0.7 < y < 0.7$. The dashed line corresponds to the function in equation (7.5), integrated over the corresponding rapidity and p_T intervals. 147

7.7) Invariant differential inclusive cross section per nucleon as a function of p_T for the process $p + Be \rightarrow \pi^0 + X$ integrated over the interval $-0.7 < y < 0.7$. The dashed line corresponds to the function in equation (7.5), integrated over the corresponding rapidity and p_T intervals. 148

7.8) Invariant differential inclusive cross section per nucleon as a function of p_T for the process $\pi^- + Cu \rightarrow \pi^0 + X$, integrated over the interval $-0.7 < y < 0.7$. The dashed line corresponds to the function in equation (7.5), integrated over the corresponding rapidity and p_T intervals. 149

7.9) Invariant differential inclusive cross section per nucleon as a function of p_T for the process $p + Cu \rightarrow \pi^0 + X$, integrated over the interval $-0.7 < y < 0.7$. The dashed line corresponds to the function in equation (7.5), integrated over the corresponding rapidity and p_T intervals. 150

7.10) α as a function of p_T: (a) determined from the ratio $\sigma(\pi^- + Be)/\sigma(\pi^- + Cu)$; (b) determined from the ratio $\sigma(p+Be)/\sigma(p+Cu)$. 152

7.11) Beam dependence of the cross section as a function of p_T, determined from the ratio $\sigma(\pi^- + Be)/\sigma(p+Be)$. The cross sections were measured over the interval $-0.7 < y < 0.7$. Superimposed is the ratio of the fits for the two processes. 154

7.12) Comparison of π^0 data from interactions between π^- and beryllium with QCD predictions. Owens set 1 with $\Lambda = 200$ GeV was used, with $Q^2 = P_T^2$ and $Q^2 = 0.25P_T^2$. 156

7.13) Comparison of π^0 data from interactions between protons and beryllium with QCD predictions. Duke–Owens set 1 with $\Lambda = 200$ GeV was used, with $Q^2 = P_T^2$ and $Q^2 = 0.25P_T^2$. 157

7.14) Comparison of π^0 data from interactions between π^- and beryllium with QCD predictions. Owens set 1 with $\Lambda = 200$ GeV was used, with $Q^2 = P_T^2$ and $Q^2 = 0.25P_T^2$. A value of 0.4 GeV for k_T has been used to include smearing contributions. 158

7.15) Comparison of π^0 data from interactions between protons and beryllium with QCD predictions. Duke–Owens set 1 with $\Lambda = 200$ GeV was used, with $Q^2 = P_T^2$ and $Q^2 = 0.25P_T^2$. A value of 0.4 GeV for k_T has been used to include smearing contributions. 159

7.16) Comparison of π° data from interactions between π^- and beryl- 160
lium with QCD predictions as a function of rapidity. Owens set 1 with $\Lambda = 200\,\mathrm{GeV}$ was used, with $Q^2 = P_T^2$ and $Q^2 = 0.25P_T^2$. The solid dots are the data points and the triangles are the values from QCD predictions.

7.17) Comparisc n of π° data from interactions between protons and 161
beryllium with QCD predictions as a function of rapidity. Duke–Owens set 1 with $\Lambda = 200\,\mathrm{GeV}$ was used, with $Q^2 = P_T^2$ and $Q^2 = 0.25P_T^2$. The solid dots are the data points and the triangles are the values from QCD predictions.

TABLE CAPTIONS

2.1: Beam Composition. 15

2.2: Target parameters. 19

3.1: Trigger threshold settings. 74

5.1: Pretrigger efficiency parameters. 97

5.2: SLOC Trigger Efficiency Parameters, Threshold = 4.2 GeV/c 101

5.3: SLOC Trigger Efficiency Parameters, Threshold = 3.6 GeV/c 102

5.4: SLOC Trigger Efficiency Parameters, Threshold = 3.0 GeV/c 102

6.1: Breakdown of the E706 data sample. 112

6.2: Summary of events remaining after applying the rejection cuts. 115

6.3: EMLAC geometric acceptance for π°s as a function of p_T and rapidity. 127

6.4: EMLAC reconstruction efficiency for π°s as a function of photon multiplicity. 128

6.5: Process dependent parameters used in the evaluation of the cross sections. 132

7.1: P_T intervals used in the cross section measurement. 135

7.2: Invariant differential inclusive cross section per nucleon for the process $\pi^- + \mathrm{Be} \rightarrow \pi^\circ + \mathrm{X}$. The units are pbarn/GeV^2/nucleon. 136

7.3: Invariant differential inclusive cross section per nucleon for the process $\mathrm{p} + \mathrm{Be} \rightarrow \pi^\circ + \mathrm{X}$. The units are pbarn/GeV^2/nucleon. 137

7.4: Invariant differential inclusive cross section per nucleon for the process $\pi^- + \mathrm{Cu} \rightarrow \pi^\circ + \mathrm{X}$. The units are pbarn/GeV^2/nucleon. 138

7.5: Invariant differential inclusive cross section per nucleon for the process $\mathrm{p} + \mathrm{Cu} \rightarrow \pi^\circ + \mathrm{X}$. The units are pbarn/GeV^2/nucleon. 138

7.6: Parameters for the fits of the experimental cross sections. 139

7.7: π° mass as a function of rapidity. 146

7.8: α dependence on p_T, obtained using cross sections integrated and averaged over the range $-0.7 < y < 0.7$. 153

7.9: α dependence on rapidity for different p_T regions. 153

1. INTRODUCTION

This thesis is devoted to the study of the inclusive production of large transverse momentum (p_T) π°'s, in interactions between 530 GeV/c proton and π^- beams and beryllium and copper targets. The data were collected during the 1987-88 run of experiment E706 at Fermilab. E706 is a second generation fixed target experiment, designed to study the production of high transverse momentum direct photons and their associated jets in hadronic interactions. One of the challenges in the extraction of the direct photon signal is the substantial background from the decays $\pi^\circ \rightarrow \gamma\gamma$ and $\eta \rightarrow \gamma\gamma$. The purpose of this thesis is to measure the π° production cross sections for the processes mentioned above and make comparisons with perturbative QCD predictions, to assess the background contributions from π°s to the direct photon signal, and as an indicator of the performance of the new spectrometer.

The remainder of this chapter will be dedicated to the physics motivation for this work. A description of the E706 spectrometer is given in chapter 2. Chapter 3 presents the experimental trigger system used in the on-line selection of events of interest. The process of event reconstruction is described in chapter 4, while the performance of the trigger is presented in chapter 5. The last two chapters are dedicated to the analysis of the data collected: the process of event selection is discussed in chapter 6 and the final results and conclusions are given in chapter 7.

The coordinates used in the description of the experiment are given relative to a right-handed system, with the Z-direction along the direction of incidence of the beam, the X-axis horizontal, and the Y-axis vertical with the positive direction pointing upwards. The terms upstream and downstream are relative to the direction of the incoming beam, downstream meaning farther along in the direction of incidence.

1.1 Hadronic Interactions and QCD

Experimental results have shown that hadronic interactions have to be considered in terms of interactions between hadron constituents. Hadrons are built from fundamental point-like fermions called quarks, bound together inside the hadron by strong quark-quark forces. Deep inelastic scattering of high energy leptons by nucleon targets, showed that the complicated process of multiple hadron production could be interpreted in terms of the elastic scattering of the lepton by a quasi-free, pointlike constituent, or parton, inside the nucleon. Later it was determined that these partons could be identified with the quarks and the boson mediating the quark-quark interactions, called the gluon.

The quark content of some hadrons such as the Δ^{++}, in which three identical $J = 1/2$ quarks in their ground state are combined in a symmetric state, led to the introduction of a new quantum number, the color charge, in order to satisfy Fermi statistics. It is supposed that quarks come in three colors, with three corresponding anticolors carried by the antiquarks. To avoid the proliferation of the number of states, in agreement with the observations, it is asserted that all particle-states observed, such as hadrons, are colorless. A colorless combination of three quarks in

a bound state is called a "baryon", while a "meson" is defined as the bound state of a quark-antiquark pair with zero net color.

To describe the strong interactions, a theory has emerged in analogy to Quantum Electrodynamics (QED), the theory of electromagnetic interactions. The quantum field theory of quark interactions is called Quantum Chromodynamics (QCD). In QCD, the strong interactions are mediated by a boson, the gluon, just as in QED the interactions are mediated by photons. But unlike the photon which has no electric charge, gluons carry color charge and therefore they can interact with each other.

The coupling for strong interactions is given as a function of the momentum transfer (Q^2) characteristic of the process considered. This "running coupling" $\alpha_s\left(Q^2\right)$, expanded to first order in terms of $\ln Q^2$ (leading-log approximation), is given as[1]

$$\alpha_s = \frac{12\pi}{\left(33 - 2n_f\right)\ln\left(Q^2/\Lambda^2\right)} \tag{1.1}$$

where n_f is the number of quark flavors, and Λ is a parameter that sets the scale for the Q^2 dependence. The value of Λ is not predicted by the theory and is to be obtained from experimental measurements; it is expected to have a value between 0.1 and 0.5 GeV.

It can be seen from equation (1.1) that the coupling α_s becomes large at large distances, which presumably gives rise to quark confinement. Thus, if enough energy is given to a quark to knock it out of its bound state, as the quark separates the coupling increases, to the point where there is enough potential energy to create a new quark-antiquark pair, a process that will continue until the available energy has degraded. In this way, one or more clusters of quarks and gluons bound in states

of zero net color are generated, a process known as "hadronization". Equation (1.1) also shows that α_s decreases with increasing Q^2. Thus, at large values of Q^2 the coupling becomes weak and the quarks behave as quasi-free particles, a feature referred to as *asymptoticfreedom*. This feature allows for the use of perturbative techniques in the calculation of, for instance, the hard scattering of the hadron constituents in high p_T processes.

Experimentally, we deal with the interactions between beams and targets which consist of hadrons and not the isolated partons. Therefore, we need to calculate the momentum distribution of the partons inside the hadrons, something that requires the knowledge of the hadron wave functions in regions where the perturbation techniques are not applicable. This wave functions can not be calculated nonperturbatively, at present, and a convolution between what can be calculated perturbatively and what can be measured experimentally is necessary.

In the parton model the hard scattering is described by the lowest order subprocess which, for high-p_T particle, jet, or single photon production, corresponds to the two-body scattering process shown in figure 1.1, where A and B are the incident hadrons, C is the specific product of the reaction, and X is anything else produced (a process of the form A + B → C + X, is termed an "inclusive" reaction[2]). The invariant inclusive cross section for this process in the leading-log approximation, is given as (ref 1)

$$E_C \frac{d\sigma}{d^3p_C} = \sum_{abcd} \int dx_a dx_b dz_c \; G_{a/A}(x_a, Q^2) G_{b/B}(x_b, Q^2) D_{C/c}(z_c, Q^2) \frac{\hat{s}}{z_c^2 \pi} \frac{d\sigma}{d\hat{t}}(ab \to cd) \delta(\hat{s} + \hat{t} + \hat{u}) \tag{1.2}$$

The sum in equation (1.2) is performed over all possible constituent scatterings.

Here, x_i is the fraction of the momentum of hadron I carried by parton i, and $G_{i/I}(x_i, Q^2)$ is the parton distribution function, which represents the probability of finding parton i in hadron I with momentum fraction between x and $x + dx$. $D_{I/i}$ is the fragmentation function. It gives the probability of obtaining a hadron I from the the hadronization of parton i, carrying a momentum fraction between z and $z + dz$ of the initial parton momentum. The distribution and fragmentation functions must be determined experimentally. $d\sigma/d\hat{t}$ is the differential cross section for the two-body parton scattering subprocess, and $\hat{s}$, $\hat{t}$, and $\hat{u}$ are the Mandelstam variables defined in terms of the parton four momentum p_i

$$\begin{aligned} \hat{s} &= (p_a + p_b)^2 \\ \hat{t} &= (p_a - p_c)^2 \\ \hat{u} &= (p_b - p_c)^2 \end{aligned} \tag{1.3}$$

with the constraint

$$\hat{s} + \hat{t} + \hat{u} = 0$$

for the case of massless two-body-scattering.

The Q^2 dependence of the distribution and fragmentation functions arise from the inclusion of radiative corrections due to collinear gluon emission, which introduces mass singularities that are absorbed into these functions. The fact that the functions no longer scale with x, as predicted by the parton model, but depend in Q^2 as well, is termed "scaling violations".

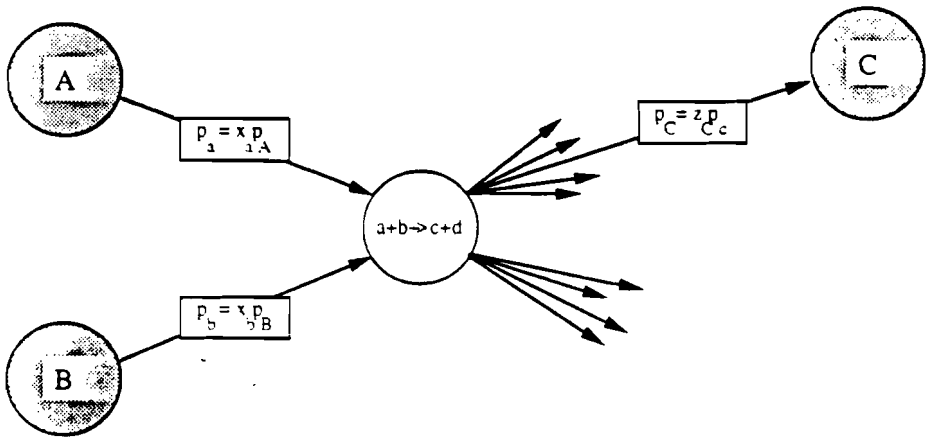

Figure 1.1: Two-body scattering process.

1.2 Direct Photons

The investigation of direct photon production in hadronic collisions has provided an important tool in the study of parton-parton scattering. Several theoretical and experimental reviews on the subject can be found that provide excellent summaries.[3–6]

Direct photons are photons that originate from the primary parton-parton interaction and not from the decay of other particles. In contrast to the gluons and quarks which fragment into hadrons of reduced p_T, direct photons emerge from the parton scattering as free particles carrying away the momentum from the primary interaction. Therefore, it is not necessary to unfold a complicated fragmentation process before getting at the fundamental quark and gluon dynamics, providing a very appealing method of studying QCD. To leading order, only two

subprocesses contribute to direct photon production: gluon-Compton scattering and quark-antiquark annihilation (figure 1.2). From this figure, we can see that when a direct photon appears in the final state, either a gluon initiated the hard scatter (Compton process), or a gluon accompanies the photon (annihilation process). Thus, once the contributions from these two processes can be isolated, direct photon production allows to extract information on both gluon fragmentation and on the gluon structure of hadrons.

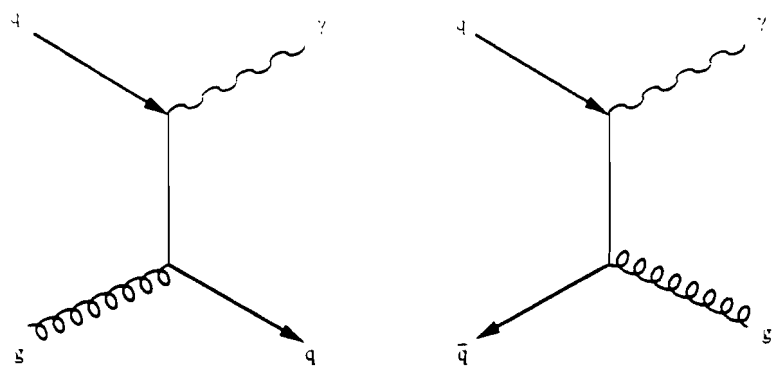

Figure 1.2: Leading order subprocess diagrams for direct photon production

The cross section for the process $A + B \rightarrow \gamma + X$, can be readily obtained from equation (1.2), after removing the fragmentation related terms, i.e.,

$$E_\gamma \frac{d\sigma}{d^3 p_\gamma} = \sum_{abd} \int dx_a dx_b \; G_{a/A}(x_a, Q^2) G_{b/B}(x_b, Q^2) \frac{\hat{s}}{\pi} \frac{d\sigma}{d\hat{t}}(ab \rightarrow \gamma d) \delta(\hat{s} + \hat{t} + \hat{u}) \tag{1.4}$$

The differential cross sections for the two leading order processes mentioned above are (ref 1)

$$\frac{d\sigma}{d\hat{t}}(gq \rightarrow \gamma q) = -\frac{\pi\alpha\alpha_s}{3\hat{s}^2} e_q^2 \frac{\hat{u}^2 + \hat{s}^2}{\hat{s}\hat{u}} \tag{1.5}$$

$$\frac{d\sigma}{d\hat{t}}(q\overline{q} \rightarrow \gamma g) = \frac{8\pi\alpha\alpha_s}{9\hat{s}^2} e_q^2 \frac{\hat{u}^2 + \hat{t}^2}{\hat{u}\hat{t}} \tag{1.6}$$

Experimental Considerations

The two major problems encountered in the study of direct photon production are: first, the cross section is reduced by approximately α/α_s, greatly reducing the yield relative to jet production (a factor of ~ 30 for analog diagrams at the p_T values of interest). The relative yield is reduced even further by the larger number of contributing diagrams in the jet case. Second, the extraction of the direct photon signal is complicated by the presence of substantial backgrounds.

A major contribution to the background to the direct photon signal arises from the decay of the π° meson into photon pairs. The misidentification of a π° as a direct photon can be examined in terms of the energy asymmetry for the two decay photons. The energy asymmetry A is defined as

$$A = \frac{|E_1 - E_2|}{E_1 + E_2} \tag{1.7}$$

where E_1 and E_2 are the photon energies. This quantity is approximately equal to $|\cos\theta^*|$, where θ^* is the angle between the line of flight of the π° and the direction of the decay photons, measured in the rest frame of the π°. A scalar particle like the π° (spin 0) decays isotropically and the asymmetry distribution should be flat from 0 to 1, assuming there is perfect detection. However, as shown in

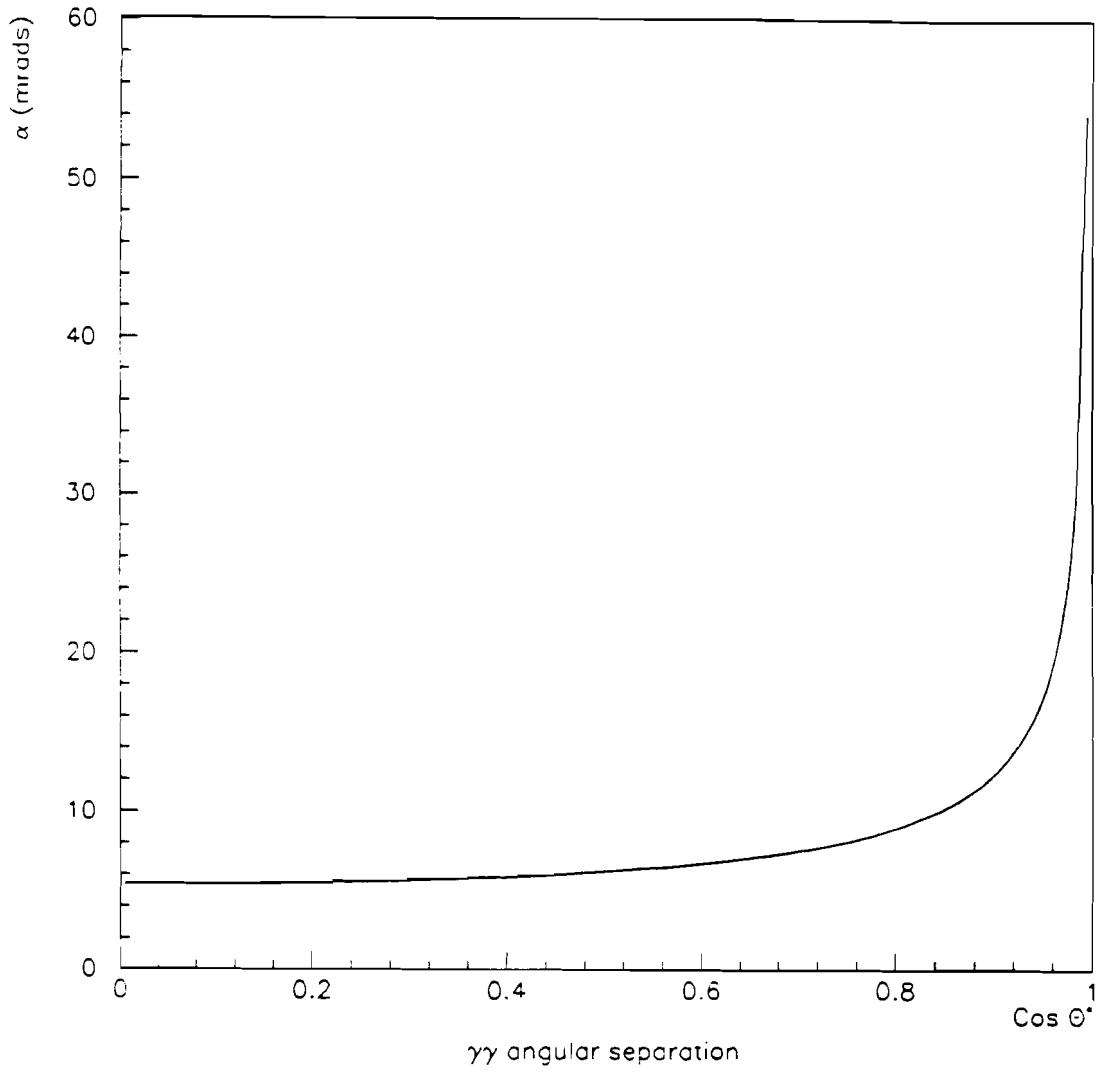

Figure 1.3: Angular separation of the π° decay photons in the lab system as a function of asymmetry, for a π° energy of 50 GeV.

figure 1.3, the angular separation of the two decay photons in the laboratory frame increases very rapidly at high asymmetries. Because detectors are limited in size, soft photons tend to be lost in highly asymmetric decays due to limited acceptance of the detectors. Even if both decay photons hit the detector, the energy of the

soft photon might be too low to be properly reconstructed and the photon is lost anyway. For asymmetries near zero, the angular separation between the two photons reaches its minimum, and there may be a loss of the π° due to the two photons coalescing. The background to the direct photon signal due to these losses of π°s, can be well calculated and subtracted once the experimental measurements of the π° cross section and asymmetry distributions have been performed.

A p_T-like kinematic variable commonly used in the measurement of the cross sections is the longitudinal rapidity. For a particle with energy E and longitudinal momentum component p_L, the rapidity y is defined as

$$y = \frac{1}{2}\ln\frac{E+p_L}{E-p_L} \tag{1.8}$$

For very high energy cases when the mass is negligible, the rapidity can be approximated to the pseudorapidity η defined by

$$\eta = -\ln\tan\theta/2 \tag{1.9}$$

where θ is the production angle. The value of the rapidity in some given Lorentz frame, say the LAB frame, is related to the value of the rapidity in another Lorentz frame, for example the CM frame, through the relation (for a boost along the direction of incidence of the beam)

$$y_{LAB} = y_{CM} + \frac{1}{2}\ln\left(\frac{1-\beta}{1+\beta}\right) \tag{1.10}$$

It can be seen from equation (1.10) that the shape of the invariant distribution $d\sigma/dy$ will be independent of the Lorentz frame.

1.3 Nuclear Dependence

The use of different nuclear targets in E706 allows to study nuclear effects. The ratio of the cross-sections per nucleus for two different targets, for example beryllium and copper, can be parametrized as

$$\frac{\sigma(Be)}{\sigma(Cu)} = \left(\frac{A_{Be}}{A_{Cu}}\right)^{\alpha} \tag{1.11}$$

where A_b is the atomic number of target material b. Any deviation of α from 1, would indicate some form of coherent behavior among the nucleons inside the nucleus.

In this analysis, the performance of the experimental trigger will be presented, cross sections will be measured for the production of π°s by 530 GeV/c proton and π^{-} incident on copper and beryllium targets. Comparison of the cross sections for the two different beam types will be made, and a measurement of the nuclear dependence will be performed for the two targets. The results from the data will be compared to theoretical QCD predictions.

2. E706 APPARATUS

The spectrometer for experiment E706 is located in the MW9 experimental hall at the end of the Meson West (MW) beamline at FNAL. The spectrometer consists of several detectors designed and built by the different collaborating institutions on the experiment. The different devices in the spectrometer were designed to handle the high interaction rates necessary to collect a large enough amount of data to be able to extract useful information about the relatively small direct photon cross section. The main components of the spectrometer, shown in fig 2.1, are:

- a set of silicon strip detector (SSD) planes,
- an analysis magnet,
- a set of multiwire proportional chambers (PWCs),
- a liquid argon calorimeter (LAC) with both electromagnetic and hadronic sections, and
- a forward calorimeter.

Downstream of the forward calorimeter is a muon system consisting of a toroidal magnet and proportional wire chambers provided by experiment E672.

The experiment was designed to allow a detailed examination of the entire event. The charged particle spectrometer measures the momenta of all charged

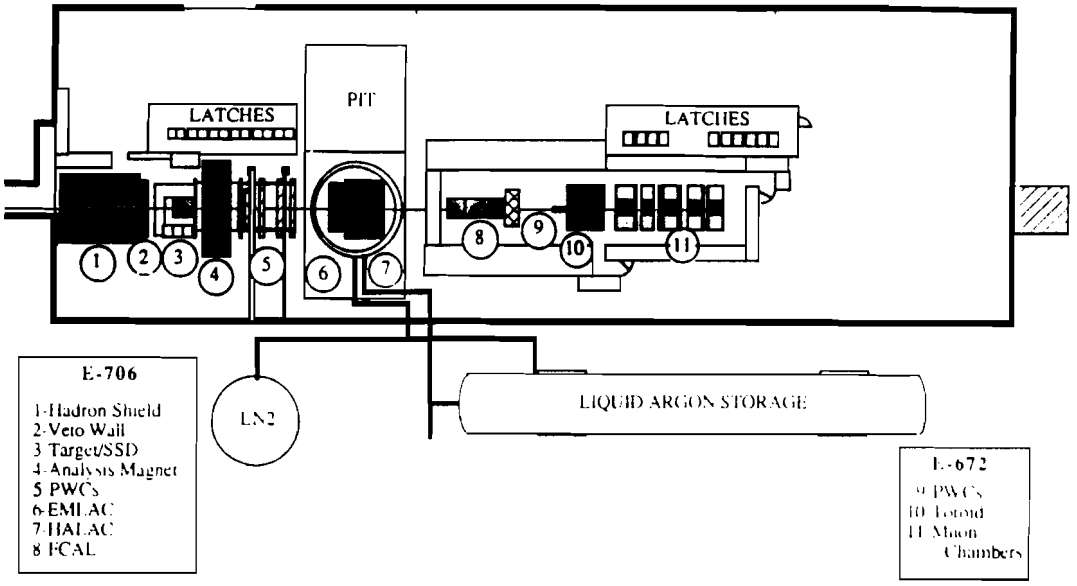

Figure 2.1: Layout of the M West spectrometer.

particles while the photon energies and positions are measured by the electromagnetic calorimeter. The hadron calorimeter measures the positions and energies of neutral hadrons in addition to giving a measurement of charged hadron energies and the forward calorimeter covers the forward angular region not covered by the LAC. The different components of the spectrometer will be described in the following sections.

2.1 MW Beamline

The MW beamline was designed and constructed to transport high intensity secondary beams of positive or negative polarities, with energies of up to the primary beam energy. The secondary beam was produced by an 800 GeV/c primary proton

beam interacting in a 0.75 interaction length aluminum primary target. The protons in the primary beam occurred in very narrow time buckets or intervals ($\sim$1 ns wide) during 23 sec long spills. The buckets were spaced 19.7 ns apart and there was a 34 sec interval between spills. During the 1987-1988 experimental run, secondary 530 GeV/c negative and positive beams were used.

The secondary beamline consists of a momentum selecting dipole pair at the production target followed by a double focus beam transport system. During the experimental run the average buckets had a 10% chance of occupancy by a beam particle, with 2% chance of double occupancy in the secondary beam. The parallel section of the beam contains a differential Cherenkov counter used for tagging the different beam particle types (π, K, p). A muon flux along the beamline, produced mainly by meson decay near the primary target, was reduced by deflecting the muons using "spoiler" magnets. The beamline also contains a dipole magnet used to sweep the beam in the vertical direction during the calibration of the calorimeters. A hadron shield is located at the end of the beamline immediately upstream of the experimental target to attenuate the halo of hadrons parallel to the beam. Following the hadron shield is a veto wall which consists of two planes of scintillation counters. The veto wall is used to veto muons parallel to the beam and any interaction occurring upstream of the experimental target.

Cherenkov Detector

The Cherenkov detector[7] is a gas-filled differential counter located in the 67 m-long parallel section of the MW-beamline approximately 98 m upstream of the E706 target. The gas used as the radiator in the detector is welding grade helium gas. The Cherenkov detector has a total radiator length of 42.1 m and a Cherenkov angle

of 4.998 mrad. The entrance and exit windows of this detector are 0.25 mm thick titanium foils. During the experimental run, one 10.16 cm × 10.16 cm scintillation counter was placed at each end of the Cherenkov counter to determine if the beam particle had passed through the entire detector. A long focal length mirror (32.4 m) was used to focus the light, and two different size rings of six photomultipliers were used to collect it. The inner ring of photomultipliers was used as the coincidence channel and the larger ring was used as the anticoincidence or vetoing channel.

The index of refraction inside the detector was manipulated by changing the helium gas pressure. During the run the operating pressure was set between 4 and 7 psia and was read remotely by two pressure transducers with an accuracy of ±0.01 psia. The helium pressure in the Cherenkov detector was generally set to allow tagging of K^- (π^+) in the negative (positive) beam. Figure 2.2 shows the Cherenkov response curve as a function of the helium gas pressure for positive beam. The horizontal axis corresponds to the gas pressure and the vertical axis indicates the number of coincidences in the Cherenkov detector normalized to total beam. The efficiency for tagging K^-s was ~ 50% with less than 5% contamination from π^-s. For the tagging of π^+s the efficiency was 80-85% with about 8% K^+ contamination and negligible contamination from protons (see ref 7). The beam composition for both beam polarities was measured using response curves such as those in fig 2.2, and is listed in table 2.1.

Negative Beam			Positive Beam		
$\pi^-(\%)$	$K^-(\%)$	$\bar{p}(\%)$	$\pi^+(\%)$	$K^+(\%)$	$p(\%)$
96.9 ± 0.2	2.9 ± 0.2	0.2 ± 0.01	7.2 ± 0.1	1.7 ± 0.1	91.2 ± 0.1

Table 2.1: Beam Composition.

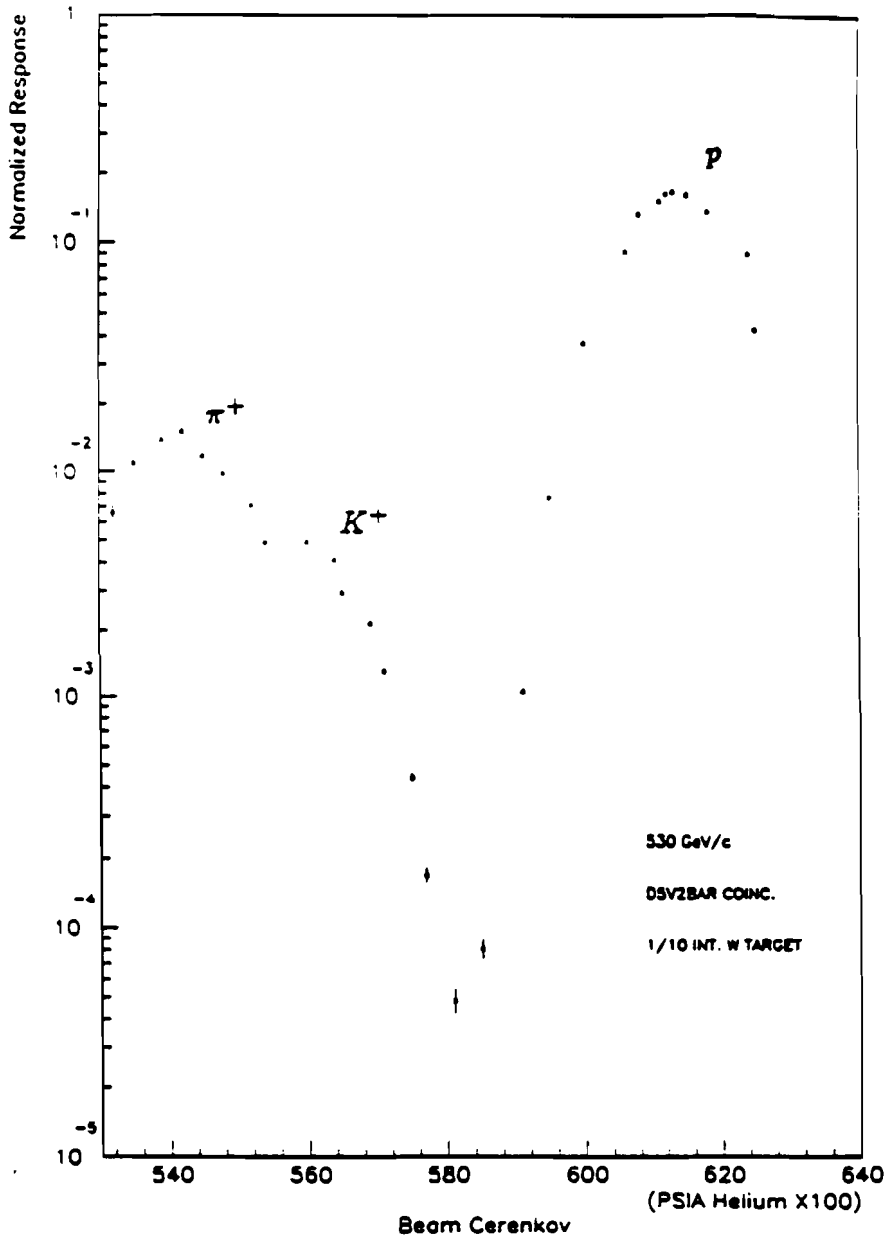

Figure 2.2: Cherenkov detector response curve for incident 530 GeV/c positive beam.

The Veto Wall

The Veto Wall (VW) consists of two overlapping planes of scintillation counters and is located immediately downstream of the beam hadron shield. Each plane has

32 50 cm × 50 cm counters supported by an aluminum frame, and is subdivided into quadrants. A relative offset of 10 cm was introduced between the quadrants in each wall, leaving a 10 cm × 10 cm hole which is centered on the beamline (see fig. 2.3). The offset was introduced so that gaps between counters in one plane were covered by counters in the other plane.

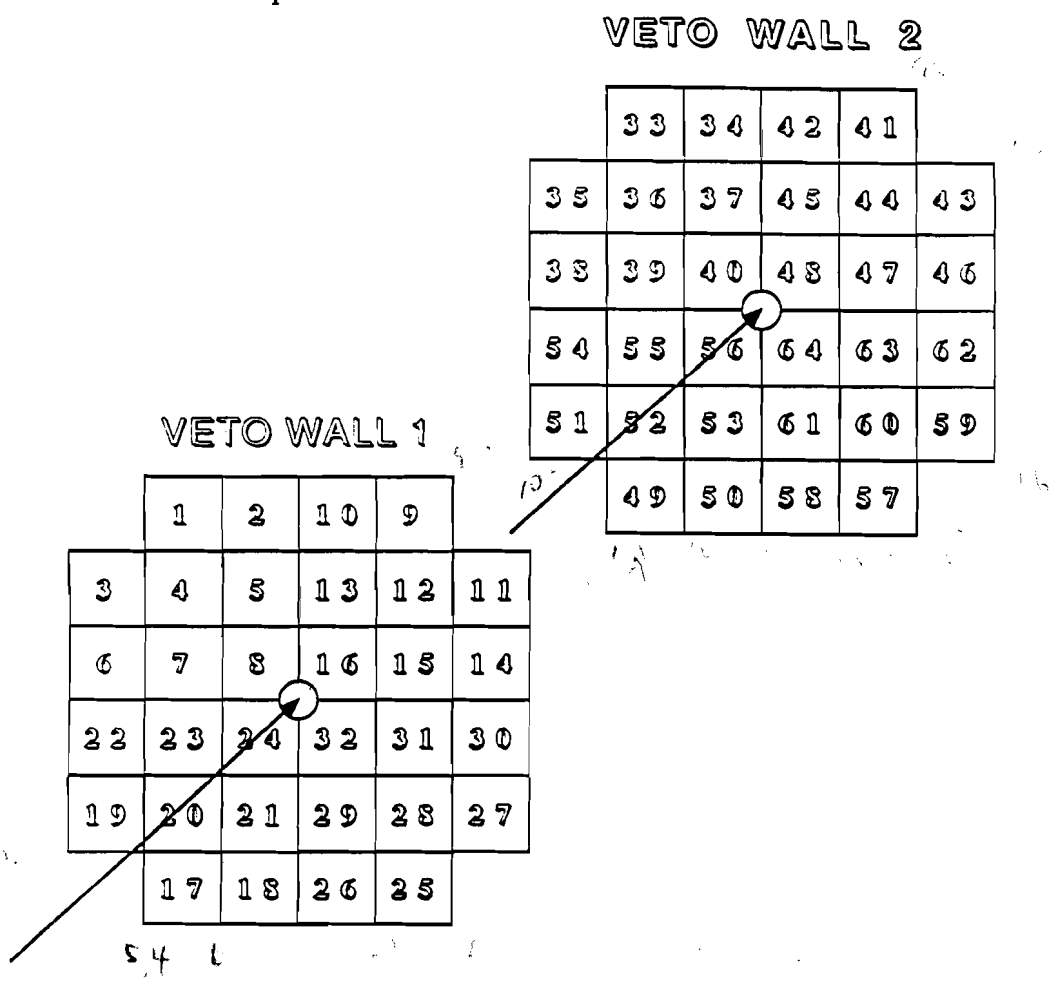

Figure 2.3: The Veto Wall planes. The beam travels in the direction indicated by the arrow. Each square corresponds to one scintillation counter.

The VW is used to detect particles (mainly muons not swept out by the upstream spoiler magnets) that travel parallel to the beam; high energy muons can

produce bremsstrahlung photons of energies high enough to create fake high transverse momentum signals in the electromagnetic calorimeter. A signal indicating a coincidence between counters in the two walls was used to veto the event at the trigger selection level (see chapter 3).

2.2 Target

Copper, beryllium and carbon nuclear targets were used. Nuclear targets have the virtue of being compact and easy to handle. For the target selection, considerations of the interaction and radiation lengths were taken into account. To minimize photon conversions in the target, long radiation lengths are necessary. In addition, targets with long interaction lengths are required in order to minimize secondary interactions. Because of the scaling properties of both the interaction and radiation lengths as functions of the atomic number Z, materials with relatively low Z are desirable.

During most of the data run, the target consisted of twenty 2 mm-thick beryllium segments separated by 1.55 mm gaps. During a portion of the run, two 0.8 mm-thick copper segments separated by a 1.55 mm gap, followed by a 3.2 mm gap, were positioned in front of the beryllium stack. Table 2.2 lists some of the properties of the target materials.

2.3 The Tracking System

The E706 tracking system consists of a set of silicon strip detectors, an analysis magnet, and a set of proportional wire chambers. This system was used primarily to measure the momenta of charged particles and to locate the interaction vertices.

Parameters	Be	C	Cu
Length(cm)	4.0	4.0	0.16
Atomic Number	9.01	12.01	63.54
Density (g/cm^3)	1.85	1.79	8.96
Radiation Length(%)	11.33	21.28	11.19
π interaction length(%)	6.90	7.78	0.83
p interaction length(%)	9.24	10.24	1.03
K interaction length(%)	6.25	7.15	0.77

Table 2.2: Target parameters.

The proportional wire chambers, combined with the electromagnetic calorimeter, were also used for electron identification.

Silicon Strip Detectors

The design of the Silicon Strip Detectors (SSDs) was based on the following considerations: (1) the detector must be compact in size along the beam axis; (2) The angular resolution of the detector must match that of the PWCs downstream of the magnet; (3) the detector must be able to resolve track reconstruction ambiguities in the PWCs resulting from very high track densities; (4) the SSD system is required to differentiate primary and secondary vertices.

The target is surrounded by an array of SSDs as shown in figure 2.4. The SSDs consist of 7 modules, each containing one vertical (X) plane and one horizontal (Y) plane, with a total of 7,120 active strips.[8] All SSDs have a 50 μm pitch and a thickness of 250 to 300 μm. Three of the X-Y modules, consisting of 3 cm $\times$ 3 cm wafers, are located before the target, and are used to measure the trajectory of the beam particle. The other four modules, one made of 3 cm $\times$ 3 cm wafers and

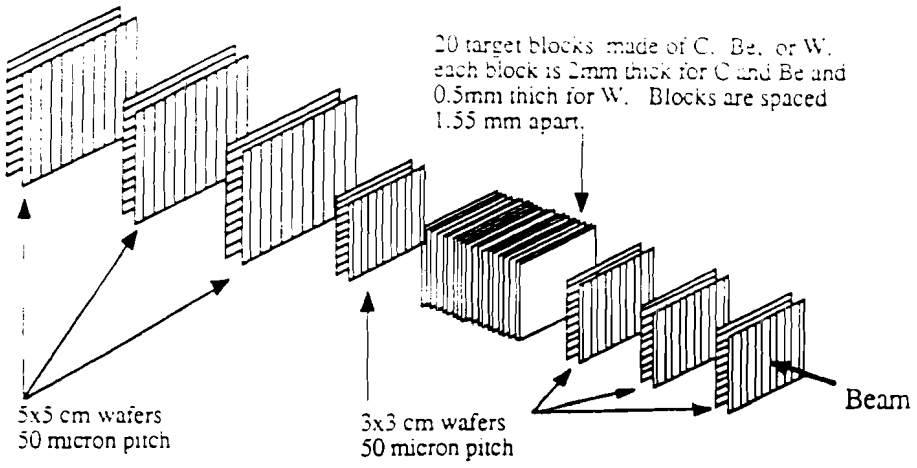

Figure 2.4: Layout of the target area. The target consists of twenty 2 mm-thick layers of target material, and is surrounded by an array of SSD planes.

the other three made of 5 cm × 5 cm wafers, are positioned after the target. They are used to determine the vertices and the trajectories of the produced charged particles in front of the analysis magnet and, in conjunction with the proportional wire chambers, they are used to measure the momenta of those particles. The signals from the strips in the SSDs are sent to charge-sensitive preamplifiers whose output is amplified again and then discriminated. The wafers are mounted on a series of two fanout boards which disperse the traces connected to the silicon strips,

thus allowing for room to mount the preamplifiers for all channels.

Analysis Magnet

The analysis magnet (MW9AN) is a dipole magnet used to provide a transverse momentum kick for all charged particles within its geometrical acceptance. MW9AN is located between the silicon strip detectors and the proportional wire chambers. The magnet aperture is 91.44 cm high, 127.0 cm wide and 167.64 cm long. To reduce the fringe field, a mirror plate was installed at each end (upstream and downstream) of the magnet. The acceptance of the magnet is defined by the holes in the mirror plates. The upstream plate hole is 35.56 cm $\times$ 25.4 cm and the downstream plate hole is 127.00 cm $\times$ 91.44 cm. The magnetic field inside the magnet aperture was measured using the ZIPTRAK system developed at Fermilab.[9] The measurements were performed using operating currents of 700, 1400 and 2100 amps. Based on the results from the measurements it was decided to use an operating current of 1050 amps to produce a transverse momentum kick of 450 MeV/c.

Proportional Wire Chambers

The proportional wire chambers (PWCs) consist of four independent modules, each of which contains a set of four (X,Y,U and V) anode planes. The wires in the U-plane are tilted at 37° and in the V-plane at $-53°$ relative to the vertical axis. There are a total of 13,440 channels in the four chambers.[10] The wires in the anode planes are gold-plated tungsten, 0.02 mm in diameter, and have a pitch of 2.5 mm. Each anode plane has one graphite coated mylar cathode plane on each side. The separation between the anode and the cathode planes is 0.57 cm. The graphite coating in the cathode planes is masked into segments so that the high voltage can be set independently in different regions of the chambers such as the

central region where for high intensity beam it is important to be able to desensitize the anode wires.

The four PWCs are dimensioned to maintain an approximately constant acceptance. Module one is 1.63 m × 1.22 m, modules two and three are both 2.03 m × 2.03 m, and module four is 2.44 m × 2.44 m. The gas mixture in the PWCs is 18% isobutane, 2.2% isopropyl alcohol, 0.1% freon, and the balance (79.7%) argon. The electronic readout system used for the SSDs and the PWCs systems is similar differing only in the preamplifier boards. The common readout system was provided by Nanometrics Systems, Inc.* The Nanometric modules were housed in CAMAC[11] crates and read out via a serial CAMAC highway by a PDP 11/34.

2.4 Liquid Argon Calorimeter

The Liquid Argon Calorimeter (LAC) consists of separate electromagnetic and hadronic sampling sections, mechanically independent of each other, which reside in a common cryostat. The two detectors are used to measure the energy and position of photons, electrons and hadrons. The electromagnetic section of the LAC was also used in the trigger selection of events with high transverse momentum electromagnetic showers. A brief description of the LAC system is given in the following sections. A complete description of the LAC system can be found in the Ph.D. dissertation by W. DeSoi of the University of Rochester.[12]

Cryostat and Gantry

The LAC system, shown in figure 2.5, is supported by a gantry structure made of steel I-beams. The cryostat is an upright cylinder, 5.2 m in diameter and 9 m high.

* The nanometric system is described in detail in the Nanometric Systems documentation.

The cryostat consists of a cover plate and a "top hat" composed of carbon steel attached to the top of the gantry, and a dewar composed of rolled 304 stainless steel. The two calorimeters are suspended from eight steel rods attached to the cover plate; the rods are monitored with strain gauges to ensure a reasonable load distribution.

The gantry rests on a set of Hillman rollers which allow it to move perpendicular to the beamline. A pit approximately 11 m deep, in which the steel dewar can be stored (see figure 2.1), was built into the building foundation west of the LAC beamline position. This feature is essential in the assembly of the LAC since once the calorimeters are attached to the gantry, it is necessary to be able to lower or raise the dewar around them. To seal the cryostat the dewar is bolted to a flange in the "top hat", with an O-ring seal providing vacuum integrity.

The wall of the dewar enclosing the calorimeters is 1.43 cm thick. It is covered by approximately 25 cm of fiberglass and polyurethane foam for thermal insulation. The insulation is equipped with a system of plastic tubes that supply dry nitrogen gas to inhibit condensation of water that might otherwise destroy the integrity of the insulation. The dewar has a circular window on the upstream side for the beam to pass through. The window hole has a diameter of $\sim$ 5 cm and is covered with 3.1 mm thick stainless steel. The purpose of this window is to reduce the amount of passive material to minimize the number of secondary interactions as the beam passes through the wall of the cryostat.

In addition to the calorimeters, two more vessels were placed inside the cryostat. The purpose of the two vessels is to replace the liquid argon with lower density material in order to reduce unwanted interactions. One of the vessels has 1.6 mm

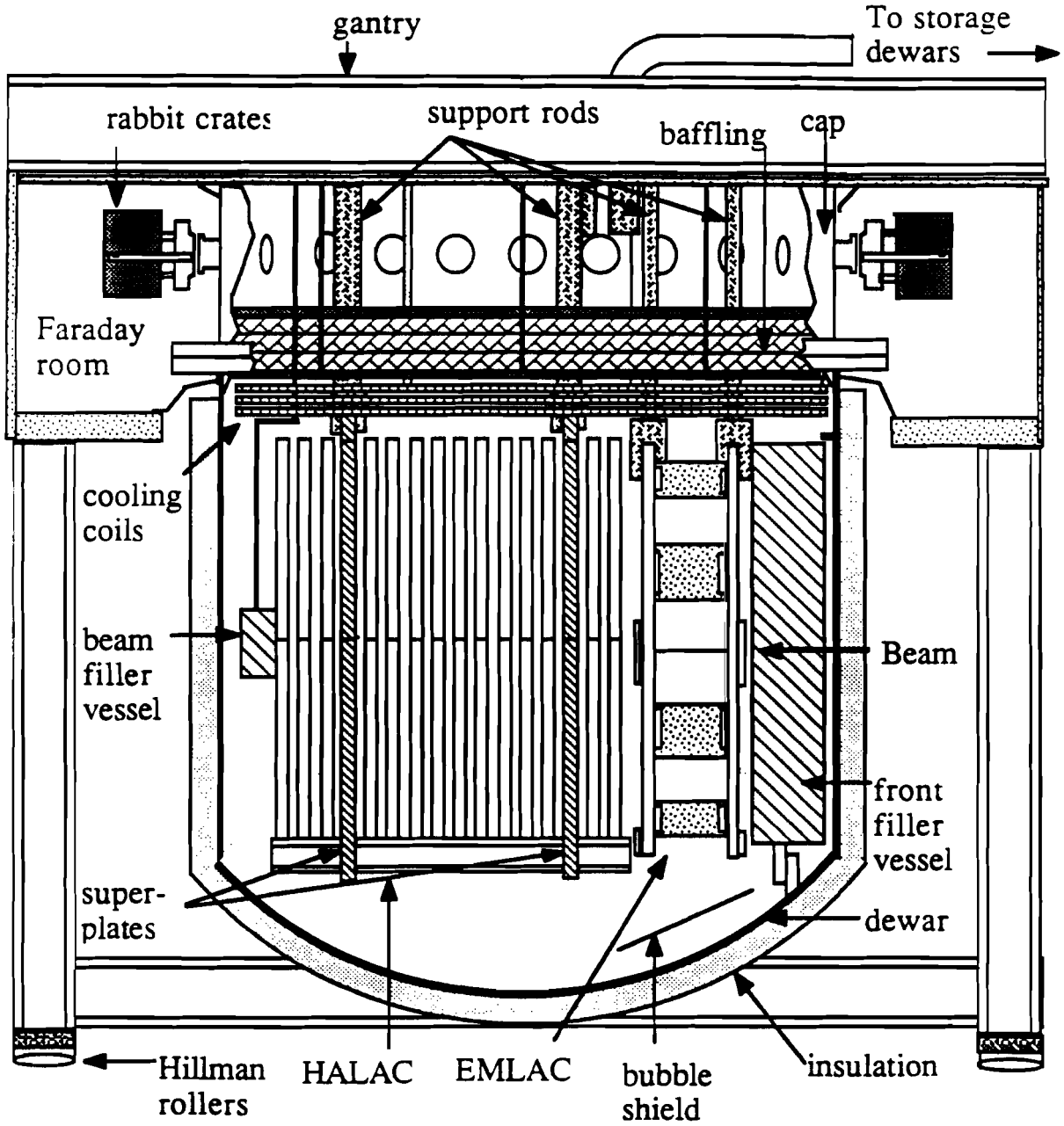

Figure 2.5: LAC cryostat. The beam is incident from the right. Suspended within the cryostat are the electromagnetic and hadron calorimeters. The cryostat is supported by the gantry.

thick steel walls and is filled with low density foam (Rohacell). This excluder vessel is fastened in front of the electromagnetic calorimeter to displace the liquid argon in front of the sensitive region of the calorimeters. The second vessel is a tapered cylindrical beam pipe that passes through the centers of both calorimeters, filling the angular region covered by the forward calorimeter. The beam pipe is 1.6 mm thick and about 40 cm in diameter and filled with helium gas to prevent the pipe from collapsing under the pressure created by the liquid argon. The front end cap of this vessel is 1.6 mm thick and the rear end cap is 3.2 mm thick.

The signals from the calorimeters are transmitted to the outside through vacuum sealed portholes distributed around the circumference of the "top hat". Crates containing charge integrating amplifiers and Analog to Digital Converters (ADCs) are attached to the portholes. Because the amplifiers are sensitive to external electronic noise, the "top hat" was enclosed by a Faraday room built into the gantry. An additional porthole was used as a feedthrough for the high voltage wires connected to the absorber plates (see below).

LAC Design Considerations

For the measurement of direct photon production, the following considerations have to be taken into account in the design of calorimeters:

- Since the cross section for direct photon production is small, a high incident flux ($\geq 10^6$/second) is necessary in order to obtain a useful measurement and, therefore, the calorimeters must be capable of running at the high beam intensities required. Furthermore, since the cross section is small the calorimeter must be able to trigger efficiently, selecting the small fraction of interesting direct photon candidates and eliminating those events with little or no elec-

tromagnetic energy.

- The detectors should be able to distinguish between photons and neutral hadrons.

- As mentioned in chapter 1, the decays of π^0 and η mesons into two photons present a primary source of background to the direct photon measurement. To determine the contribution of this background to the observed yield of single photons, it is important to have excellent efficiency for the detection and reconstruction of the background events. In order to properly reconstruct π^0's and η's, it is essential for the detector to have a large acceptance (solid-angle coverage), good energy resolution and linearity (must be able to detect high energy photons as well as soft photons resulting from asymmetric decays of mesons), and a fine lateral segmentation so as to be able to distinguish single showers from overlapping showers (for high energies, the segmentation must be comparable to a fraction of the transverse dimensions of an electromagnetic shower). In the case of the π^0, the separation ΔR between the photons is given as[13]

$$\Delta R = \frac{2M_{\pi^0} \times D}{E_{\pi^0} \times \sqrt{1 - A^2}} \tag{1.11}$$

where A is the asymmetry in the energy of the two photons from the π^0 decay, D is the distance from the target to the front of the LAC (9 m), and M_{π^0} and E_{π^0} are the π^0 mass and energy respectively. For a 250 GeV π^0 and $A = 0$ the separation is $\Delta R \cong 1$ cm.

- Large acceptance and fine lateral segmentation call for a very large number of readout channels which makes frequent calibration impractical. Therefore, good gain stability over time is required.

Electromagnetic Calorimeter

The electromagnetic calorimeter (EMLAC) is located in front of the hadron calorimeter inside the cryostat. The EMLAC, circular in shape, has an inner radius of 21 cm and an outer radius of 160 cm, corresponding to an approximate angular coverage of 22 mrad $\leq \theta \leq$ 176 mrad in the laboratory coordinate system.

The calorimeter is subdivided into four mechanically independent quadrants, held together by an overall support structure, and has a total of 6,264 channels. Each quadrant consists of 66 layers in which 2 mm thick absorber plates are separated from copper-clad G10* octant-sized anode boards by 2.5 mm gaps of liquid argon. For the purpose of separation of electromagnetic particles from hadrons, the absorber material used in a calorimeter must have a small radiation length (X_0), so that electromagnetic particles deposit their energy in a very short distance, and a large interaction length (λ_I) so that hadrons do not shower quickly. Lead was chosen as the absorber material; it has a radiation length of 0.56 cm and an interaction length of 17.1 cm. The lead plates are kept at ~ -2.5 kV and each one has two 100 nf ballast capacitors (one for each octant) attached to it. The total thickness of the EMLAC is approximately $30X_0$.

The design of the anode boards was based on two main considerations: the need for a fine lateral segmentation required to obtain a good position resolution (limited by the natural width of electromagnetic showers), and the use of the calorimeter to trigger on high transverse momentum (p_T) electromagnetic showers. Based on the triggering requirements, an R/Φ geometry (polar coordinate system) was chosen;

* G10 is a glass epoxy material similar to the one used for printed circuit boards. It does not, however, contain the usual fire retardant additives which are known to contaminate liquid argon.

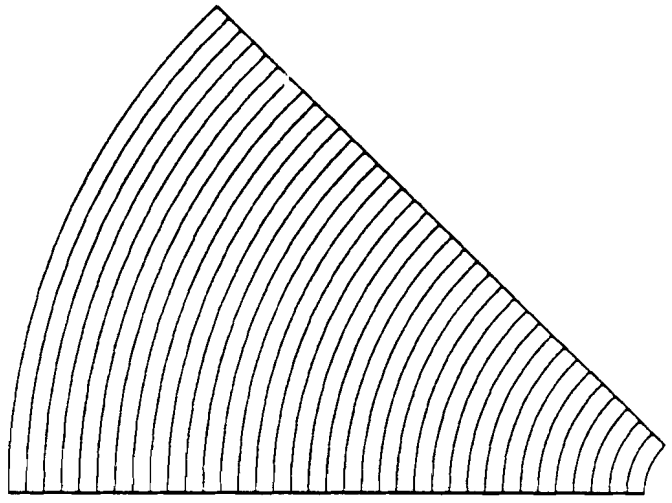

(a)

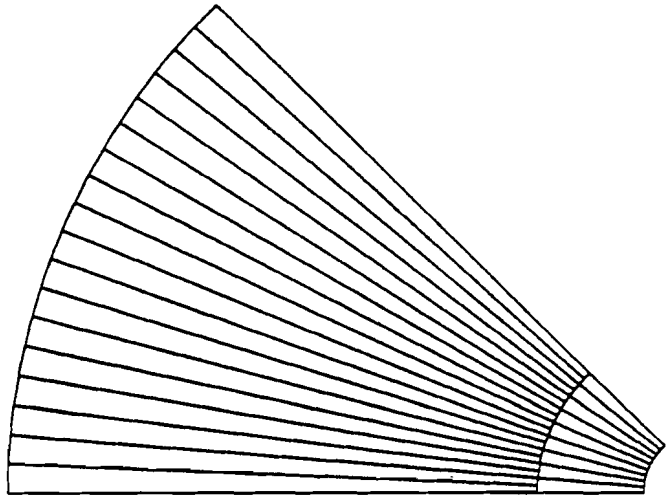

(b)

Figure 2.6: EMLAC anode boards: (a) R-view and (b) Φ-view. The figures show the geometrical design of the boards.

knowledge of the radial position of the deposited energy automatically provides an immediate estimate of the shower p_T without a complicated electronic system. Two types of anode boards were then used, one to measure the radial position (R-view) and one to measure the azimuthal position (Φ-view).

The strips in the R-view boards, fig. 2.6(a), are a series of concentric strips centered on the beamline and focused on the target, so that corresponding strips in different boards subtend the same element of solid angle from the target. Because of the focusing, the width of the R-view strips in a board is determined according to the distance from the target along the beam line. The R-view strips (R-strips) are numbered from 0 to 255. The width of the strips in the first anode board (located 9 m from the target) is 0.55 cm.

The Φ-view boards, fig 2.6(b), are divided into separate inner and outer regions. Each of the strips in the inner region, inner Φ strips, subtends an azimuthal angle of 16.36 mrad whereas the strips in the outer region, outer Φ strips, subtend an angle of 8.18 mrad each. The inner/outer Φ split helps improve the position resolution at large radii by reducing the width of the outer strips which otherwise would become very wide. The exact location of the the inner/outer Φ boundary is also focused on the target. The radius at the boundary is 40.2 cm at a distance of 9 m from the target, which corresponds to an angle of $\sim 73.8°$ in the center of mass frame for an incident beam momentum of 530 GeV/c.

The R-view and Φ-view layers in each quadrant are alternated, the first one being of the radial type. Each quadrant is subdivided into two longitudinal sections. The front section contains the first 22 layers (approximately 10 radiation lengths) and the back section contains the other 44 layers ($\sim$ 20 radiation lengths).

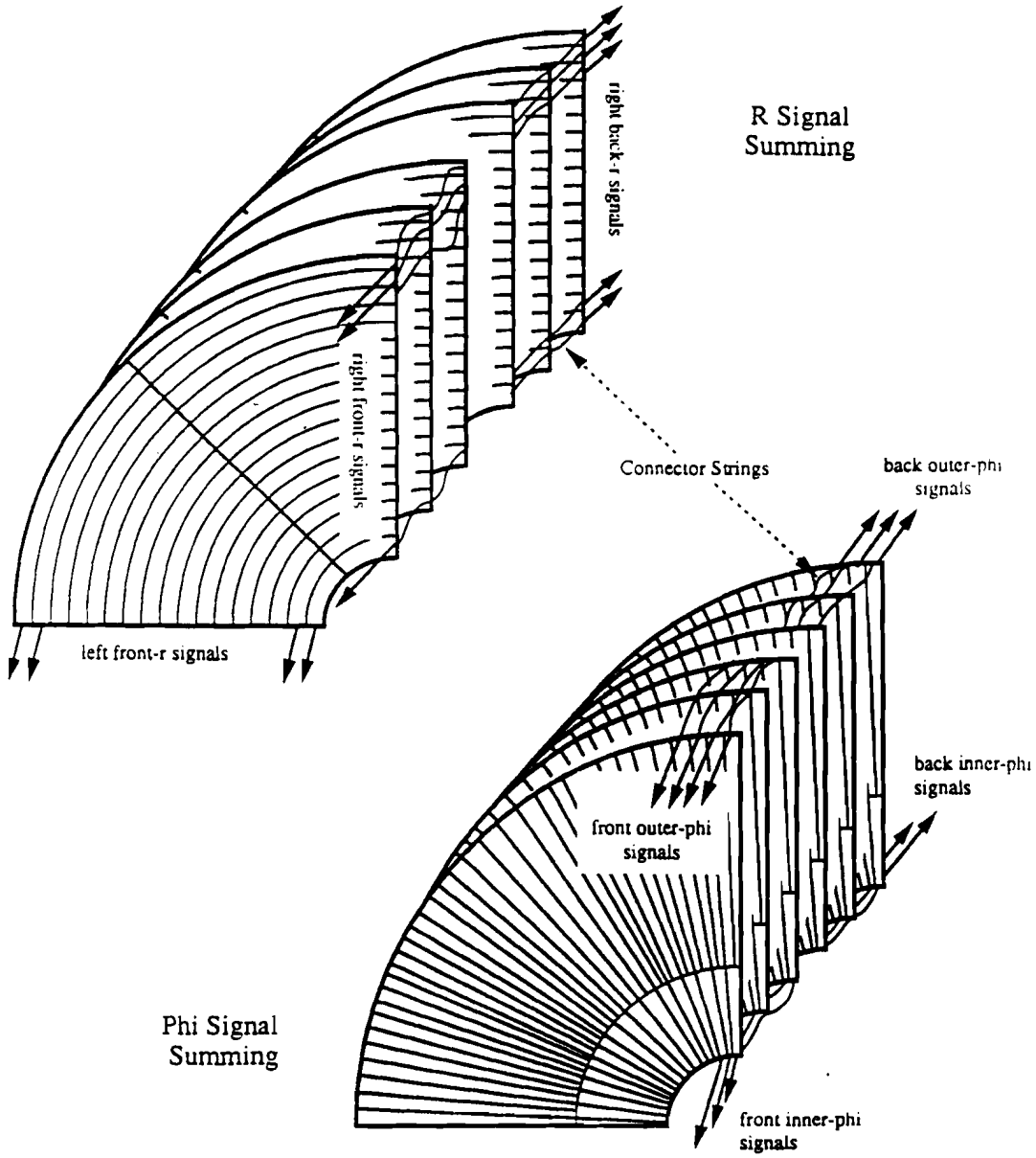

Figure 2.7: Summing of signals for each longitudinal section. The sum is performed by ganging corresponding strips together using connector strings. Signals are summed separately for each view.

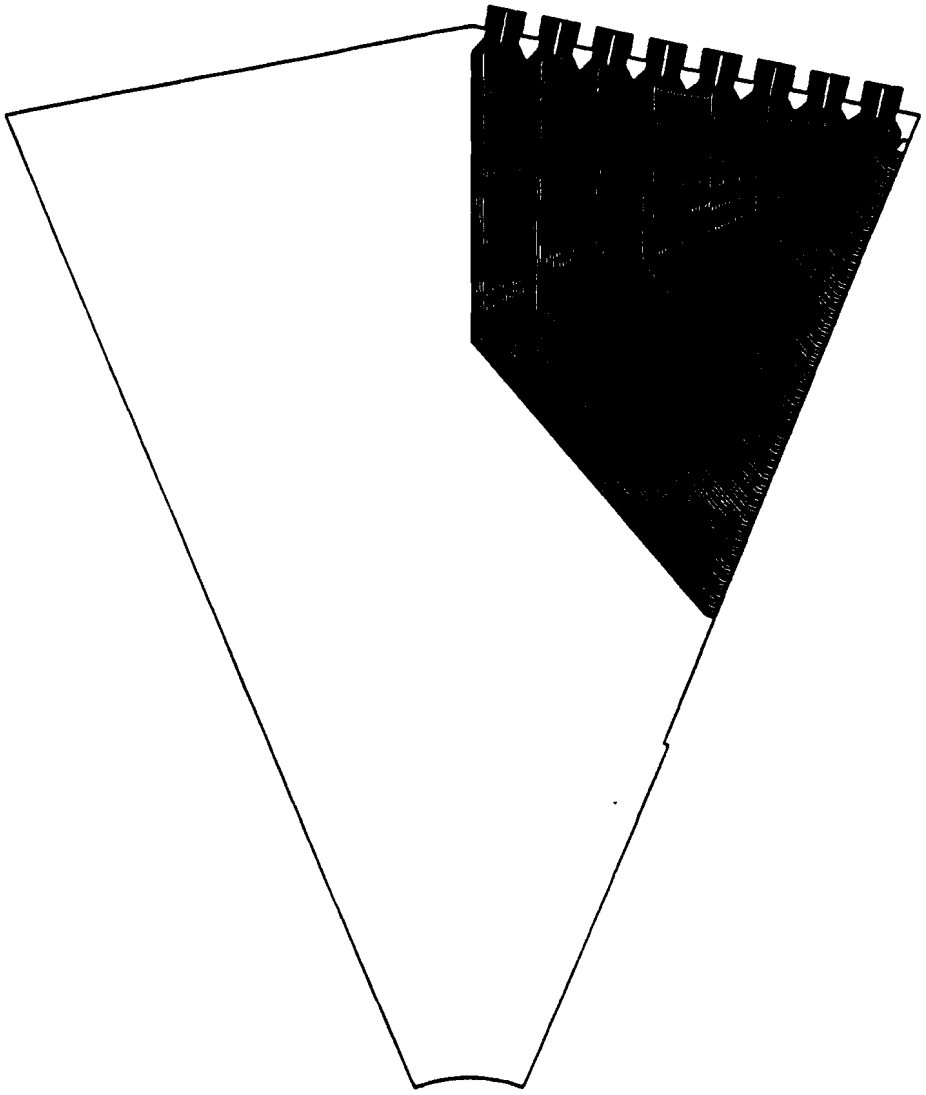

Figure 2.8: Readout board for the outer 128 strips in the R-view of the detector. The connector strings used to gang the strips are connected to the readout board. The signals are then taken to the top of the gantry via cables attached to the connectors in the periphery.

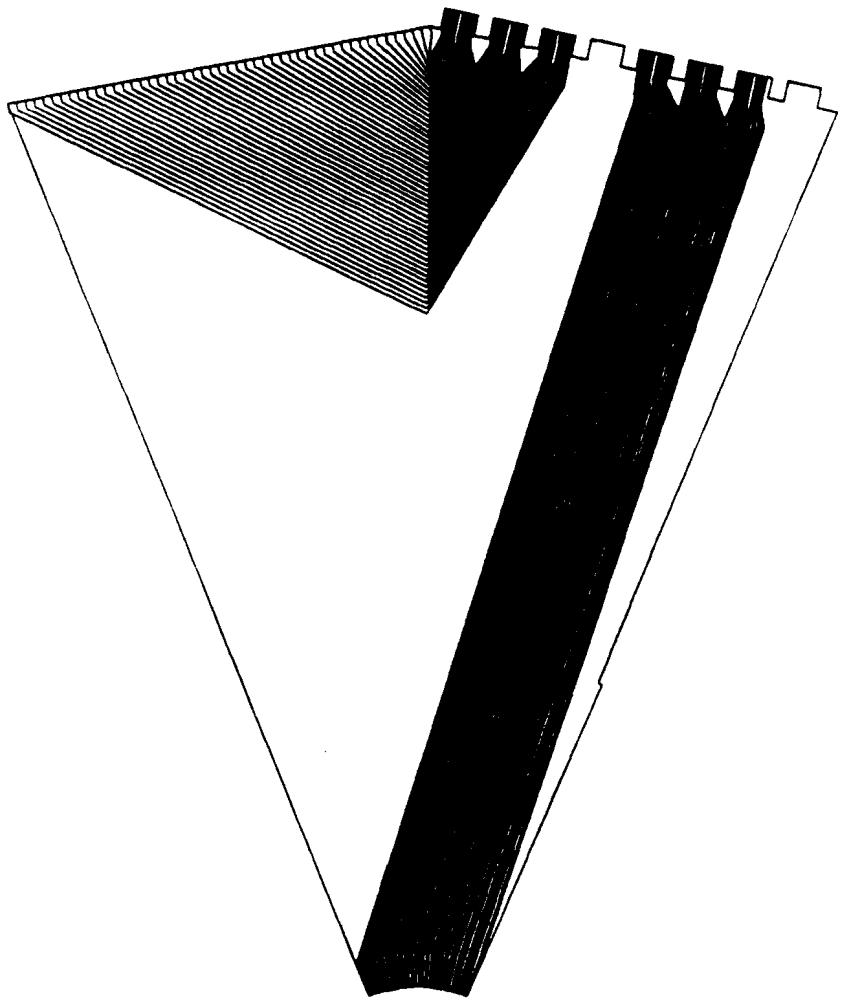

Figure 2.9: Readout board for the strips in the Φ-view of the detector. The connector strings used to gang the strips are connected to the readout board. The signals are then taken to the top of the gantry via cables attached to the connectors in the periphery.

This longitudinal segmentation is useful in the discrimination between electrons and hadrons since electromagnetic particles tend to deposit most of the energy in the front of the calorimeter whereas hadrons tend to start showering in the back. The splitting is also useful in the correlation of energies in the two views and in efficiently resolving the two γ's from the decay of high energy π°'s and η's.

Strips covering the same element of solid angle either in R or in Φ are ganged together in a tower structure to sum the energy along the stack in each of the longitudinal sections, as shown in figure 2.7. The summed signals are then taken to a corresponding readout board. The readout boards are special octant-sized boards which route the summed signals from inside the stack to connectors located on the periphery of the calorimeter. There are three of these readout boards for each octant in each of the sections: one for the innermost 128 R-channels, one for the outer 128 R-channels and the third for the inner Φ channels and half of the outer Φ. The other half of the outer Φ channels are connected to a small readout card attached to the support structure (see figures 2.8 and 2.9). The signals from the readout boards and cards travel through cables to the portholes in the "top hat". Feedthrough connectors epoxied in the portholes enable the signals to reach the amplifier cards mounted on the exterior of the "top hat", in the Faraday room.

Each quadrant is supported by two full-sized G-10 plates located in the front and back of the calorimeter, connected to each other by rectangular steel plates bolted to the edges (radial and outer) of the G-10 plates. The steel plates in the radial sides are tapered and are also used to join neighboring quadrants together. Two steel rings, attached to the steel plates on the outer edge of the quadrants, support the full EMLAC. These rings are attached to the support rods which suspend the

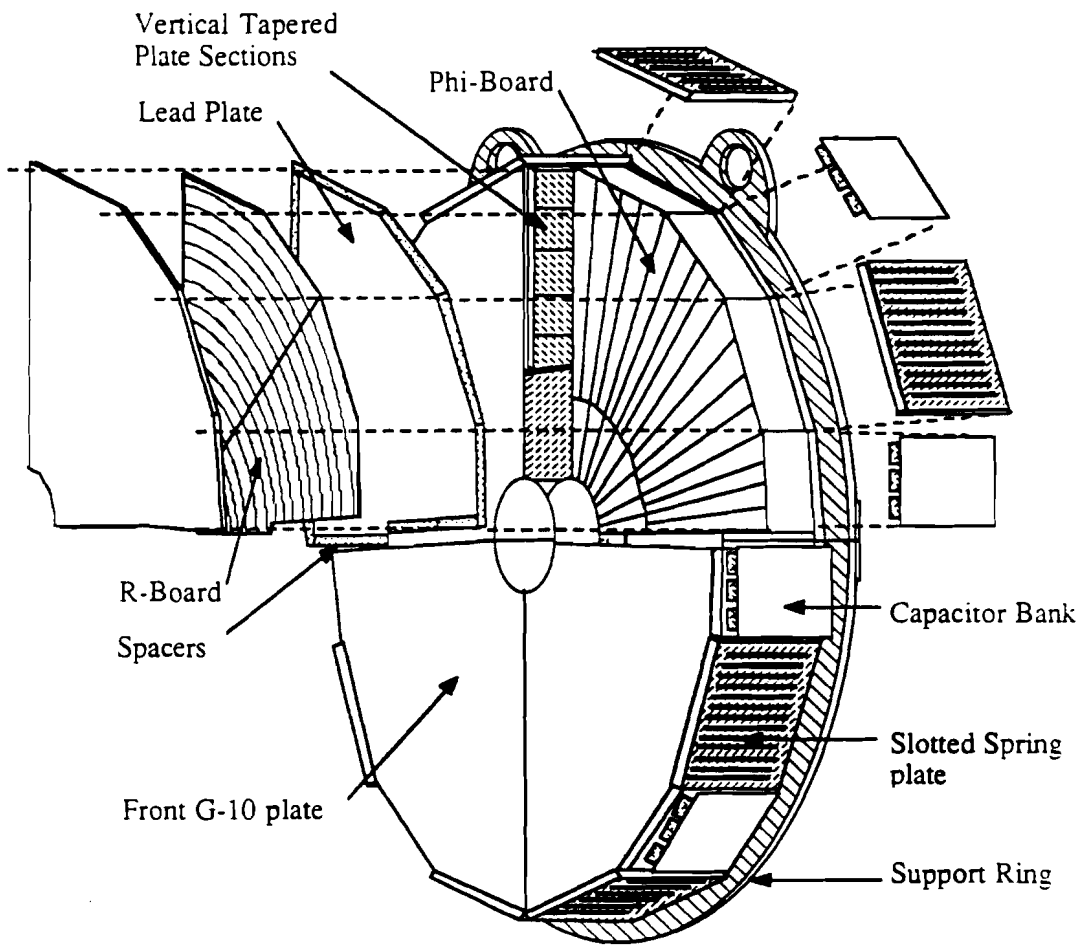

Figure 2.10: Structure of the EMLAC. The figure shows the final configuration of the calorimeter.

calorimeter from the gantry. The ballast capacitors are mounted on capacitor banks which are attached to the support rings on the periphery of the calorimeter, one bank for each octant. Figure 2.10 shows an exploded view of the full EMLAC.

Hadron Calorimeter

The hadron calorimeter (HALAC) has a depth of eight interaction lengths and was designed to fully contain energetic hadronic showers. The HALAC has the same acceptance as the EMLAC. A detailed description of the HALAC can be found in the Ph.D. dissertation by C. Lirakis of Northeastern University.[14]

The HALAC consists of 52 2.5 cm-thick stainless steel absorber plates interleaved with 53 readout modules known as "cookies". The calorimeter is divided into separate front and back sections, the former consisting of the first 14 cookies and 13 absorber plates (approximately 2 interaction lengths). The absorber plates are octagonal in shape. Two of them, called the "superplates", were constructed using a better grade of cryogenic stainless steel; they were designed to support the weight of the full HALAC and are fastened by clevises to four support rods attached to the top of the gantry.

Unlike electromagnetic showers, hadronic showers have a greater lateral spread and therefore a very fine lateral segmentation is not as necessary as in the EMLAC. As for the EMLAC, studies were carried out to decide the detailed characteristics of the calorimeter. One of the decisions taken based on these studies was to have the pad-type readout instead of strips, thus reducing the channel noise contribution. The readout pads are triangular in shape (equilateral triangles). The size of the triangles is such that approximately 93% of the hadronic shower energy will be contained in a hexagon formed from six triangles.

The triangular pads and the readout lines were routed in 0.8 mm-thick copper-clad G-10 readout boards. Because of the need to have electrical connections from each pad to the periphery of the detector, it was necessary to have a pair of comple-

mentary readout boards per module to cover the full detector. Each readout board covers one half of the detector with rows of triangles, leaving the space between rows for readout lines. Since only 122 cm × 366 cm G-10 boards are commercially available, each readout board consists of 3 G-10 boards held together by vertical ribs.

A cookie consists of two complementary halves which combine to give a full and uniform coverage of the cross section of the calorimeter. Each cookie has in sequence, a high voltage (HV) plane, a layer of 3 mm thick G-10 horizontal strips that defines the argon gap and shadows the area covered by the readout lines preventing charge collection in that area, one of the readout boards covering one half of the detector, a layer of 0.8 mm thick G-10 ribs, the second readout board covering the other half of the calorimeter (it has triangles where the other one has readout lines and vice versa), a layer of horizontal strips, and a second HV board. Each HV plane consists of a 0.8 mm thick layer of copper double-clad G-10 boards; the side facing the pads was kept at −3kV while the other side was kept at ground. Thus, the HV boards acted as their own ballast capacitor. Figure 2.11 shows an exploded view of the cookie structure. The full pad configuration of the cookie is shown in figure 2.12.

The pad signals are sent to the edges of the cookie. In each longitudinal section of the HALAC, the pads of successive cookies that cover the same element of solid angle are ganged together to form towers, for a total of 2,340 channels. The towers also focused on the target and, therefore, the size of the triangles in each cookie depends on its distance to the target, starting with a height of 4.4 inches in the first cookie to a height of 5.5 inches in the last cookie. Towers of pads in the same row are daisy chained together in groups and the chain is terminated in a patch board

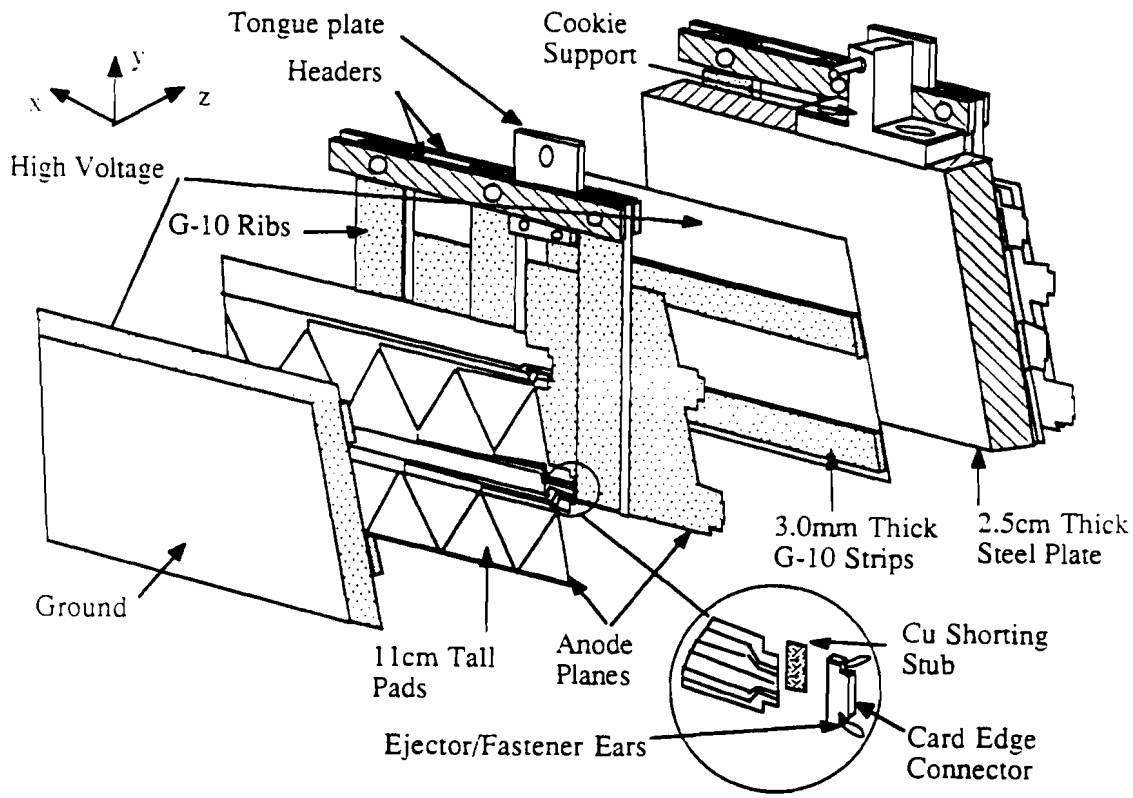

Figure 2.11: Exploded view of a HALAC cookie.

where the output is reconfigured. The signals from the patch boards are then sent to the portholes in the "top hat" and fed into the amplifier cards.

LAC Cryogenics

Two sets of copper cooling coils, through which liquid nitrogen flowed, were supported by the cover plate in the gantry and mounted just above the calorimeters. One of the sets was used in the cooldown process to cool the argon gas, and the other set was used to regulate the pressure and temperature after the cooldown was complete. Since carbon steel becomes brittle at low temperatures and is very likely

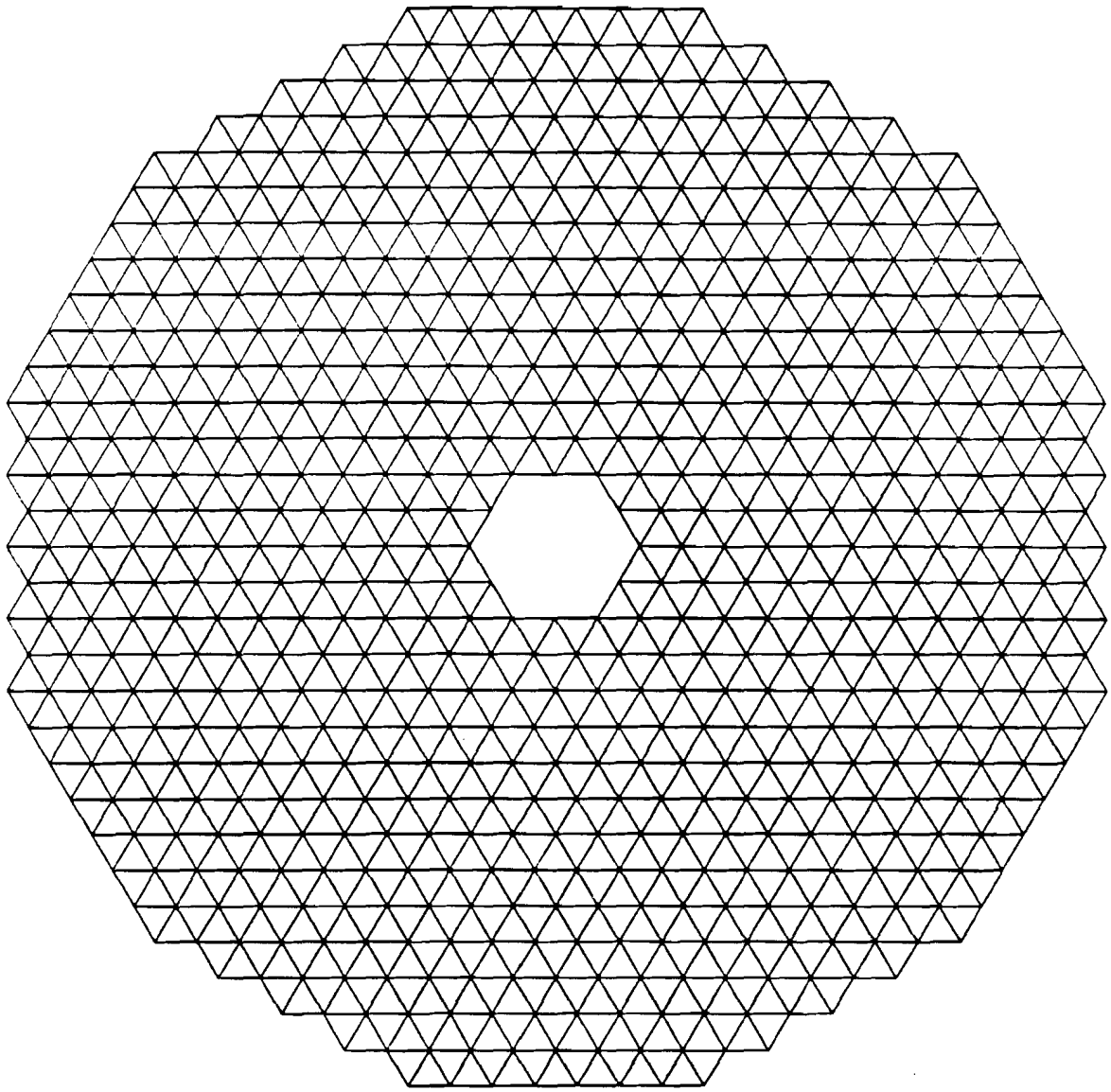

Figure 2.12: Triangular readout pattern of a cookie.

to fracture under load, plastic baffling was placed above the cooling coils to prevent the "top hat" from being cooled by thermal convection.

The process of filling the cryostat with liquid argon was accomplished in several steps. After the LAC system was assembled and the cryostat sealed, the system was pumped down until the pressure inside the cryostat was approximately 100 microns. This "pumping down" process lasted for about two months, until the contents of the cryostat were degassed and small leaks, mainly in the portholes in the "top hat", were found and sealed. Once the pump down process was complete, the system was cooled down by circulating liquid nitrogen through the copper coils to cool argon gas which was being introduced into the cryostat. After the system was cooled down to 96°K, 17,200 gallons of liquid argon were transferred into the cryostat. Approximately 170 thermocouples were attached to the calorimeters, the support rods, cryostat walls and argon excluder vessels, to monitor temperature changes and variations. It was very important to monitor the system during cooling since the calorimeters were expected to be very sensitive to large temperature gradients. During the cooldown and filling operations, which lasted several weeks, the maximum temperature gradient between any two points of the calorimeters never exceeded 30°C.

The amount of charge deposited in the calorimeter is proportional to the energy of the incident particle. In the EMLAC case, the detected charge Q, was determined to follow the relation[15,16]

$$Q = Q_0 \frac{2S}{D}\left[1 - \frac{S}{D}\left(1 - e^{-D/S}\right)\right] \tag{2.1}$$

where Q_0 is the total electronic free charge deposited, D is the argon gap size, $S = \alpha E/p$, with $\alpha = 0.12$ (for S measured in cm), E is the applied electric field, and

p is the impurity concentration in parts per million (ppm). Q_o is given by

$$Q_o = e\frac{dE}{dx}\frac{D}{W} \tag{1.11}$$

where W is the typical energy required to ionize an atom in liquid argon and dE/dx is the energy loss per unit length to ionization.

By plotting the collected charge as a function of the electric field applied and fitting equation (2.1) to the data, the contamination found in a sample of liquid argon can be measured in equivalent parts per million (ppm) of oxygen. This method was used during the filling process to determine whether to accept the argon delivered by the vendor, and to monitor the purity of the liquid argon over time. The liquid argon delivered had an average contamination measured to be $\sim$ 0.43 ppm of oxygen equivalent contamination.

LAC Readout Electronics

The readout system for the LAC was based on the Redundant Analog Bus Based Information Transfer system (RABBIT) developed at Fermilab. The RABBIT system consists of crate controllers (EWEs), Before After Timers (BATs), and Front End Electronic Devices (FEED). The amplifier cards (LACAMPS) developed for E706 are of the FEED type. There are 28 RABBIT crates used in the LAC readout system, each with 2 EWEs (allowing use of both the top and bottom buses for faster readout), one BAT, and 22 slots allocated for LACAMP cards. The crates are mounted around the top of the LAC cryostat inside the Faraday room. A detailed description of the LAC readout system can be found in the Ph.D. dissertation by D. Skow of the University of Rochester.[17]

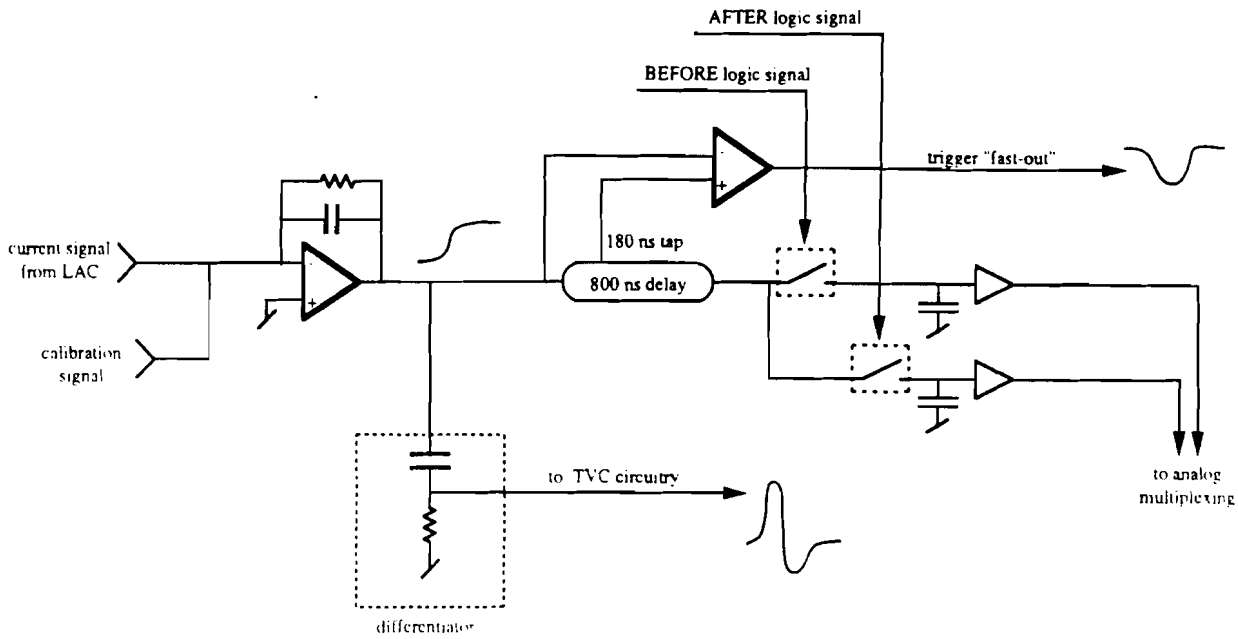

Figure 2.13: LAC Amplifier Module Diagram

Each amplifier card contains 16 charge integrating amplifiers. Amplifier gains and pedestals were measured by injecting charge across a precision (1%) capacitor connected to the outputs of the 16 channels. The results from this calibration procedure, performed at different times, were stored in a data base accessible to the off-line reconstruction software. The output from each charge integrating amplifier traveled to three separate circuits: the fast output, the Time to Voltage Converter (TVC), and the sample and hold (fig 2.13). One of the output signals from the amplifier was sent through an 800 ns delay line. The delay allowed a trigger decision to be performed on the event before the amplifier output was sampled. A fast output signal was derived by subtracting the output from the amplifier from a delayed copy of itself (taken on the 180 ns tap of the delay line). The fast output signal was sent to the trigger electronics to be used in the selection of the event. If the event satisfied the condition for a pretrigger (see chapter 3), an EVENT signal was sent to the

BAT to instruct it to generate a BEFORE signal and some time later (typically 500 ns), an AFTER signal in the RABBIT crate back plane; the delay between the BEFORE and AFTER signals was programmable using an 8-bit digital to analog converter (DAC) in the BAT.

In the sample and hold section of the LACAMP a switch was opened upon receipt of the BEFORE pulse and a second switch was opened on receipt of the AFTER signal; the output level was held in a separate 1 nF capacitor each time. A TVC received the sum of the amplifier outputs of four adjacent channels. This signal was then differentiated and compared to a crate-wide threshold, with the resulting logical signal used to start a timing circuit. The timing circuit was stopped if and when the BEFORE signal arrived. When the circuit was triggered , a second circuit was enabled to allow for the possibility of a second hit. The timing circuits produced a voltage level proportional to the time between their being triggered and the arrival of the BEFORE signal.

Each EWE was controlled by a hard wired ECL processor called an MX, a dedicated computer developed at Fermilab for use with the RABBIT system. When an event was selected by the trigger, each EWE was instructed to address each amplifier and collect the signal from the sample-and-hold and the TVC circuits. In the EWE, the difference ΔV of the output levels in the sample-and-hold circuit in each channel, ($\Delta V = V_{after} - V_{before}$), had the pedestal value for that channel subtracted from it. If the voltage level (with pedestal subtracted) was above a predetermined threshold, called the zero suppression threshold, the signal from the channel was digitized by a 16 bit analog-to-digital converter (ADC) and the result stored by the MX.

Though each MX can control a maximum of eight EWEs (four crates), for greater speed the system was set up using three crates per MX. When the trigger selected the event, the MXs were instructed to start gathering event information in one of their four buffers. The MXs, in turn, instructed the EWEs to start addressing the amplifiers and the information from all channels with signals above threshold were then stored by the MXs.

2.5 The Forward Calorimeter

The forward calorimeter (FCAL) was designed to intercept the forward angular region which is not covered by the LAC. The FCAL was located $\sim 17\,\mathrm{m}$ downstream of the target and consisted of three modules supported on a rail system which permitted movement transverse to the beam, sufficient to (1) allow access to the end cover-plates covering photomultiplier tubes and associated electronics, (2) allow individual modules to be placed in the beam axis for calibration, and (3) align the calorimeter relative to the beam. A complete description of the FCAL is given in the Ph.D. dissertation by R. Benson of the University of Minnesota.[18]

Two of the modules contained 28 steel plates, 1.905 cm thick, with a diameter of 114.3 cm. The third module contained 32 plates. The steel plates were separated by 0.64 cm gaps in which 0.46 cm thick sheets of acrylic scintillator (Plexipop) were placed. The plastic and scintillator sheets had a central 3.18 cm diameter hole to allow passage of the non-interacting beam. The scintillator and steel sheets had a grid of 76 holes through which wavelength-shifter rods were inserted. Figure 2.14 shows a view of the forward calorimeter.

The wavelength-shifter rods were BBQ doped and contained an ultraviolet absorbing agent which absorbed the ultraviolet light, up to wavelengths of 375 nm,

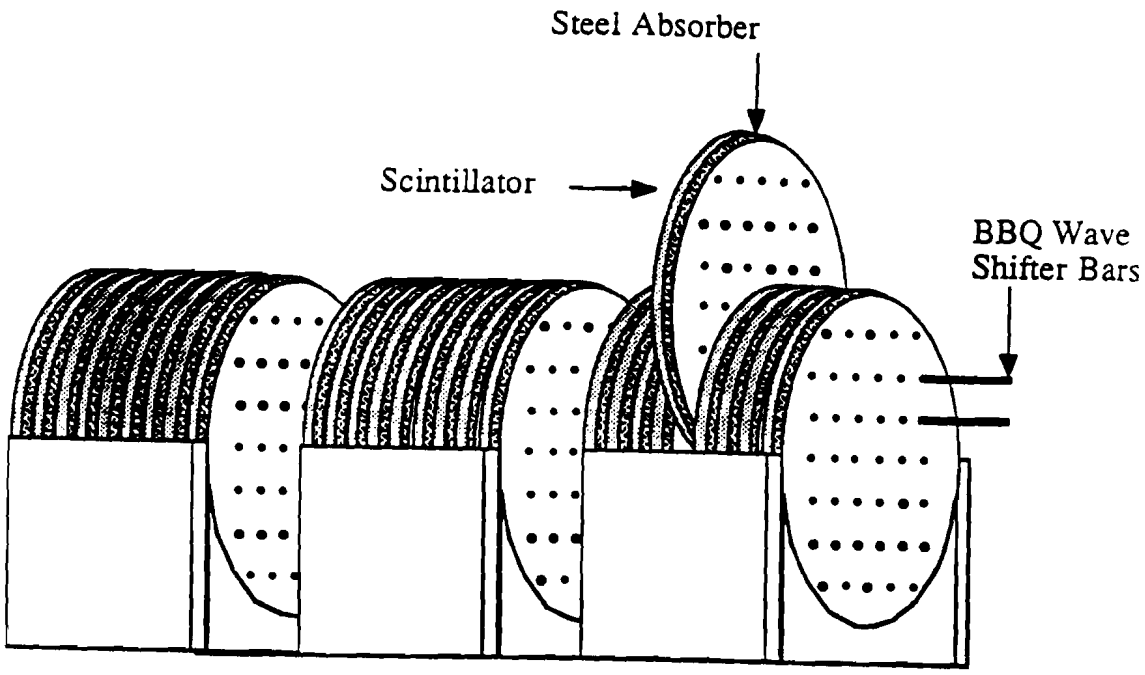

Figure 2.14: The Forward Calorimeter

to minimize effects of Cherenkov light produced by particles passing through the rods. Each rod was silvered at one end and attached to a single photomultiplier tube (PMT) at the other end. The bases for the PMTs were designed to perform at rates of up to 10 MHz. Anode signals were amplified by a factor of 20 at the base using a fast RF amplifier before being sent via coaxial cables to the remote flash-ADC system to be digitized; the rise and fall times of the signals were 5 and 15 ns respectively.

2.6 Data Acquisition System

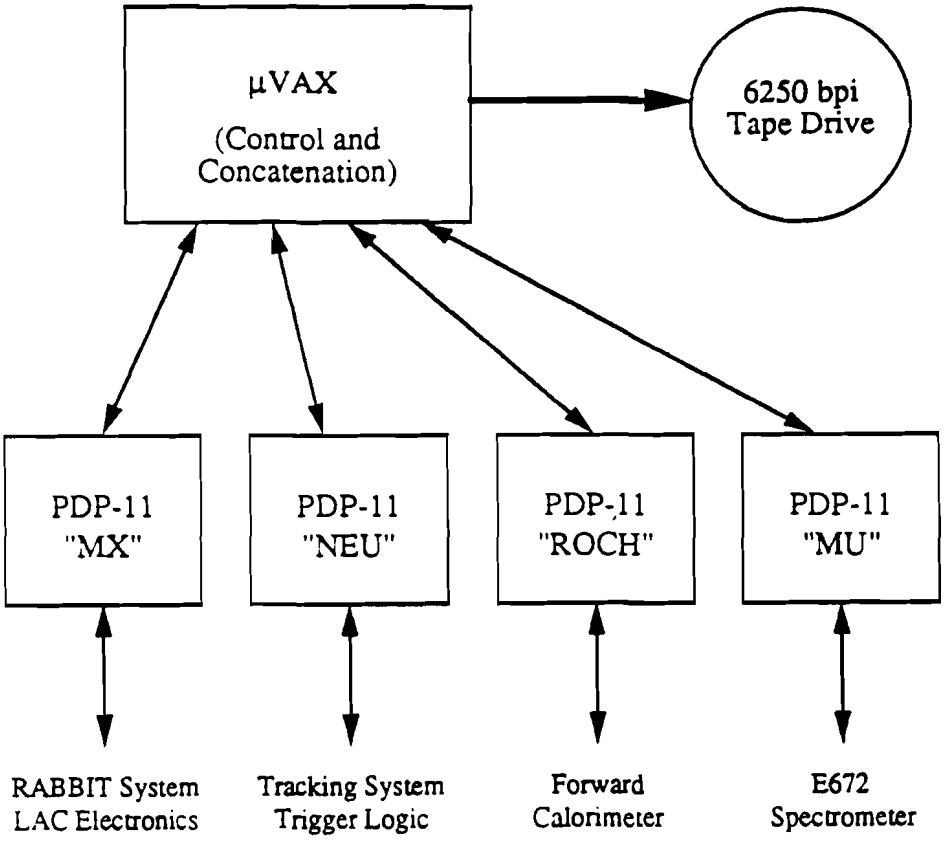

Figure 2.15: Data acquisition system diagram

For data acquisition purposes the experiment was subdivided into four separate sections. Each section was assigned to a Digital Equipment Corporation (DEC) PDP-11 minicomputer. The PDPs controlled the readout of the event information from the various detectors in the spectrometer. The four sections were designated as follows: (1) the SSD/PWC tracking system, trigger logic and Cherenkov detector,

(2) the the LAC system, (3) the forward calorimeter, and (4) the E672 Dimuon system. (1), (3) and (4) were controlled by PDP-11/34's. These three sections were instrumented with CAMAC devices and were readout using standard parallel and serial links. The LAC data acquisition used the RABBIT system described above. The tasks in all the MXs were controlled by a PDP-11/45. The data readout by the four PDPs was concatenated by a DEC Microvax II computer (μVax). This computer was the central on-line data acquisition system driver. It was used to control the process of data taking and the monitoring tasks. After the information from the PDPs was concatenated, it was sent to a space in memory known as the event pool, and then it was written on a magnetic tape. Figure 2.15 shows a block diagram of the data acquisition system.

The software used for on-line data data acquisition was VAXONLINE[19], a software package developed by the Fermilab computing department. Some of the data stored in the event pool was sent to a DEC VAX 11/780 computer and used for on-line monitoring of the detectors. Two tape drives were assigned for the logging of data onto magnetic tape, thus minimizing the dead time due to tape rewinding. The process of data taking was segmented into "runs". The term "run" referred to a period of collection of data during which the conditions of the experiment remained constant. In normal conditions, a run was defined by the filling of one 6250 bpi magnetic tape with data.

3. TRIGGER DESCRIPTION

This chapter describes the trigger implemented for experiment E706 during the 1987-1988 data run. The first section gives a brief description of the trigger. In the following sections a more detailed description is given including the setup, functions and logic implemented. The performance of the trigger is presented in chapter 5.

3.1 Overview

The trigger system used in experiment E706 was designed to perform at rates of up to 10^6 interactions per second, triggering on high transverse momentum (p_T) electromagnetic showers as dictated by the goals of the experiment. It was built using a combination of NIM units, CAMAC programmable logic units (PLUs)*, and custom-designed summing and weighing p_T cards. Most of the trigger system was computer controlled; this feature, in combination with the versatility of the PLUs, gave the capability to implement and handle different trigger combinations with minimal changes in the hardware structure. For testing purposes, pulser triggers were set up and enabled for basically any specific section of the trigger and the data acquisition system. In addition to triggering on events of interest for E706, the trigger system was implemented to coordinate the final event selection in a

* The NIM and CAMAC units mentioned here are described in the LeCroy catalog.

sharing mode with experiment E672. E672 studied the production of dimuon pairs in hadronic collisions using the same beam and target used by E706.

Basically, the decision of triggering on a particular event was done in three main steps: beam and interaction definition, preselection of the interaction, and the final selection of the event.

For the definition of an incident beam particle, two plastic scintillation counters, BA and BB, were located in the beam line directly upstream of the target (figure 3.1). A beam particle signal was defined as the coincidence of the signals of the two beam counters. To define an interaction, the logical OR of the discriminated signals from four scintillation counters, SE1, SW1, SE2 and SW2, was put in coincidence with the beam signal. When an interaction occurred, it was additionally required that no other interaction occurred within ± 60 ns of the present interaction in order to prevent overlapping of signals due to insufficient time resolution (pile-up). If this additional requirement was satisfied, it was further required that the incident particle was not a beam halo particle. For this purpose, the signal from BH, a plastic scintillation counter located next to BA and BB and which had a hole in its center, was used in anticoincidence with the interaction which satisfied the pile-up filter. If all conditions were met, an interaction strobe signal was produced.

After the interaction was accepted and the interaction strobe signal was generated, the final trigger decision was reached based on the deposition of energy in the EMLAC. For triggering purposes each octant was treated independently. The energy deposited in each octant was weighed according to its radial position, and individual octant signals were created. The weight applied to the energy was so

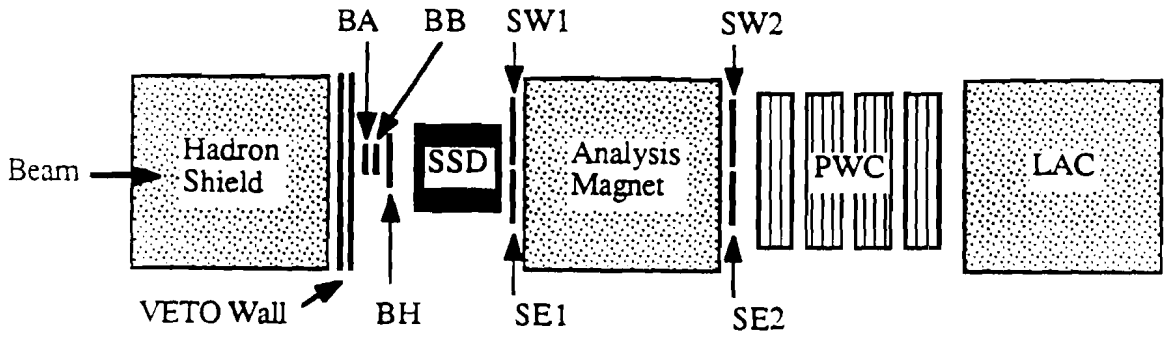

Figure 3.1: Layout of the Trigger System Counters. The size of the counters has been exagerated with respect of the surrounding spectrometer components.

that the transverse momentum deposited could be represented by

$$P_T = E \sin \theta \tag{3.1}$$

where E was the amount of energy deposited, and θ the angle between the beam line and a line from the target to the point of energy deposition.

Since most hadronic interactions produce particles with low p_T, a preliminary step in the event selection was executed in order to minimize the dead time caused by the processing of low transverse momentum events. To find if the event was to be preselected, signals from each octant were processed to determine if the following requirements were satisfied:

- the total transverse momentum deposition within the innermost 96 R-strips

Having preselected the event, the next step was to determine if conditions were satisfied to select the event. As mentioned above, each octant was treated individually. Two signals from each octant were used in this part of the event selection: a global p_T signal and a local $p_T$signal. The octant global p_T was the total amount of transverse momentum deposited in the octant. This global p_T signal was susceptible to coherent noise (noise common to all channels) and also to multiphoton events in which each photon carried low p_T. The fine granularity of the EMLAC was used to suppress events of this kind by requiring a local p_T condition: a substantial fraction of the octant global p_T had to be deposited within 16 radial strips of the calorimeter, roughly the size of a single electromagnetic shower. Each of the two octant p_T signals (local and global) was discriminated using two different nominal thresholds. Using combinations of the two p_T signals and the different thresholds, four LAC triggers were implemented:

- LGHI: this trigger required that, in at least one octant, the momentum deposition was such that the local p_T signal satisfied the low local p_T threshold and the global p_T signal satisfied the high global p_T threshold.

- LGLO: this trigger was similar to the LGHI trigger, except that the global p_T signal was only required to satisfy the low global p_T threshold. The purpose of having two similar triggers differing only in the threshold requirement, was to measure the efficiency of the trigger required to satisfy the higher threshold. The lower threshold was set so that by the time the LGHI trigger started to "turn on", the LGLO trigger was 100% efficient and the efficiency could be determined by measuring what fraction of the time the LGHI trigger fired when the LGLO trigger was satisfied. Since most of the events are at low p_T,

the LGLO trigger was prescaled by a factor of ten to avoid its dominance in the event selection.

- SLOC: the requirement for this trigger was that one or more octants had a local p_T signal which satisfied the high local p_T threshold.
- TWOG: unlike the other three LAC triggers, for this trigger a combination of two octants was necessary. The TWOG trigger required that the local p_T signal in one octant satisfied the low threshold and the local p_T signal in any of the three geometrically opposite octants also satisfied the low threshold.

In addition to the conditions mentioned above, each of the four LAC triggers required the LACPRET signal, as well as the octant pretrigger signal(s) corresponding to the triggering octant(s). If no trigger was satisfied after LACPRET had been generated, a reset signal was sent to the SSD/PWC latches, the FCAL, and the BATs. Five microseconds later, after allowing the electronics to settle, the system was reset and the preselection process was executed for the next event. If any of the triggers had been satisfied, an INTERRUPT signal was sent to the computers to instruct them to read in the data stored in the different elements of the spectrometer. After collecting the data, the computer system generated a reset which was fanned out to the different electronics substations, the BATs, and finally the trigger system was reset to start processing the next event.

The trigger system can be divided into three sections: data acquisition controls, beam and interaction definition, and the high transverse momentum electromagnetic shower selection and final trigger decision.

3.2 Data Acquisition Controls

There were four subsystems in E706, each handled independently by a PDP-11 (see chapter 2). The data acquisition control section, located in the counting room, was set up so that combinations of subsystems could be operated independently. The process of data taking was controlled by gates and pulses generated at different times during the beam spill. The communication between the trigger and the individual PDPs was done via Bison boxes.[20] This control section had the basic task of synchronizing the data taking operation between the different subsystems.

As described in chapter 2, the beam spill was approximately 23 sec long, and spills were $\sim$ 35 sec apart. The start and the end of the spill were marked by begin spill (BEGSP) and end spill (ENDSP) signals generated using reference times provided by the main ring accelerator control.

At the beginning of the spill, a gate labeled DAGATE (data acquisition gate) was "turned on" and a begin data acquisition (BEGDA) pulse was generated by the BEGSP signal. DAGATE defined the time span during which the computers that controlled the selected spectrometer subsystems were to be ready to collect data. Both pulse and gate were sent to each of the Bison boxes. 100 ms later, after allowing the system to become ready to start collecting data, BEGSP enabled a beam gate (BMGATE) and generated a begin beam (BEGBM) pulse. BMGATE set the time interval during which incoming beam particles were to be considered for triggering purposes. BMGATE remained enabled until the ENDSP signal arrived, at which time an ENDBM pulse was generated. The ENDSP signal was delayed by 100 ms to allow the computers to read in any remaining information, and then it was used to turn off DAGATE and produce a corresponding ENDDA pulse. All

these gates and pulses generated during the spill were fanned out and sent to the different stations in the MW9 experimental hall for local use.

During the spill, when both DAGATE and BMGATE were enabled, the trigger was in charge of directing the computers to record the desired events. When a particular event was selected, an INTERRUPT signal was sent to all Bison boxes involved in the data taking process to notify the corresponding computers to read in the event information. At this time each Bison box generated a BUSY gate which remained enabled until the data from the corresponding subsystem had been completely read in. When all the computers were ready, i.e., all the BUSY gates were disabled, a computer ready gate (COMP_RDY) and a computer reset pulse were produced. The computer ready gate indicated that all the computers were available to continue taking data and the reset signal cleared the trigger and enabled it to continue the event selection.

3.3 Beam and Interaction Definition

This section of the trigger, implemented in the upstream latch house in the main MW9 hall, processed the veto wall, beam and interaction counter signals.

To define beam, three scintillation counters were located on the beam line immediately downstream of the veto wall, approximately 1.5 m in front of the target (see figure 3.1). Two of them, BA and BB, were 2.54 cm $\times$ 2.54 cm and completely overlapped with each other. The other counter, BH, was 12.7 cm $\times$ 12.7 cm and had a hole, 0.95 cm in diameter, centered on the beam line. Four additional scintillation counters, SE1, SW1, SE2, SW2, were used to define an interaction. SE1 and SW1 were located $\sim$35 cm downstream of the target immediately before the front mirror

plate of the analyzing magnet; SE2 and SW2 were located immediately after the downstream mirror plate at ~ 367 cm from the target. The interaction counters in each pair were matched side by side to cover the full acceptance region of the spectrometer, leaving a hole around the beam line. These holes were 1.9 cm and 3.8 cm in diameter, upstream and downstream of the analyzing magnet respectively.

The signals from BA, BB, BH, SE1, SW1, SE2, SW2 were sent to NIM L612A photomultiplier amplifiers where they were amplified by a factor of ten and then through CAMAC 4416 discriminator units to produce the corresponding logic outputs. The discriminated outputs were fanned out to be sent to scalers and other components of the trigger logic electronic units.

The dicriminated BA and BB pulses were timed with respect to each other and then sent to a CAMAC L4532 majority logic unit where two output signals corresponding to the logical OR and the logical AND of BA and BB were produced. These two outputs were sent to a 4508 PLU (BEAM) where the definition of beam was done. The BEAM PLU was first cleared by an RF clock pulse and then strobed by the same pulse delayed by 5 ns. The RF clock is a pulser referenced to the main ring control; it runs at ~ 52 Mhz and produces a train of 10 ns wide pulses in phase with the accelerator, simulating the beam structure. BMGATE, defined above, was also input into this logic unit. A beam particle (BM) was then defined by requiring a coincidence between BA, BB, BMGATE and the RF clock pulse.†

$$\mathrm{BM} = \mathrm{BA} * \mathrm{BB} * \mathrm{BMGATE} * \mathrm{RF_CLOCK} \tag{3.2}$$

The RF clock was used in the logic to make sure that the the signals were in phase

† A note in the notation used: analog signals are labeled with small letters and logic signals are labeled with capital letters. The sum of analog signals indicates an actual sum, whereas a sum of logical signals indicates a logical OR.

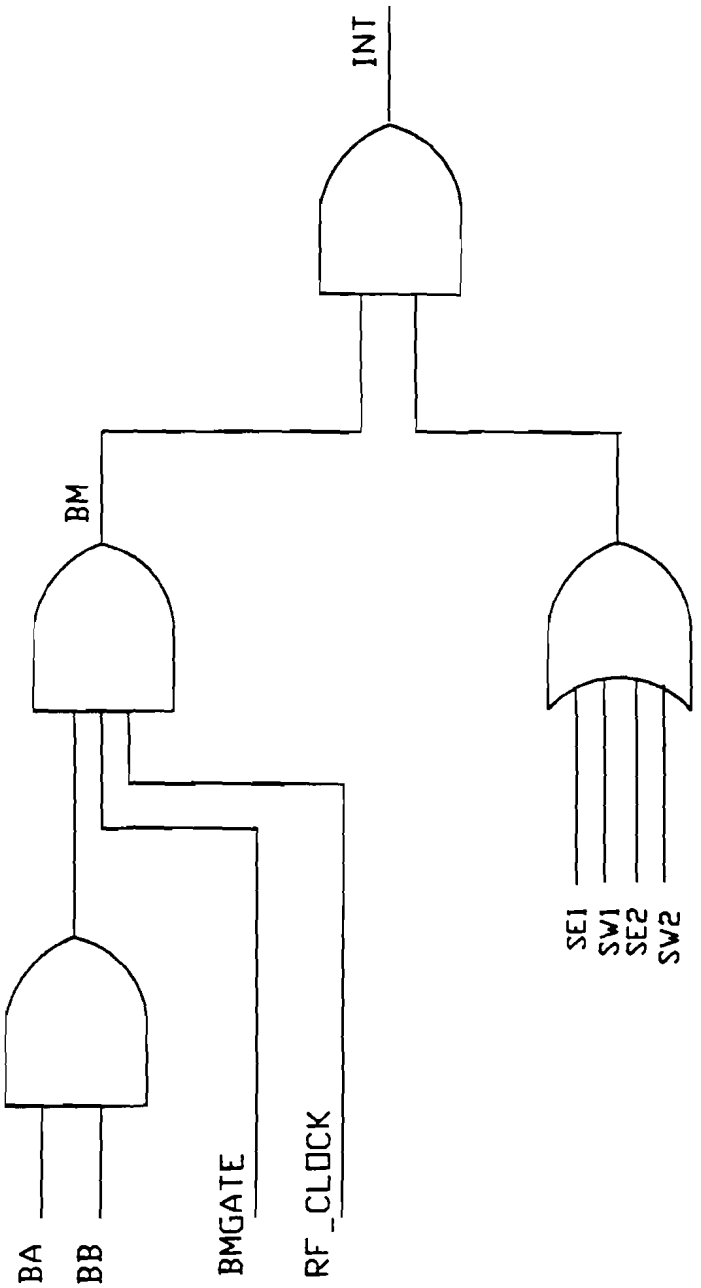

Figure 3.2: Beam and Interaction logic definition diagram.

with the accelerator, and also to process those signals at the necessary high rates.

The discriminated output signals from SE1, SW1, SE2, and SW2 were timed with respect to each other and input into a 4508 PLU strobed by BM. The logic in this unit was set to define an interaction if any of the interaction counter signals was present in coincidence with BM.

$$\mathrm{INT} = \mathrm{BM} * (\mathrm{SE1} + \mathrm{SW1} + \mathrm{SE2} + \mathrm{SW2}) \tag{3.3}$$

Figure 3.2 shows schematic diagrams of the beam and interaction logic definitions.

INT was sent through an early/late circuit used to avoid interaction pile-up. In the early/late logic circuit, a CAMAC 4418 delay unit was used to delay INT sixteen times; each time, the signal was delayed by ~ 20 ns (the time between beam buckets) except for the ninth time when the delay was the equivalent of two beam buckets. A delayed INT output was produced each time, for a total of sixteen output signals. An additional signal, corresponding to INT delayed by 9 buckets, was generated and used as the $t = 0$ reference signal. This set of delayed INT outputs could be used to determine the occurrence of interactions during the eight buckets preceding the current interaction, or during the eight following buckets. The eight pulses from the 4418 unit corresponding to the first eight delays were fed into a 4508 PLU (LATE), and the other eight into another 4508 (EARLY). Both PLUs were cleared and strobed with the INT signal delayed by nine buckets. This implementation of the early/late circuit allowed for a selection of early/late windows as wide as 16 buckets (± 8 buckets) for a cleanliness requirement. We chose to use a 6-bucket

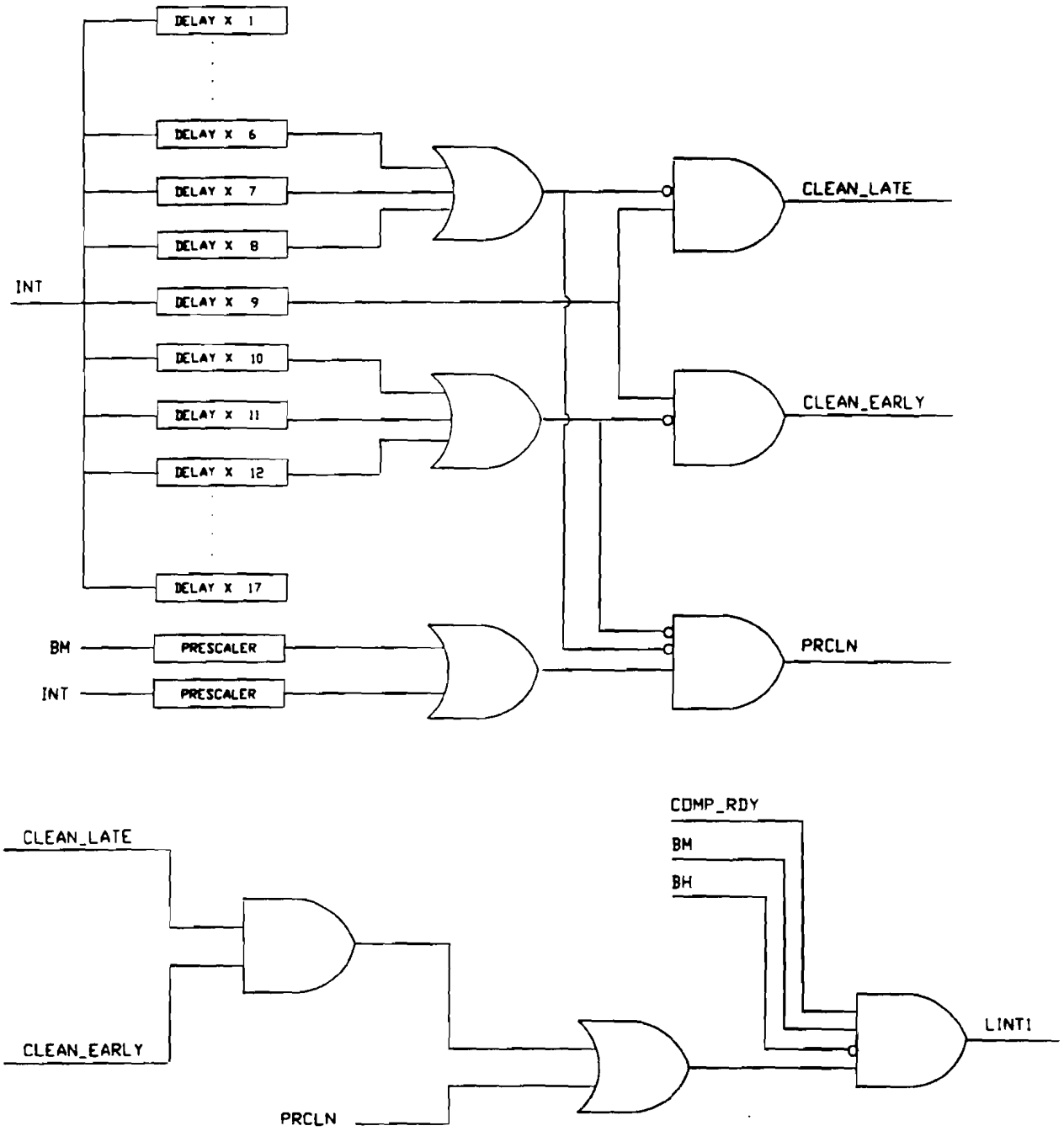

Figure 3.3: Early/Late filter and Live Interaction definition diagrams.

window, to require that no other interaction had been defined within ± 60 ns of the present interaction. According to this choice, in EARLY it was required that, when the strobe signal arrived, no interaction signals were present in the inputs corresponding to the 10, 11 and 12 bucket delays. For LATE the same requirement applied for the inputs corresponding to the 6, 7 and 8 bucket delays. Two signals, CLEAN_EARLY and CLEAN_LATE, were produced reflecting the satisfaction of these requirements. A diagram of the early/late filter is shown in figure 3.3.

To study the trigger bias, prescaled beam (PRBM) and prescaled interaction (PRINT) signals were generated. PRBM was produced by sending BM through a CAMAC 4431 unit set to prescale by a factor of 2.25×10^6, and to generate PRINT, INT was prescaled by 2.25×10^5. The outputs from the two prescalers were fanned out and sent to the Faraday room and to a NIM 365 logic unit where a logical OR of the two prescaled signals was performed. The output from the 365 was used to clear and then strobe a 4508 PLU into which the six delayed INT outputs used in the early/late filter logic described above were input. If none of the six inputs was present when the PLU was strobed, a signal called PRCLN was produced.

The final step in the definition of a triggerable interaction, labeled LINT1, was done using an additional 4508 PLU cleared and strobed by BM. The inputs to this unit were COMP_RDY, the discriminated BH signal, CLEAN_EARLY, CLEAN_LATE and PRCLN. LINT1 was defined as

$$\begin{aligned} \text{LINT1} = \text{BM} * \overline{\text{BH}} * \text{COMP_RDY} \\ * [(\text{CLEAN_EARLY} * \text{CLEAN_LATE}) + \text{PRCLN}] \end{aligned} \tag{3.4}$$

LINT1 was sent through a fast cable to the Faraday room where it was used in the preselection of the high transverse momentum events.

The veto wall, described in chapter 2, consisted of two parallel overlapping layers of 32 scintillation counters each. The signals from each of the counters were passed through an amplifier, and then discriminated in a time over threshold mode. The discriminated veto wall signals were timed with respect to each other and then fanned out. They were sent to OR logic units where the logical OR of the signals from the eight counters belonging to the same veto wall quadrant was performed. The eight logical ORs were then input into a 4508 PLU, cleared and strobed with RF clock pulses, where several logic combinations of the signals were made. The outputs from the veto wall PLU were passed through a prescaler set to prescale by a factor of 10, and then to a scaler. One of the output signals was also sent to the Faraday room to be used as a muon vetoing signal. The vetoing signal (VW) chosen was defined as

$$VW = VW1OR * VW2OR \tag{3.5}$$

where VW1OR is the logical OR of the 32 counters in the first (upstream) veto wall layer, and VW2OR is the logical OR of 32 counters in the second layer.

3.4 Event Selection

The electronics used in the selection or rejection of an event was installed in the Faraday room. It was in this section of the trigger system where the processing of the EMLAC signals was performed, and where the communication with experiment E672 occurred. The selection of an event is discussed in detail in what follows.

The P_T system

The weighing of the energy deposited in the LAC was done using custom made p_T weighting cards designed to work within the MX/RABBIT system framework.

The inputs to these cards were taken from the fast outputs of the LACAMP modules connected to the R-channels in the electromagnetic calorimeter (see chapter 2). The fast output was derived from the amplifier output received directly and out of the tap (180 ns) of the delay line. The op-amp subtracted the output from a delayed copy of itself and the delay line differentiated signal was routed to a single multipin connector on the front panel from where it was taken to the trigger summing cards.

There were a total of 16 p_T summing cards per octant, 8 for the front section of the EMLAC and 8 for the back section, with 32 input channels per card. The signals from adjacent channels were added in pairs, i.e., channel 0 + channel 1, channel 2 + channel 3, etc. The sum of two channels was then passed through an eight bit attenuator which was controlled by a Digital to Analog Converter (DAC). Each attenuator was programmed to correct for gain variations and to weigh the energy in the channel. The weight applied in a particular channel depended on which EMLAC R-strip was connected to it, and was proportional to $\sin\theta$ where, for strip i,

$$\sin\theta_i = \frac{r_i}{Z_{lac}} \tag{3.6}$$

In equation (3.6), Z_{lac} is the distance from the target to the first EMLAC anode board (~ 900 cm), and r_i is the radius of strip i in the first R anode board. The outputs from the attenuators were summed in groups of four to create signals corresponding to the p_T contained within groups of 8 strips; a sum of 32 channels was produced as well. A diagram of the summing card is shown in figure 3.4.

The sums of 8 channels from the summing cards were fed into two local discriminator modules. In each of these modules, sums of channels from the front of the EMLAC were added to the sums of the corresponding channels in the back.

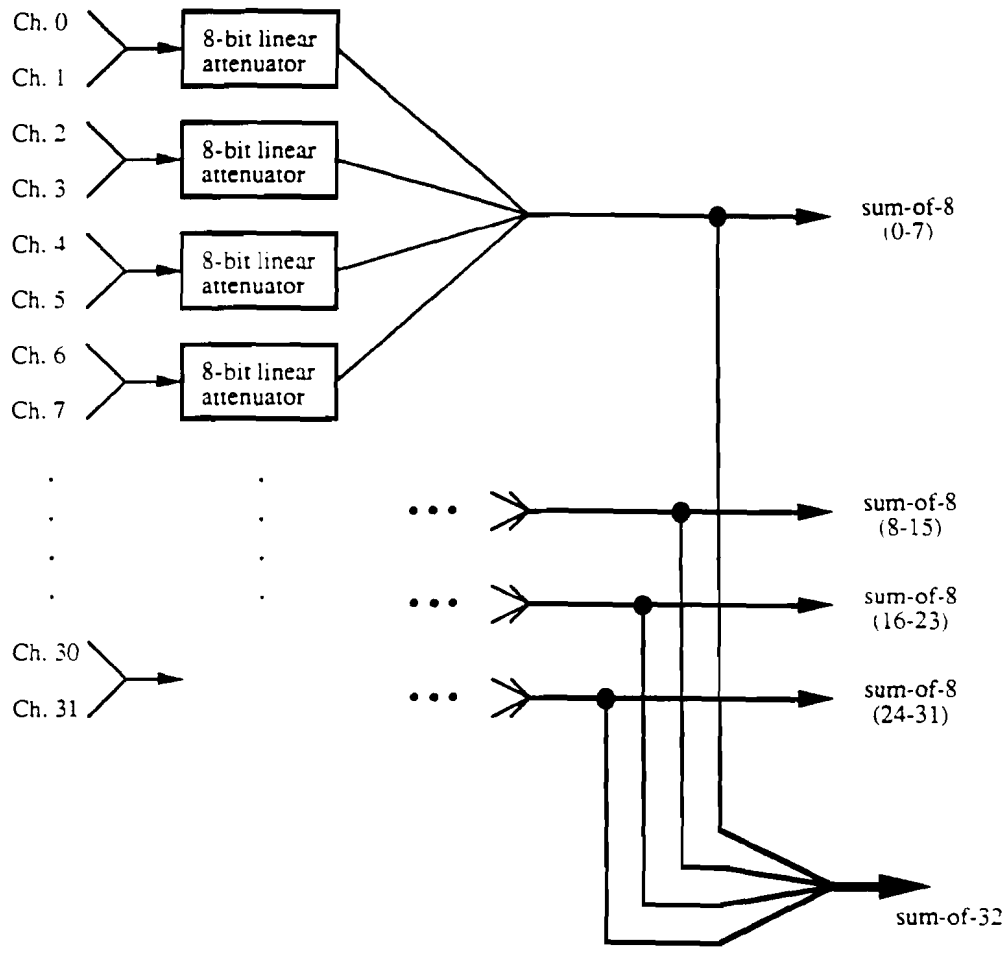

Figure 3.4: E706 P_T Summing Card.

Using the 8-channel sums (front and back added together), overlapping p_T sums of 16 adjacent channels were made and passed through discriminators whose thresholds were controlled by 8-bit DACs (see figure 3.5). When a p_T sum of 16 channels exceeded the discriminator threshold, a corresponding local p_T logic signal was generated in a time-over-threshold mode. The individual local p_T signals in an octant were transmitted as differential ECL signals through two 34-pin ribbon connectors.

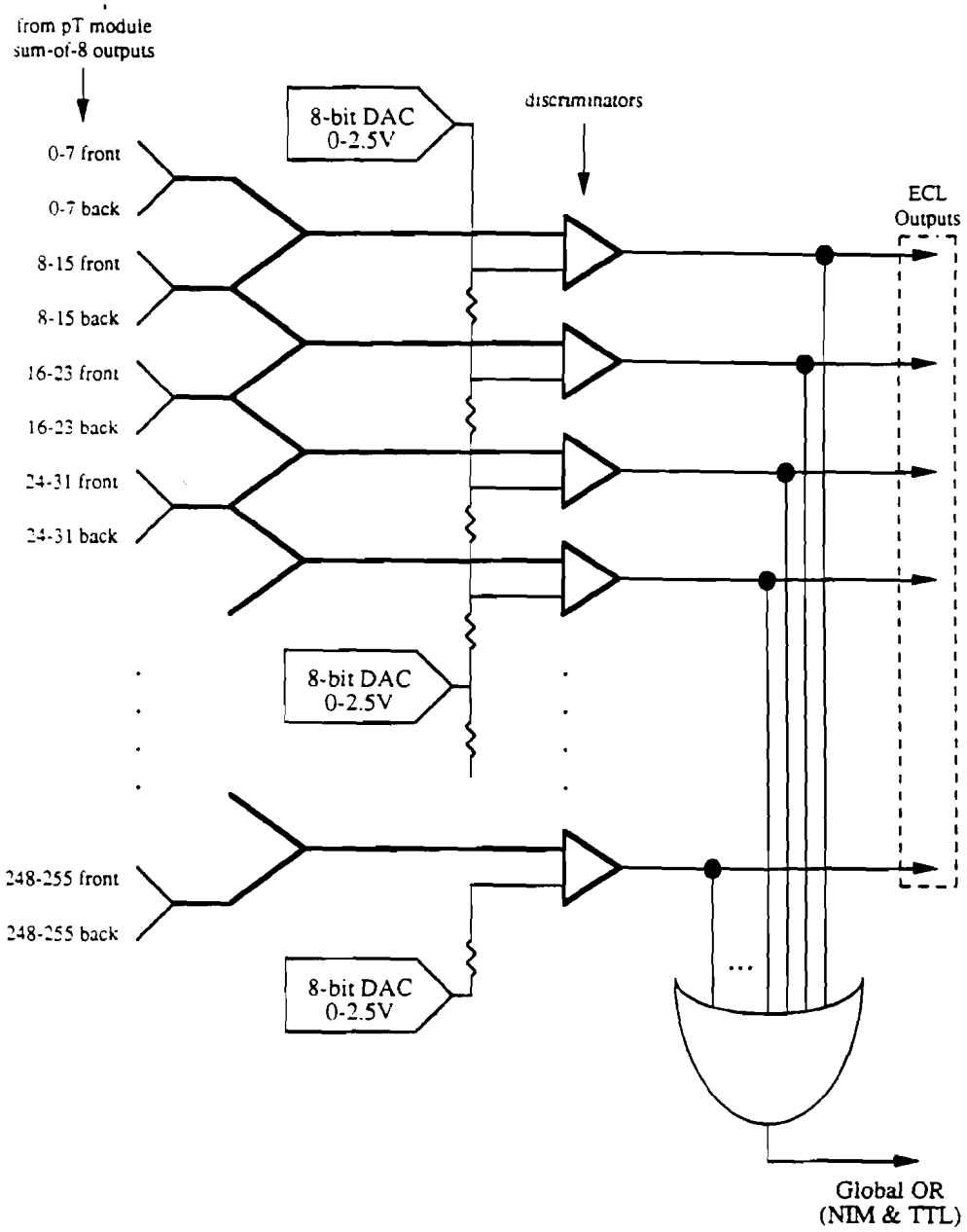

Figure 3.5: E706 Local P_T discriminator module.

A LOCAL P_T signal for the octant was produced by performing the logical OR of all the local p_T signals and transmitted as both NIM and TTL outputs. The two discriminator modules had different DAC settings and thus, for each octant, two LOCAL P_T signals were generated: LCLHI, which satisfied the high local threshold,

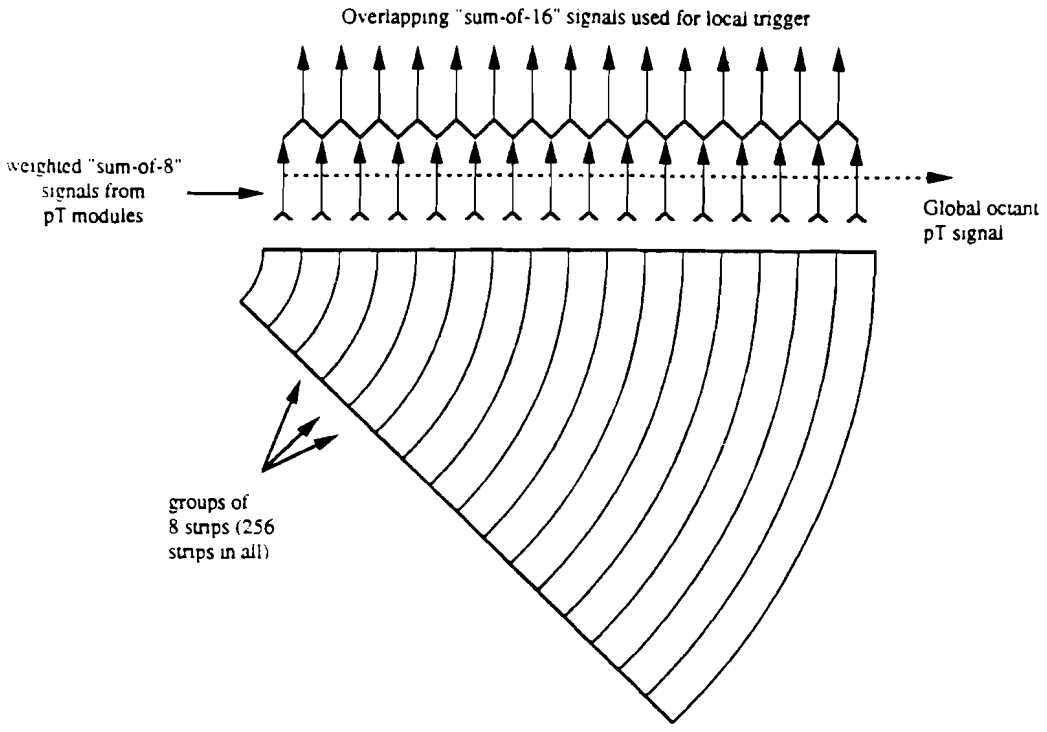

Figure 3.6: E706 Octant P_T Signal Summing.

and LCLLO, which satisfied the low threshold setting.

The sum of 32 channels from the summing cards were also sent into another summing card where the sums of channels in the front were added to the sums of the corresponding channels in the back. Finally, separate analog signals corresponding to the global p_T sums of the innermost 96 R-strips, the next 128 R-strips, and the outermost 32 R-strips were made and transmitted through three different outputs. The LCLHI and LCLLO NIM outputs and the three global p_T analog signals were sent via fast cables to the trigger logic electronics section for further use. Figure

3.6 summarizes the processing of the LAC energies to generate p_T signals.

Image Charge

An unforseen feature of the electromagnetic calorimeter, related to the presence of image charge, complicated the formation of the p_T sum signals, affecting the performance of the experimental trigger.

In the EMLAC, charge was collected by creating an electric field between the lead plate and the readout strips separated by the argon gap (see description of the EMLAC in chapter 2). When a shower was generated inside the calorimeter and ionization occured, the electrons from the electron-ion pairs drifted toward the readout strips thus inducing a current. Ideally, this current was to have flowed to the charge integration amplifier through the signal cables, and returned via the ballast capacitors attached to the high voltage lead plates, as shown in figure 3.7.

After the LAC system was sealed and filled with liquid argon, it was found that, due to impedances in the ground path between the amplifiers and the ballast capacitors, current tended to flow through the amplifiers connected to the other strips in the octant during the early stages of the pulse formation ($\sim$200 ns).† The charge supplied by the ballast capacitor to compensate for the charge loss, flowed at a later time causing more small current signals in the amplifiers in the octant.

This feature of the detector had a serious effect in the trigger performance because, when energy was deposited in a given group of strips, signals of opposite sign were induced in all other channels. At the individual channel level, this "image charge" signal had a negligible effect, but when the signals were added together by

† Recall that the signal to be used by the trigger was taken from the 180 ns delay tap.

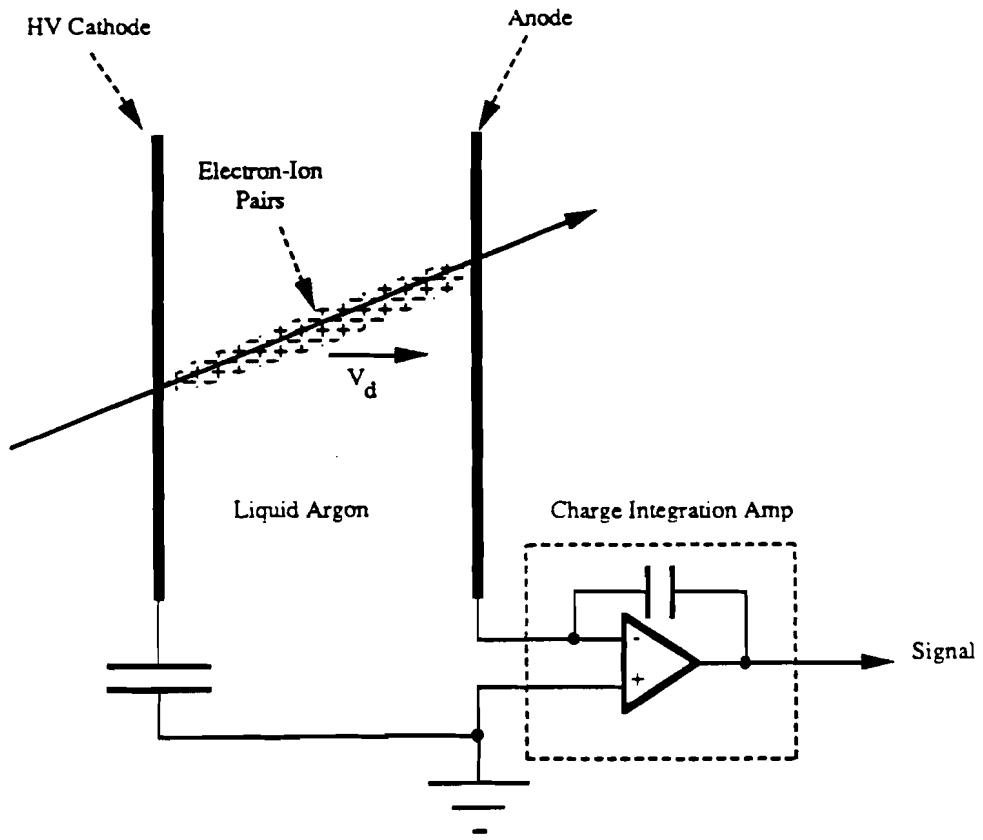

Figure 3.7: EMLAC charge collection.

the p_T summing cards, it posed a major problem since the signal from the strips that contained the shower was being summed together with the signal from the strips which only had charge of the opposite sign. This effect is shown in figure 3.8. In this figure, the top curve corresponds to the p_T signal from the shower, the middle curve corresponds to the image charge induced in the other strips, and the bottom curve shows the sum of the two signals. An additional complication to the problem arose from the fact that both the strip area and the weight applied ($\sin\theta$) increased as a function of the radius, making the image charge contribution from

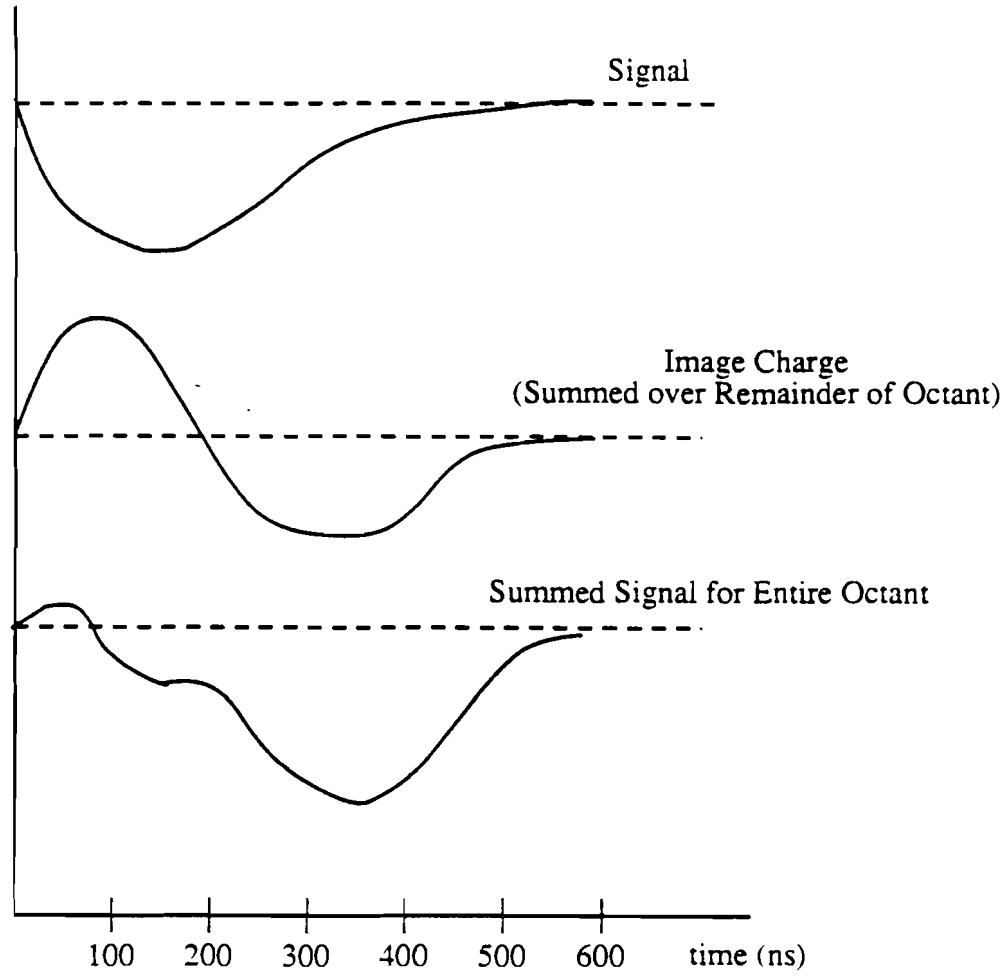

Figure 3.8: Effects of the image charge on the global p_T signal. The top curve corresponds to the p_T signal from the shower. The middle curve corresponds to the image charge induced in the strips away from the shower. The bottom curve is the sum of the two signals, and corresponds to the global p_T signal as seen by the trigger.

the outer strips larger. The net effect was an attenuation of the p_T signal with a change in its rise time, to the point where in some instances the p_T signal was

effectively nullified.

In the case of the local p_T signal, the image charge effects were not so drastic because only 16 strips were used in the sum. For the global $p_T$signal the situation was more critical since all strips were added together. In an attempt to deal with the problem, cutoff diodes were installed in the second stage summing cards where the sums of 32 channels were to be added together. The effect of the diode was to cutoff any positive going signal (recall that the p_T signals are negative) from the sums of 32 strips. The image charge effect was not completely eliminated however, because the diodes had a turn-on voltage which allowed for a small positive signal. Because the effects from image charge in the outer region of the detector were found to be drastic, the outermost 32 EMLAC radial strips were removed from the trigger.

Pretrigger

Using a combination of NIM 428 linear fan-in/fan-out units, the following analog global p_T signals were generated to be used at different stages in the event selection:

$$\mathrm{glpt13} = \sum_{i=0}^{95} p_{Ti} \tag{3.7}$$

$$\mathrm{glpt47} = \sum_{i=96}^{223} p_{Ti} \tag{3.8}$$

$$\mathrm{glpt17} = \sum_{i=0}^{223} p_{Ti} \tag{3.9}$$

with

$$p_{Ti} \propto E_i \sin\theta_i \tag{3.10}$$

where i is the R-strip number, E_i is the energy deposited in strip i, and $\sin\theta_i$ is

given by equation (3.6). Signals glpt13 and glpt47 are essentially the same signals produced by the summing cards, and glpt17 is a linear fan-in (sum) of the two.* Copies of each octant's glpt13 and glpt17 signals were sent to LeCroy 2249 ADC units to be digitized. When the event was selected, the information from these ADC units was stored on tape.

To preselect the event as a high p_T candidate, each octant was examined to determine if (1) the total amount of p_T deposited in the octant was larger than $\sim 1.7\,\mathrm{GeV/c}$, (2) the energy deposition in the octant was time correlated with the current interaction and, (3) the transverse momentum detected in the octant during the preceeding 300 ns was not larger than 1.5 GeV/c.

To decide if (1) and (2) were satisfied, zero-crossing discriminators were used. Because of the effects of the image charge on the timing of the global p_T signal, each octant was subdivided into two regions, one including the innermost 96 strips and the other including the other 128 strips, and each region was used separately. Accordingly, glpt13 and glpt47 were sent to separate zero-crossing discriminators. These discriminators had a threshold setting of $\sim 1.7\,\mathrm{GeV/c}$ and used a clip of $\sim 90\,\mathrm{ns}$. The discriminated output pulse, when produced, was 150 ns wide and was used to determine if the p_T signal was correlated in time with the interaction. The outputs corresponding to the two input signals were GLPT13 and GLPT47. A third signal, GLOBPT, was generated by a NIM 622 logic unit where the logical OR of GLPT13 and GLPT47 was executed. Signal glpt17 was used to establish if requirement (3) was satisfied. A copy of this signal was discriminated on a time over threshold fashion using a CAMAC 4416 updating discriminator. The threshold in

* The signals suffered some attenuation going through the NIM 428 units.

this unit was set to 1.5 GeV/c and the discriminated output was delayed by 300 ns using CAMAC 4418 delay modules.

GLOBPT and the delayed discriminated signal (EARLYPT) were sent into a self clearing 4508 PLU (GLBTIM) strobed by LINT1. For each octant, an output labeled OCTPRET (octant pretrigger), was generated. OCTPRET was defined as

$$\mathrm{OCTPRET} = \mathrm{LINT1} * \mathrm{GLOBPT} * \overline{\mathrm{EARLYPT}} \tag{3.11}$$

The EARLYPT requirement was to protect from pile-up effects resulting from the relatively slow response of the LAC readout electronics. The octant pretriggers were OR'ed to generate LACTIM. LACTIM was used in the second step of the event preselection.

$$\mathrm{LACTIM} = \sum_{i=1}^{8} (\mathrm{OCPRET})_i \tag{3.12}$$

Once the LAC information was processed for possible octant pretriggers, an additional step was done to preselect or reject the event. This step was executed using PRETRIGGER LATCH, a 4508 PLU strobed with LINT1 and cleared with CLEAR1 (CLEAR1 was a reset signal generated depending on the satisfaction of the logic requirements and its meaning will become apparent later on). The inputs to PRETRIGGER LATCH were the following:

— LACTIM

— VW: the signal from the latch house. This signal was passed through an updating discriminator. The output from the discriminator was set to be 150 ns wide and timed with respect to LINT1 (the timing proved to be tricky because of the randomness of the VW signals).

— SCRKILL: a 30 μsec wide signal generated by noise spikes caused by the 400 Hz power supplies in the Faraday room.

— PRBM and PRINT: defined above.

— 672CAND: this was a signal sent by the E672 trigger processor to indicate that the event was a DIMUON trigger candidate.

Depending on the inputs, three different pretriggers could be produced with the following definitions (see figure 3.9):

$$\begin{aligned} \text{LACPRET} &= \text{LINT1} * \text{LACTIM} * \overline{\text{VW}} * \overline{\text{SCRKILL}} \\ \text{PRPRET} &= \text{LINT1} * (\text{PRBM} + \text{PRINT}) * \overline{\text{SCRKILL}} \\ \text{672PRET} &= \text{LINT1} * \text{672CAND} * \overline{\text{SCRKILL}} \end{aligned} \tag{3.13}$$

LACPRET was generated if any of the octants had a pretrigger and VW and SCRKILL were not present. Four copies of LACPRET were produced and later used in the logic definitions of the different LAC triggers. If any of the prescaled signals or E672CAND was present in the absence of SCRKILL the corresponding pretrigger was produced. If the logic requirements for any of the three pretrigger logic signals defined in equation (3.13) were satisfied, a fourth signal, PRETRIG, was produced; if none of the pretriggers was satisfied, signal NOPRET was generated. These two signals were defined as:

$$\begin{aligned} \text{PRETRIG} &= \text{LACPRET} + \text{PRPRET} + \text{672PRET} \\ \text{NOPRET} &= \overline{\text{PRETRIG}} \end{aligned} \tag{3.14}$$

The output signals from PRETRIGGER LATCH were sent through two CAMAC 4431 prescalers to control the different trigger rates. NOPRET, was input into a NIM 622; when no pretrigger had been found, NOPRET caused the 622 unit

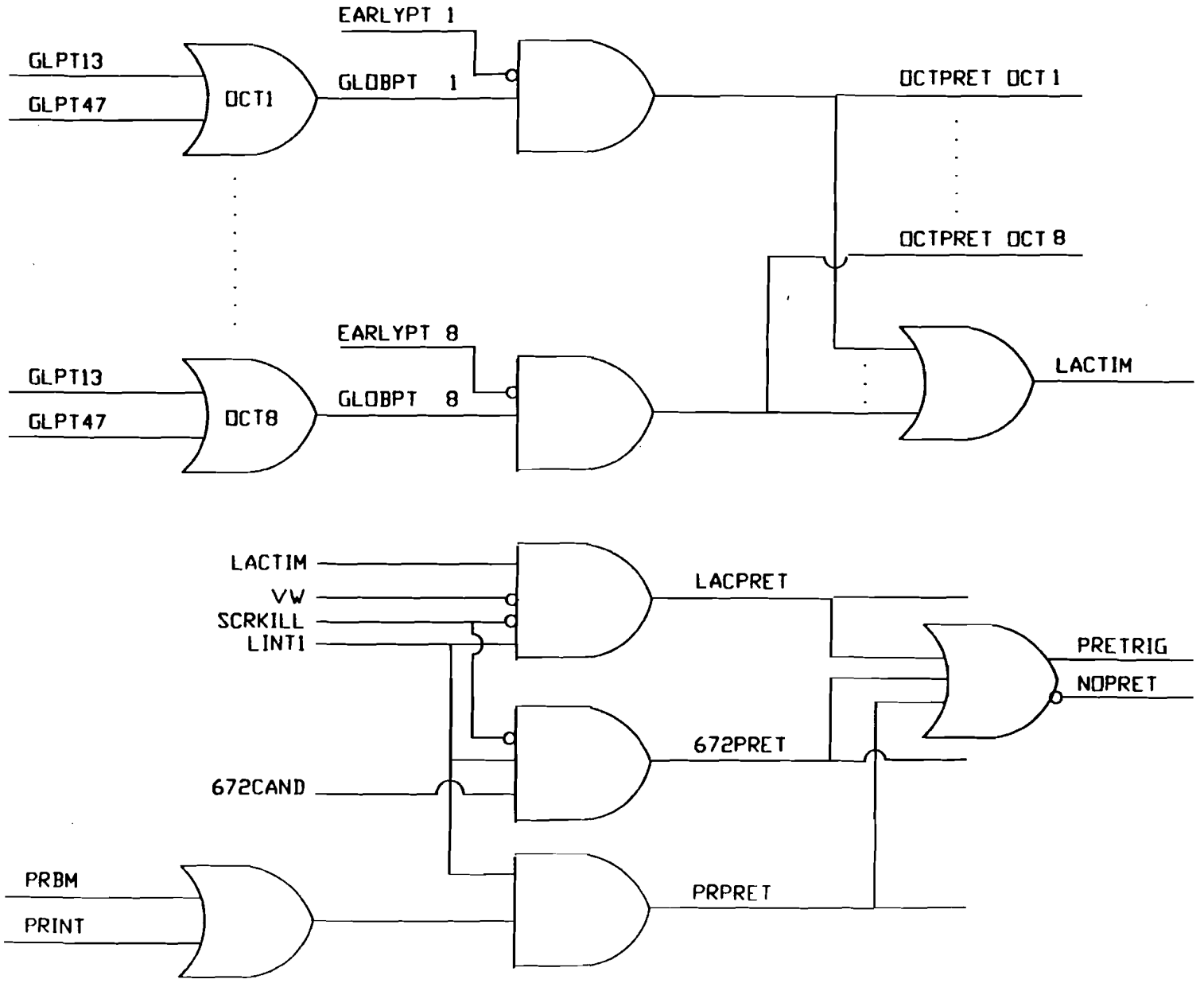

Figure 3.9: Pretrigger Logic diagram.

to produce a reset signal, labeled CLEAR1. CLEAR1 was in charge of resetting PRETRIGGER LATCH and thus enable the system to start the preselection process for the next event. If any pretrigger had been produced, PRETRIG generated the LOAD signal sent to the PWC/SSD, the FCAL and the E672 latches, and the EVENT signal propagated to the different BATs; the next step was to determine if a final trigger combination was satisfied.

Trigger and Readout

Seven trigger combinations were implemented during the 1987-1988 data run. Three of them were related to PRBM, PRINT and 672CAND, and were automatically satisfied when the associated pretriggers were generated. The other four triggers had requirements on the electromagnetic transverse momentum (LAC triggers). The conditions for the four LAC triggers were evaluated separately for each octant before the final trigger decision was made. Three of the LAC triggers, LGHI, LGLO and SLOC could be satisfied by any individual octant while the fourth one, TWOG, required at least two octants. For the evaluation of the requirements, each of the four triggers had a copy of LACPRET assigned to it, and they were all evaluated in two steps.

The four LAC triggers used combinations of four signals: LCLHI, LCLLO, GLBHI and GLBLO. LCLHI and LCLLO were defined above. The other two signals were generated by discriminating two copies of glpt17 using separate CAMAC 4416 discriminators. The two discriminators had different threshold settings and were used in a time over threshold mode. GLBLO was generated when glpt17 satisfied the lower threshold; if it satisfied the high threshold, GLBHI was produced. The local and global p_T discriminator thresholds were changed at different times during

List of threshold settings					
Early P_T	GLB P_T HI	GLB P_T LO	LCL P_T HI	LCL P_T LO	Date
	5.0 GeV/c				11-04-87
		3.0 GeV/c			11-14-87
			1.6 GeV/c	1.2 GeV/c	12-01-87
1.5 GeV/c					12-02-87
	4.0 GeV/c	2.5 GeV/c	4.2 GeV/c		01-08-88
			3.6 GeV/c		01-23-88
	3.6 GeV/c				01-23-88
			3.0 GeV/c		02-11-88

Table 3.1: Trigger threshold settings.

the data run. Table 4.1 lists the different threshold settings and the dates when they were implemented.

For the LGHI trigger, the first requirement to be satisfied by any octant was the existence of both the octant LCLLO and GLBHI signals. The coincidence of the two signals was examined in a 4508 PLU strobed by LACPRET and cleared by CLEAR2 (see below). If the coincidence was satisfied, a signal was produced and sent to a second 4508 PLU into which the corresponding octant OCTPRET signal was also input. The logic in the second unit was defined to produce an octant LGHI output signal (OCTLGHI), if both input signals were present when the strobe pulse arrived (the strobe was taken from the SYNC output of the first 4508 PLU). The LGLO trigger was processed in a similar fashion but using GLBLO and strobing with a LACPRET signal which was prescaled by a factor of 10.

$$(\mathrm{OCTLGHI})_i = \mathrm{LACPRET} * (\mathrm{OCTPRET} * \mathrm{LCLLO} * \mathrm{GLBHI})_i \qquad (3.15)$$

$$(\mathrm{OCTLGLO})_i = \mathrm{LACPRET} * (\mathrm{OCTPRET} * \mathrm{LCLLO} * \mathrm{GLBLO})_i \tag{3.16}$$

The third LAC trigger, SLOC, only required a high local p_T deposition. The evaluation of this trigger was done in a 4508 strobed by a third copy of LACPRET. This unit generated an octant SLOC trigger output (OCTSLOC) if, when strobed, the octant OCTPRET and LCLHI signals were present.

$$(\mathrm{OCTSLOC})_i = \mathrm{LACPRET} * (\mathrm{OCTPRET} * \mathrm{LCLHI})_i \tag{3.17}$$

To determine if any of the first three LAC triggers, LGHI, LGLO and SLOC, was satisfied, the logical OR of the corresponding octant triggers was performed:

$$\begin{aligned} \mathrm{LGHI} &= \sum_{i=1}^{8} (\mathrm{OCTLGHI})_i \\ \mathrm{LGLO} &= \sum_{i=1}^{8} (\mathrm{OCTLGLO})_i \\ \mathrm{SLOC} &= \sum_{i=1}^{8} (\mathrm{OCTSLOC})_i \end{aligned} \tag{3.18}$$

The processing of the signals to determine if a TWOG trigger existed was executed in two steps. First, in a 4508 PLU, strobed by a copy of LACPRET, each octant was searched to establish if its OCPRET and LCLLO signals were in coincidence with the strobe. An output reflecting the satisfaction of the coincidence, was produced for each octant and input into a second 4508 PLU, strobed by the pulse taken from the SYNC output of the preceding PLU. In the second step PLU, if any octant had satisfied the OCPRET*LCLLO coincidence requirement and any of the three octants geometrically opposite to it had satisfied the requirement as well, a

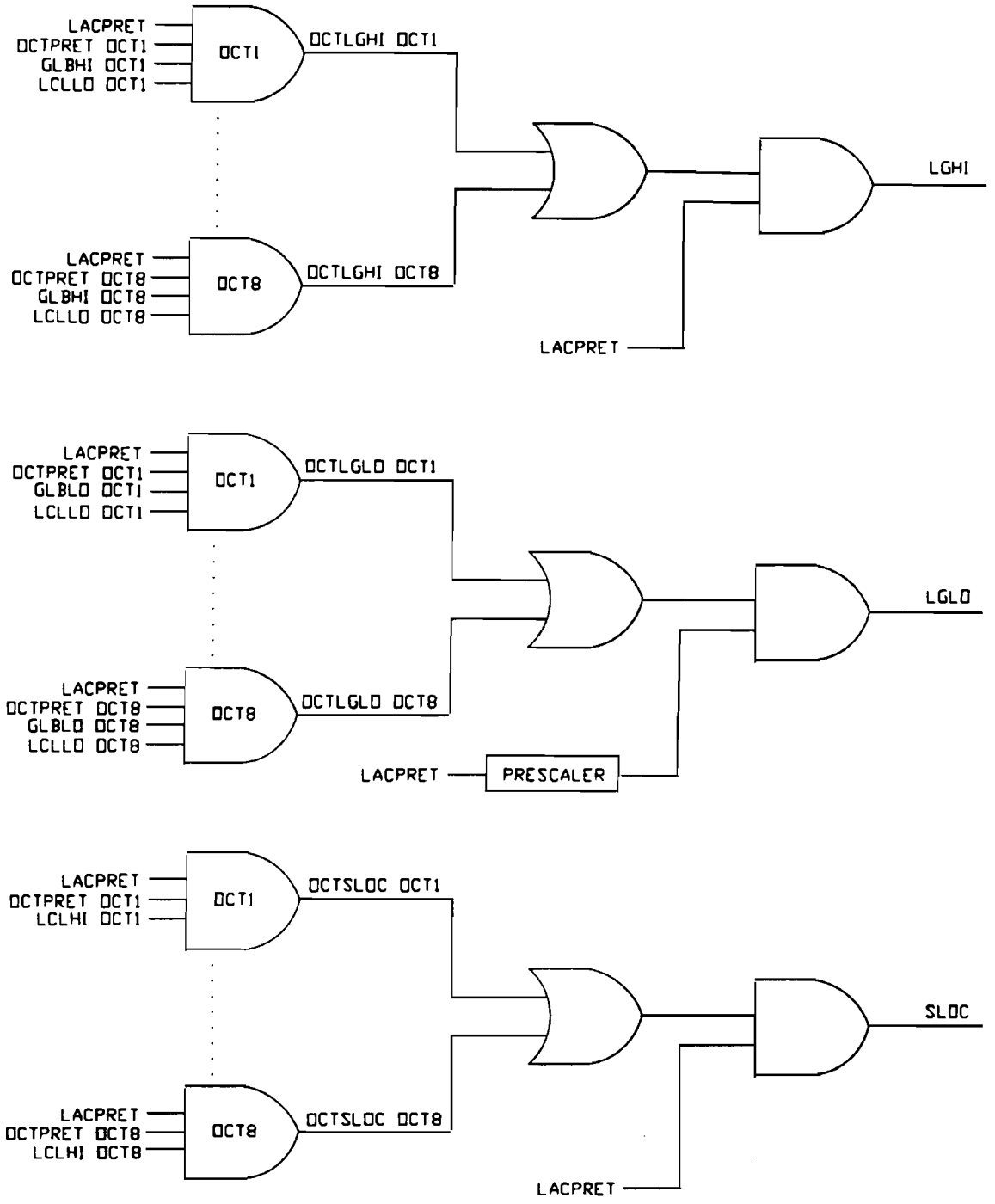

Figure 3.10: LGHI, LGLO and SLOC trigger diagrams.

TWOG trigger signal was generated.

$$\begin{aligned}(\mathrm{TWOG})_{\alpha\beta} &= \mathrm{LACPRET} * (\mathrm{OCTPRET} * \mathrm{LCLLO})_{\alpha} \\ &\quad * (\mathrm{OCTPRET} * \mathrm{LCLLO})_{\beta} \\ \mathrm{TWOG} &= \sum_{\alpha\beta} (\mathrm{TWOG})_{\alpha\beta}\end{aligned} \tag{3.19}$$

where β is any of the three octants geometrically opposite to octant α, and all possible $\alpha\beta$ combinations were used. A simplified version of the LGHI, LGLO, and SLOC triggers is shown in figure 3.10.

The four LAC trigger signals along with PRBM, PRINT, and 672PRET were input into a 4508 PLU strobed by PRETRIG, and in which a logical OR of the seven signals was performed, as shown in figure 3.11. Eight different outputs were produced by this unit. Four of the outputs were used in the final step to decide if the information for the event was to be stored:

$$\begin{aligned}\mathrm{TRIG1} &= \mathrm{PRETRIG} * (\mathrm{LGHI} + \mathrm{LGLO} + \mathrm{SLOC} + \mathrm{TWOG} \\ &\quad + \mathrm{PRBM} + \mathrm{PRINT}) \\ \mathrm{672TRG1} &= \mathrm{PRETRIG} * \mathrm{672PRET} \\ \mathrm{TRIGOR} &= \mathrm{TRIG1} + \mathrm{672CAND} \\ \mathrm{NOTRIG} &= \overline{\mathrm{TRIGOR}}\end{aligned} \tag{3.20}$$

NOTRIG was generated when no trigger had been satisfied after PRETRIG had been generated. NOTRIG was sent into a NIM 622 unit to generate a CLEAR2 signal to reset all the 4508 PLUs used after PRETRIGGER LATCH in the evaluation of the trigger. A reset signal was also sent to the PWC/SSD latches, the FCAL, E672, and the BATs. 5μsec later after allowing the electronic systems to

settle, CLEAR2 was input into the NIM 622 channel where NOPRET is sent and a CLEAR1 signal was then produced to reset PRETRIGGER LATCH and start the preselection process for the next event.

If a trigger was satisfied, TRIGOR strobed READOUT, the last 4508 PLU in the chain. Three signals were input into READOUT: TRIG1, 672TRG1 and 672TRG2. 672TRG2 was a second signal sent by E672 verifying that their event candidate was a good DIMUON event. To give the E672 trigger processor time to decide if the event was to be triggered on, TRIGOR was delayed up to 100μsec before strobing READOUT. When the 672 trigger decision was reached, signal 672DONE was received and used to stop the delay applied to TRIGOR, allowing the latter to strobe right away and thus reduce the trigger dead time. Two final outputs could be generated by READOUT (see figure 3.11):

$$\begin{aligned} \text{INTERRUPT} &= \text{TRIGOR} * (\text{TRIG1} + \text{672TRG1} * \text{672TRG2}) \\ \text{NOREAD} &= \overline{\text{INTERRUPT}} \end{aligned} \tag{3.21}$$

NOREAD was produced when no INTERRUPT was generated. It was sent to a NIM 622 unit to produce a CLEAR3 signal to clear READOUT. CLEAR3 was also sent into the same NIM 622 where NOTRIG was sent. The presence of a CLEAR3 generated a CLEAR2 and the rest of the system was reset in the fashion described above. When INTERRUPT was generated, it was transmitted to the Data Acquisition Control section of the trigger to instruct the subsystem computers to read the event information and store it in tape. After all the subsystems were finished reading the event, a computer RESET signal (which was also automatically produced at the beginning of each spill) was sent to the trigger section in the Faraday room. RESET was used to generate CLEAR3 and the trigger system was then reset as described above. Figure 3.12 shows a diagram describing the reset signal logic.

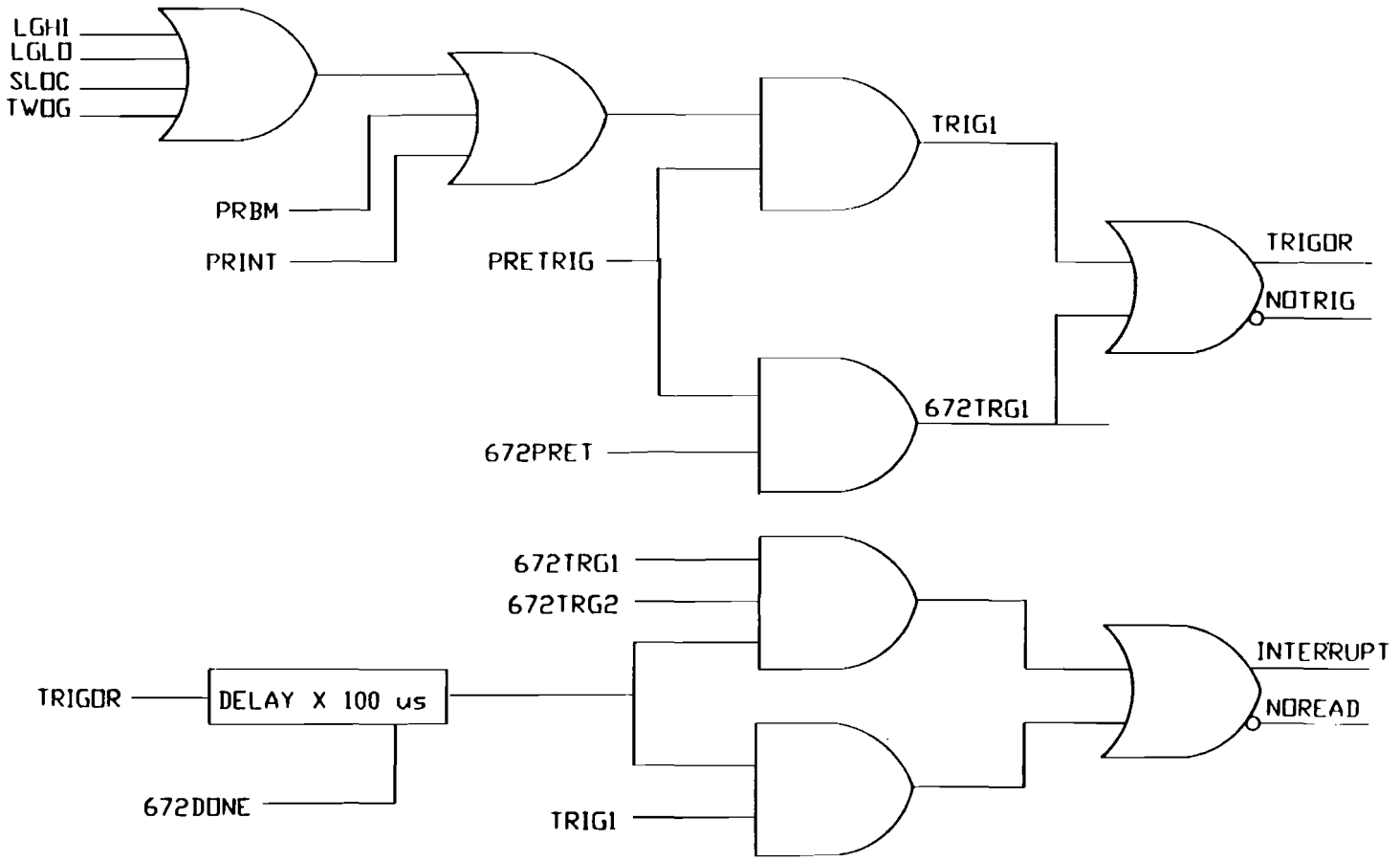

Figure 3.11: Final Trigger and Readout logic diagrams.

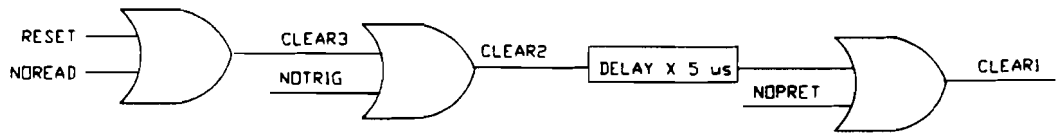

Figure 3.12: Trigger reset logic

For bookkeeping purposes, the number of occurrences of the different signals was scaled in LeCroy 4434 and LeCroy 2551 scalers. The 4434 scalers were read out at the end of each spill and then cleared. The 2551 units were also read out at the end of each spill but, unlike the 4434's, they accumulated information in a run by run* basis and were reset only at the end of each run.

3.5 Latches

In addition to performing basically any kind of logical operation on the inputs, a 4508 PLU also stores the input pattern in registers as soon as the strobe pulse arrives. The registers can be read through normal CAMAC operations. This feature was used to store information about the presence of the following signals in each event:

- LCLLO, LCLHI, GLBLO, GLBHI and OCTPRET for all octants.

* the meaning of the term "run" is explained in the Data Acquisition section of chapter 2.

- LCLLO * GLBLO, LCLLO * GLBHI coincidences in each octant.
- OCTLGHI,OCTLGLO and OCTSLOC octant triggers.
- LCLHI * OCTPRET and LCLLO * OCTPRET coincidences in each octant.
- The seven trigger combinations LGHI, LGLO, SLOC, TWOG, 672CAND, PRBM, PRINT.

A second kind of latches used were the Minnesota Latches.* These latches stored information at a frequency controlled by a clock. Each time the units were strobed by a clock pulse, also referred to as time tick, the input pattern was registered and stored in a buffer. The buffer saved the input patterns registered during up to 255 consecutive time ticks in an updating fashion. When an event was selected, a signal was sent to the latches to stop the clock and the buffers were accessed to read out the information corresponding to 15 selected consecutive time ticks (the maximum number of data words that could be transferred in one command); after being read out, the units were cleared and the clock restarted. Signals from the following counters were latched by these units:

- BA, BB, BH, SE1, SW1, SE2, SW2
- the 6 differential, the 6 anticoincidence and the 2 beam scintillation counters in the Cherenkov detector,
- the 64 VW counters.

The clock rate was controlled by the RF_clock, thus assigning each time tick to correspond to a beam bucket. The clock was started using CLEAR2 (described

* The Minnesota Latches were designed by P. Lukens and constructed by P. Lukens and R. Benson of the University of Minnesota.

above) and it was stopped by INTERRUPT. The clock was set up so that the fifteen time tick window chosen was centered around the triggering interaction.

4. EVENT RECONSTRUCTION

The overall software structure for the offline reconstruction of events is a program called MAGIC.* MAGIC is a Fortran-77 program which uses PATCHY,[21] a computer code management system developed at CERN. To overcome the lack of dynamic memory in standard Fortran, the CERN memory management system ZEBRA[22,23] is used in MAGIC. ZEBRA allows, at execution time, for the creation and manipulation of data banks whose size can be defined as needed for the event being processed. ZEBRA data banks can be written out in a machine independent format.

MAGIC provides a framework for the various subprograms used in the reconstruction process, and coordinates their execution. The tasks performed by MAGIC include: reading input data from disk or magnetic tape and from the databases, handling the memory management, unpacking the data and reconstructing the events, error reporting and diagnostic information, and writing the output to the selected output device. To date, MAGIC has been successfully implemented in DEC VAX, Fermilab Advanced Computer Project (ACP), and AMDAHL computers.

For each event, the unpacking and reconstruction of the the data from each of the detectors is performed separately by specialized subprograms. A brief description of the trigger, tracking and EMLAC data reconstruction is presented below.

* MAGIC was developed primarily by George Alverson and Edward Pothier of Northeastern University

A complete description of the HALAC data reconstruction is given in the Ph.D. dissertation by A. Sinanidis of Northeastern University.[24] The FCAL reconstructor is described in reference 18.

4.1 Discrete Logic Reconstruction

The Discrete Logic REConstructor (DLREC) made use of the trigger information latched by the 4508 PLUs and the Minnesota latches. DLREC performs the following tasks for each event:

- reconstruct the beam logic,
- find which octant(s) triggered the event and which LAC trigger the octant(s) was (were) part of,
- determine if any of the Veto Wall quadrants, geometrically corresponding to a LAC quadrant containing a triggering octant, has a signal and,
- reconstruct the LAC triggers to determine if there are discrepancies.

The beam reconstruction is done to determine (1) if both beam counters (BA and BB) had a signal, (2) if BH had no signal, (3) if the early/late filter was satisfied and, (4) which of the interaction counters fired. In addition, the Cherenkov information is used to determine which of the DnVm logic requirements were satisfied. Here, Dn indicates that at least n of the differential counters fired, and Vm means that less than m of the anticoincidence (veto) counters fired. In all cases m is set to 2, for n values of 2, 3 and 4.

The search for signals in the Veto Wall is done for a time span determined by the user via MAGIC user cards. The span is measured in ticks, each tick corresponding

to one beam bucket,* and can be as wide as 15 ticks. A search is performed to determine if a signal was latched for any of the 16 counters in a VW quadrant during the time interval selected. If a latched signal is found and the geometrically corresponding LAC quadrant has a triggering octant, a flag is turned on.

Finally, based on the information latched about the presence of pretriggers, local p_T HI/LO and global p_T HI/LO signals in each octant, a software reconstruction of the trigger logic is performed. The results from this reconstruction are compared to the actual trigger execution of the logic to determine if there are any discrepancies. The results from DLREC are stored in quality words, and in standard Fortran arrays (it is not necessary to use ZEBRA data banks for storage purposes in this case).

4.2 Tracking reconstruction

The reconstruction of data from the tracking system is done by a program known as PLREC.[35] PLREC reconstructs the tracks from the SSDs (upstream) and the PWCs (downstream) separately. To find the complete trajectories, upstream tracks are linked with downstream tracks at the magnet, taking into account the bending of the tracks due to the magnetic field. The final results from PLREC are then stored in data banks and ultimately written out to the output device.

The first step in the reconstruction of downstream tracks is to find view tracks in each of the four views (XYUV). To find a view track, two of the planes in the view are used as "seed" planes. A straight line is defined by a combination of two hits,*

* See description of the Minnesota latches in chapter 3.
* A hit in this case is defined as the view coordinate of a wire that fired when a charged particle passed close by.

one in each of the seed planes, and then projected onto the other two planes (the "search" planes). The search planes are searched for hits within ± 1.5 wire spacings of the line projection. If hits satisfying this criteria are found in both search planes, the track is called a four-hit track; if only hits in one of the search planes satisfy the requirement then the track is termed a three-hit track. The search for view tracks is done in two passes. In the first pass the outer planes are used as seed planes and in the second pass they are used as search planes. The second pass is executed to find three-hit tracks in which a hit from one of the outer planes is missing, whereas the first pass is expected to find the other three-hit tracks and all the four-hit tracks cases. In both passes all possible combinations of hits from the seed planes are used.

In the next step, PLREC proceeds to match the view tracks to form space tracks using a procedure similar to that described above. Two seed views are selected and a combination of two tracks, one from each seed view, is used to define a space track candidate. The space track candidate is projected onto each of the planes of the two search views, and a search is performed to find all hits within ± 1.5 wire spacings of the projection of the space track in all the search view planes. The hits found during the search and the hits that make up the seed view tracks are grouped as a set; this set of hits defines a space track if the following conditions are met:

- there are at least two hits in each view,
- there are at least four hits from all the search views,
- there is a minimum of six hits from the seed views, and
- there are at least thirteen hits in all.

As mentioned in chapter 2, three SSD modules are positioned upstream of the target to measure the incident beam particle trajectory, and the other four modules,

located downstream of the target, measure the trajectories of the produced charged particles upstream of the analysis magnet. In what follows, tracks related to the two groups of SSD modules will be referred to as beam and upstream tracks respectively. The reconstruction of beam and upstream tracks is performed in a similar fashion as for the downstream view tracks. An additional complication arises in the reconstruction of the upstream tracks however, because of the effects of charge sharing by adjacent strips in high multiplicity events. To reduce these effects, nearby hits are clustered to form equivalent single hits in those events.

Linking of the upstream and downstream tracks is accomplished by projecting the tracks to the longitudinal center of the aperture of the analysis magnet. Each downstream track projection is paired with all the upstream track projections and the spatial and bending angle difference in each paired projection is measured to find the best match. If this best match satisfies a predetermined cut, it is called a linked track. The momentum components (p_x, p_y, p_z) of the linked track and its charge q can be found using the following recipes:

$$q = \frac{\theta_1 - \theta_2}{|\theta_1 - \theta_2|}\frac{B}{|B|} \tag{1.11}$$

$$\sqrt{p_x{}^2 + p_y{}^2} = qBL_o/(\sin\theta_1 - \sin\theta_2) \tag{1.11}$$

$$p_x = p_z \tan\theta_1 \tag{1.11}$$

$$p_y = p_z \tan\theta_y \tag{1.11}$$

where θ_1 and θ_2 are the angles, relative to the Z-axis, of the particle trajectory projection onto the XZ-plane at the entrance and exit of the magnet, B is the strength of the magnetic field, L_o is the length of the magnet, and θ_y is the angle of the projection of the trajectory on the YZ plane, relative to the Z-axis.

Once the track reconstruction is completed, vertex reconstruction is carried out. For vertex definition, four-hit upstream tracks that are properly linked with downstream tracks are used. If no such tracks exist, all four-hit upstream tracks are used provided there are at least four of them; if fewer than four are found, the algorithm uses all three-hit linked tracks. The vertex is obtained by projecting the selected tracks to the target, and applying a χ^2minimization procedure to find the spatial coordinates of the point that minimizes the average impact parameter of the track projections.* After each minimization, the track with the largest impact parameter is eliminated from the set of selected tracks, and the process is repeated until the average impact parameter of all the tracks associated with the vertex is less than 20μm or the largest impact parameter for any single track is less than 50μm or there are only two tracks left.

Figure 4.1 shows a distribution of the reconstructed vertex Z-position. The segmentation of the target is clearly visible in this figure. The resolution of the vertex Z-position was measured to be $\sim 600\mu$m, and the resolution in the X-Y positions was determined to be $\sim 21\mu$m.[26]

4.3 EMLAC DATA RECONSTRUCTION

The reconstruction of the EMLAC event information is done by a program called EMREC. A complete description of EMREC can be found in the Ph.D. dissertation by J. P. Mansour of the University of Rochester.[27] The reconstruction is executed in a quadrant by quadrant basis. Each quadrant is subdivided into four views: views 1 and 2 correspond to the radial views in each octant; view 3 is assigned to the

* The impact parameter is the normal distance from the projection of the track to the candidate vertex position.

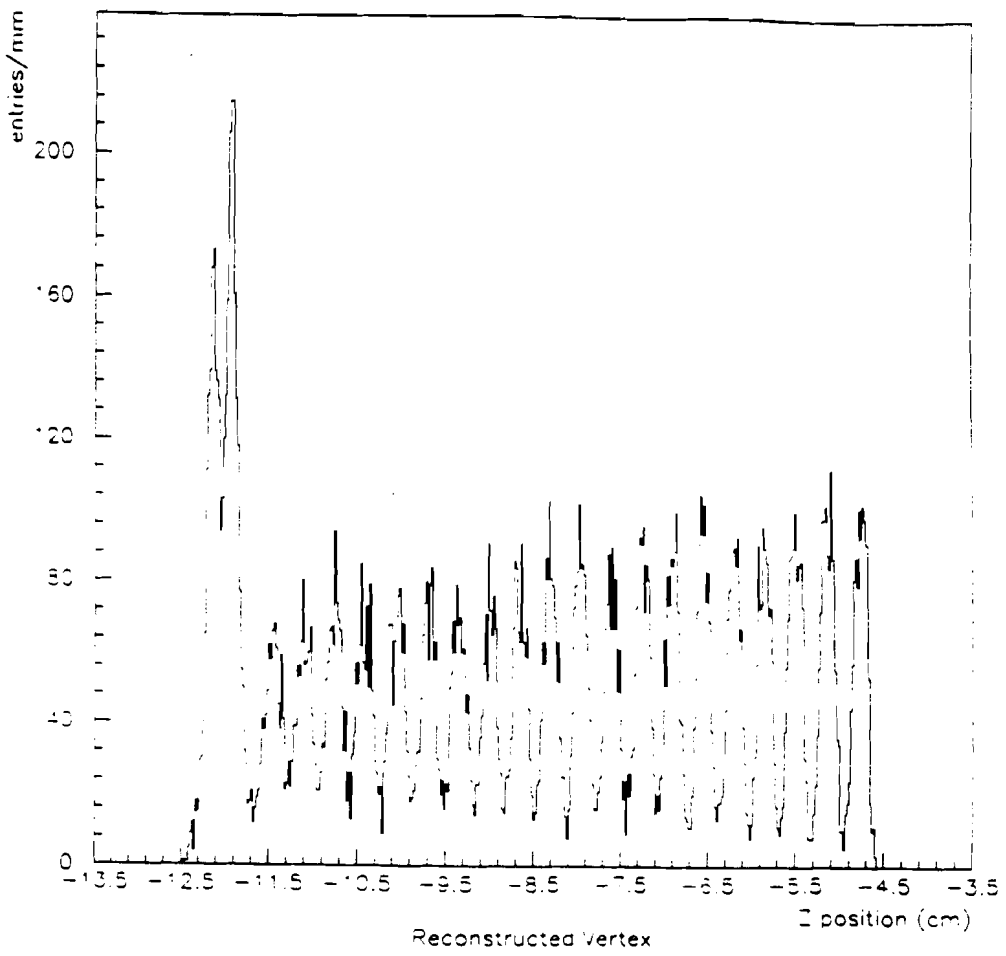

Figure 4.1: Reconstructed vertex Z–position

inner Φ strips and view 4 to the outer Φ strips (see chapter 2). The reconstruction is performed in four steps: (1) group and peak finding, (2) fitting of peaks found in (1) to photon shower shapes, (3) correlation of the reconstructed showers in the R and Φ views to form the final photons.

Before the EMLAC data is reconstructed, the information stored in ADC counts is converted to units of energy. The conversion is done using the relation

$$E_i = A_i G_i (N_i - N_{oi}) \tag{4.1}$$

where i identifies the channel, A_i is a normalization factor, G_i is the relative gain for the channel, N_i is the ADC value, N_{oi} is the channel pedestal and E_i is the resulting energy value. The determination of the values for G_i, A_i and N_{oi} is described in reference 17.

As described in chapter 2, the EMLAC is divided longitudinally into front and back sections and the readout of signals from the two sections is done separately. Each section is reconstructed individually, thus providing information on radial positions and the fraction of the energy deposited in each of the sections of the EMLAC. In addition, the energies of corresponding front and back strips are summed, and the reconstruction is performed for the front and back sections added together. This sum is done to minimize the dependence of the shower shape on the point of origin of the shower.

The search for groups is done separately for each of the views defined above. A group is defined as cluster of consecutive strips which satisfy the following requirements:

- there must be at least 3 strips (2 in view 4) with energies above a software threshold (this threshold is set to 150 MeV by default but can be redefined via the user cards in MAGIC)
- the total group energy must be at least 750 MeV,
- the average energy per strip must be greater than 150 MeV and,
- the strip with the maximum energy must contain at least 300 MeV.

Once the group is defined, EMREC proceeds to search for peaks of energy within each group. The peak search is done for the summed sections and, to avoid losing

low energy peaks because of adding the front and back sections together, a search is done in the front section as well. When a peak candidate is found, the expected variance in the peak value is calculated by

$$\sigma = \sqrt{(0.14)^2 \, \mathrm{E} + (0.1)^2} \tag{4.2}$$

where E is the energy of the peak-strip, σ is the estimated energy variance for E, $0.14\sqrt{\mathrm{E}}$ gives the intrinsic energy resolution of the EMLAC due to shower sampling fluctuations (calculated using GEANT[26]), and 0.1 is the incoherent noise contribution to the total resolution. Associated to each peak are two valleys, one on each side of the peak. A valley is defined as the strip with the lowest energy deposited between two peaks, or the end strip in the group if the peak is the first, last or only peak in the group. In order for the peak to be accepted it is required that the energy difference between the peak-strip and each of its valleys is at least 2.5σ

Having found the peaks the next step is to find the position and energy of the shower in a view, by fitting the energy distribution using a parametrization of the photon shower shape.* For single peak groups the process is straightforward in that the position and energy calculations are unambiguous. The following description assumes this to be the case.

To find the position of the shower in a view the position of the center of the peak strip is determined. Then, based on weights determined according to the energies of the two strips neighboring the peak strip, a shift from the center is found and

* The parametrization of the shower shape was determined using the GEANT based E706 Monte Carlo program. The parametrization, given as a function of the radial distance to the center of the shower, is given separately for the front and back sections because the lateral spread of the shower is wider in the back.

a new position X is defined. The energy distribution is then fitted to the shower shape using three different locations, $X - 0.2, X$ and $X + 0.2$, and the χ^2 values of the fits are used to find the best estimate of the center of the shower. The energy of the shower is calculated by minimizing the χ^2 of the fit of the energy distribution to the shower shape. For the fit, only a number N_s of strips is used in order to prevent noise in the tails of the shower from affecting the fit. N_s depends on the strip energies and is calculated using a parametrization determined from Monte Carlo studies, in which N_s was shown to be the appropriate number of strips that could be used without having energy fluctuations in the tails affecting the χ^2 of the fit. After the number of strips is determined the χ^2, defined as

$$\chi^2 = \sum_{i=1}^{N_s} \frac{1}{\sigma_i{}^2}(e_i - Ez_i)^2 \tag{4.3}$$

is minimized with respect to the true energy E. In equation (4.3), e_i is the energy in strip i, z_i is the fraction of energy in strip i as predicted from the shower shape, and σ_i, defined by equation (4.2) for e_i, is the standard deviation for the the energy seen in strip i. The energy that minimizes the fit χ^2, E_{fit}, is then calculated and the amount of energy in the tails is computed as

$$E_{tail} = E_{fit}\left(1 - \sum_{i=1}^{N_s} z_i\right) \tag{4.4}$$

If the χ^2 is less than 5.0, the fit is deemed to be acceptable. Otherwise the energy is given as

$$E_{sum} = \sum_{i=1}^{N_s} e_i + E_{tail} \tag{4.5}$$

When more than one peak are present in a group the case is somewhat more complicated. The procedure is to apply a splitting algorithm to separate the showers

and then perform the calculations of the positions and energies for the corrected pulse distributions. After the splitting is done, EMREC proceeds to perform the process described above for single showers.

The next step in the reconstruction is to correlate showers in the R view(s) with showers in the Φ view(s) to form the final photons. The idea is to match a shower in one view with a shower in the other view that has approximately the same energy and a similar fraction E_{front}/E_{total} of the total energy deposited in the front section of the EMLAC. Although straightforward in conception, this is a complicated procedure when the showers are located near the octant and/or inner/outer Φ boundaries. The effects of these problems on the efficiency of the correlation, as well as the effects introduced by ambiguities in the splitting process, can be seen in the experimental distributions (see chapter 6).

Photon Arrival Time

The time of arrival associated with each photon, was calculated using the information stored in the TVCs (see chapter 2).

5. TRIGGER PERFORMANCE

Studies have been carried out to examine the performance of the different trigger combinations, using results from EMREC to measure the energy deposition, and DLREC to determine the trigger response. A trigger model that includes known weaknesses of the trigger hardware has been developed, but it does not include image charge effects. A model that includes image charge contributions is being developed at this time. One of the complications in developing a more complete trigger model arises from the fact that energy measurements in EMREC are affected by reconstruction efficiencies, and pedestal and gain fluctuations. It is important to efficiently handle the problems affecting the energy reconstructed by EMREC since image charge contributions to the amount of energy seen by the trigger, depend on the total energy deposited and its radial location.

The probability $P(r,p_T)$ that a trigger was satisfied by transverse momentum p_T deposited in the EMLAC as a function of the radial position "r", was represented by the convolution of a step function, representing the trigger discriminator threshold, and a gaussian smearing term, i.e.,

$$P(r, p_T) = \frac{N}{\sqrt{2\pi}\sigma(r)} \int_{-\infty}^{+\infty} dx\ \theta(p_T + x - \tau(r)) \times \exp(-x^2/2\sigma^2(r)) \qquad (5.1)$$

where

$$\theta(x - a) = \begin{cases} 0, & \text{if } x < a \\ 1, & \text{if } x > a, \end{cases} \tag{5.2}$$

$\tau(r)$ is the trigger threshold, and $\sigma(r)$ is the width of the smearing term. The smearing is caused by: (1) coherent noise in the detector, (2) strip-to-strip fluctuations in the relative gains and trigger weights, and (3) variation of the threshold as a function of the radial position which, as mentioned above, is affected by the image charge.

Results from the trigger studies showed that in addition to the image charge problem mentioned in chapter 3, the octant global p_T analog signals "glpt17" (equation 3.8) disappeared at random times, thus creating an additional inefficiency in the LGHI and LGLO triggers. The problem was tracked down to a failure in the NIM 428 units used to generate these signals; the units could not recover from positive going input signals fast enough, to the point where they would remain basically dead if the input rates were higher than $\sim$ 25 Hz. Signals "glpt13" and "glpt47" were not affected by the failure of the NIM 428s and therefore, neither were the pretrigger nor the SLOC and the TWOG triggers.

Because of the many subtleties involved in the generation and use of the global p_T signals, the SLOC trigger has been understood in more detail than the LGHI and LGLO triggers. In the following paragraphs, a summary of the results from the SLOC trigger and the pretrigger performance analysis is presented, along with a description of the performance of the Veto Wall. The latter is an important tool in the determination the muon contamination in our data sample.

5.1 Pretrigger

To measure the pretrigger efficiency, information from EMREC reconstructed groups was used. In order to select an unbiased data sample, events selected by the SLOC, the LGHI, or the LGLO triggers were used. In those events, the octants geometrically opposite to the triggering octant were examined to measure the energy deposited, and the pretrigger response to it according to the information reconstructed by DLREC. The calculation of the global p_T as the trigger would have measured it, was done by a software simulation of the summing process described in chapter 3.

The pretrigger efficiency for each of the two octant regions used in the pretrigger definition, was calculated by determining, as a function of p_T, what fraction of the time the pretrigger was satisfied. The inner region corresponds to the innermost 96 strips and the outer region covers the remaining 128 strips used. Fits to the efficiency distributions for each octant using equation (5.1), were performed to determine the corresponding set of values for τ, σ and N in the inner region. For the outer region, all octants were summed together due to statistical limitations, and the summed distribution was fit to find the corresponding parameters. Table 5.1 shows the results of the fits.

Figure 5.1 shows the pretrigger efficiency distribution for the inner region in octant 6 as a function of p_T. Figure 5.2 shows the pretrigger efficiency for the outer region of the LAC, in which all octants have been combined.

Octant	τ (GeV/c)	σ (GeV/c)	N
Inner Region			
1	1.950 ± 0.045	0.526 ± 0.052	0.98
2	1.852 ± 0.013	0.518 ± 0.025	1.00
3	2.016 ± 0.009	0.540 ± 0.022	0.97
4	1.894 ± 0.007	0.567 ± 0.022	0.98
5	2.108 ± 0.019	0.619 ± 0.026	0.98
6	1.842 ± 0.012	0.510 ± 0.033	0.96
7	2.214 ± 0.014	0.536 ± 0.024	0.95
8	1.621 ± 0.011	0.599 ± 0.022	0.95
Outer Region			
All	2.316 ± 0.020	0.7151 ± 0.040	0.83

Table 5.1: Pretrigger efficiency parameters

5.2 SLOC Trigger

To determine the SLOC trigger efficiency, all available events in which the TWOG trigger was satisfied were used. The TWOG trigger made use of the local p_T LO signal, and for the SLOC trigger the local p_T HI signal was used, both requiring the pretrigger to have been satisfied. From the individual octant point of view, both triggers are identical except for the threshold requirement. In this case, and provided the low threshold trigger is already 100% efficient at p_T values nearing the high threshold, the efficiency of the high threshold trigger can be found by measuring the ratio $L \cdot H/L$, where L is the number of times the low threshold trigger was satisfied and $L \cdot H$ is the number of times both triggers were satisfied simultaneously, as a function of p_T. The local p_T LO was measured to reach full

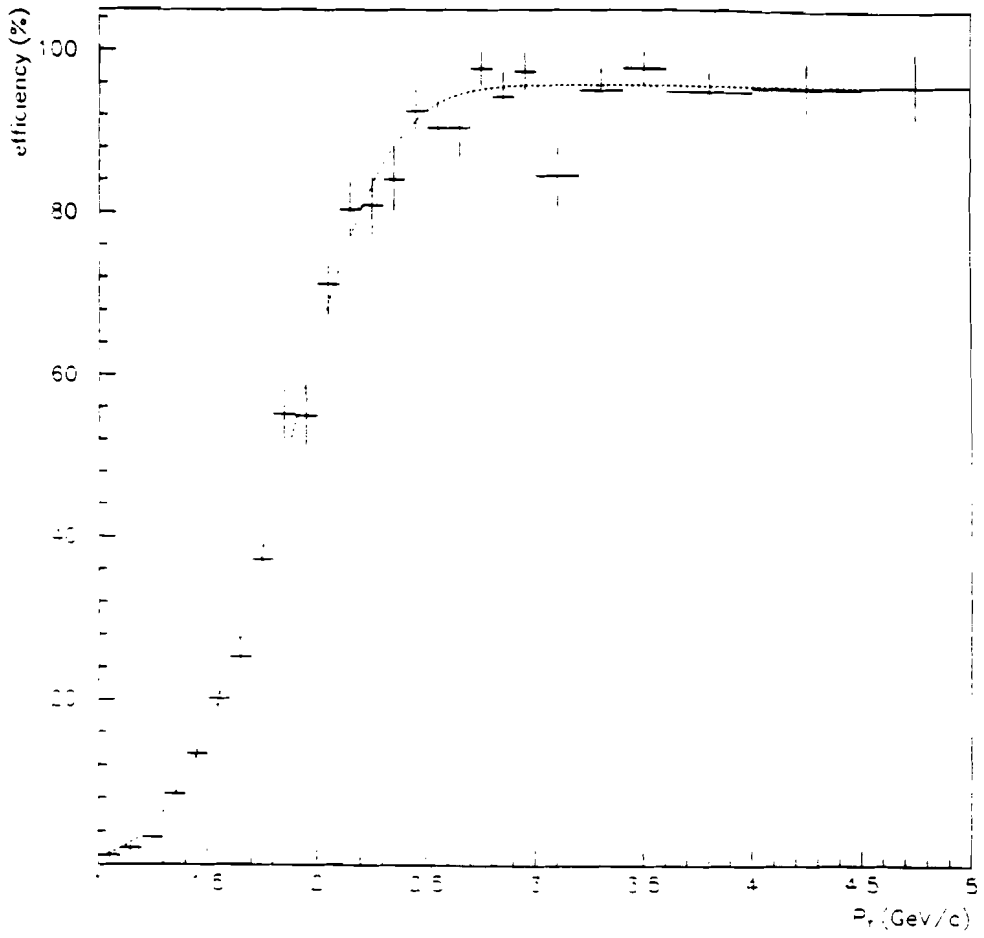

Figure 5.1: Octant 6 Inner Region Pretrigger Efficiency.

efficiency at 1.8 GeV/c, well below the threshold settings used by the SLOC trigger.

A software simulation of the trigger overlapping sums of sixteen channels was executed for the octants which satisfied the TWOG trigger. The p_T deposited in each local group was measured using the energy reconstructed by EMREC, and the group of 16 strips with the highest local p_T was assumed to be the one which satisfied the trigger. In addition, each octant was subdivided into units of eight radial strips. A position, corresponding to the group of eight strips with the highest p_T content, was assigned to the triggering p_T in order to establish the radial dependence of the

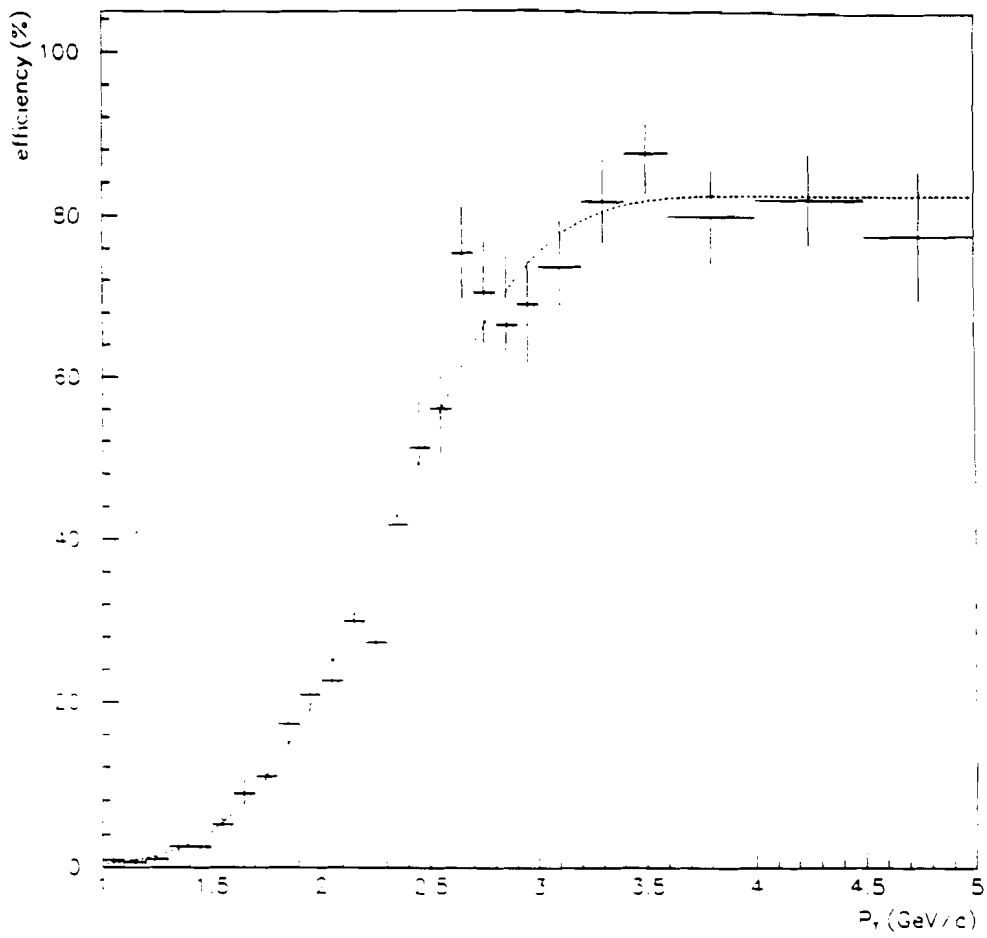

Figure 5.2: LAC outer region pretrigger efficiency.

SLOC trigger efficiency.

The ratio SLOC·TWOG/TWOG was initially measured for five octant regions. The first region includes strips 1 through 16, the second region strips 17 through 32, the third region covers strips 33 through 64, the fourth region, strips 65 through 96, and the last region includes strips 97 through 224. The segmentation of the each octant into these five regions was dictated by statistics* as well as known variations between groups of strips. Once the efficiency distributions for the five regions were

* Most of the events which satisfied the TWOG trigger were low p_T events, rendering the statistics for the higher SLOC trigger thresholds limited.

measured, additional combinations of the five regions were performed based on the similarities of the distributions.

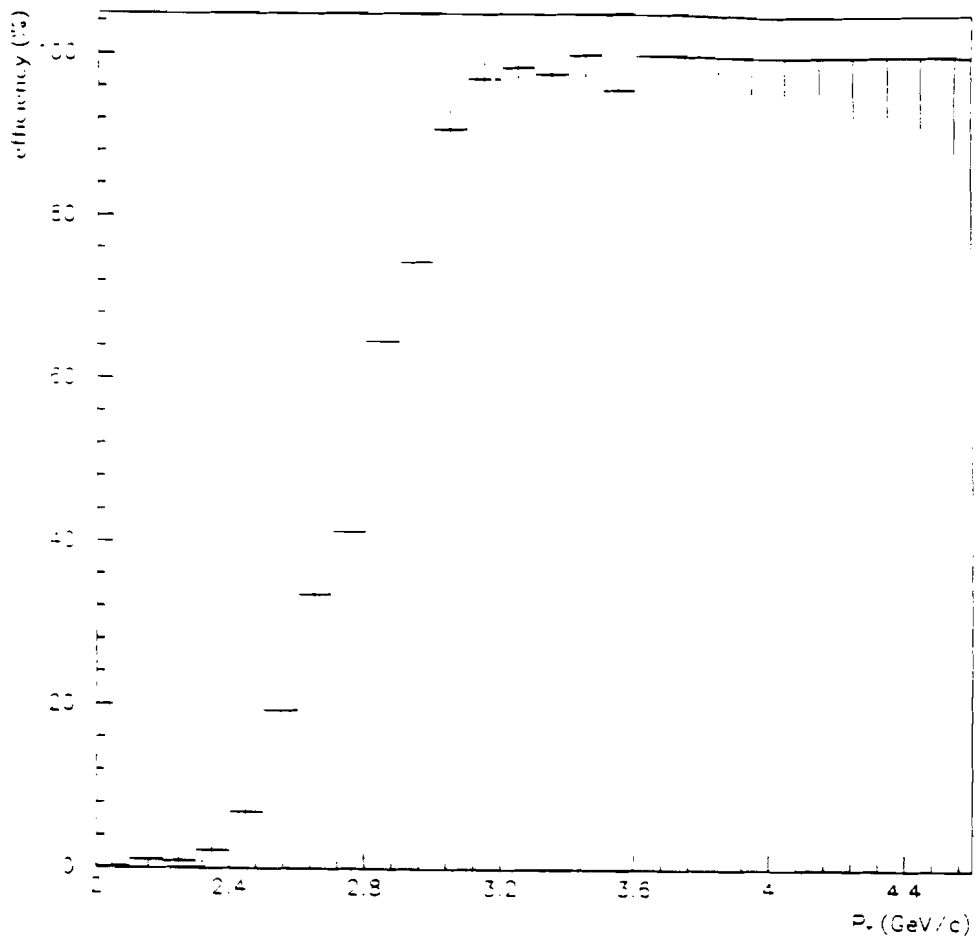

Figure 5.3: Octant 8 SLOC trigger efficiency for the lowest threshold setting.

Efficiencies were measured for each octant for each of the three thresholds used by the SLOC trigger. Figure 5.3 shows the efficiency distribution for octant 8 for the lowest threshold setting (see table 3.1). All the octant regions have been combined in this plot. The efficiency distributions obtained for all the octant regions were fit to the form given in equation (5.1). The results of the fits for each threshold are

given in tables 5.2-5.4. Two octants, 1 and 7, were not implemented in the SLOC trigger for a good portion of the experimental run due to hardware problems. In all cases the value of N is 1., and τ and σ are in GeV/c.

	Region 1		Region 2		Region 3		Region 4		Region 5	
Octant	τ	σ	τ	σ	τ	σ	τ	σ	τ	σ
1	-	-	-	-	-	-	-	-	-	-
2	3.92	0.15	3.92	0.15	4.29	0.42	4.29	0.42	4.29	0.42
3	4.31	0.30	4.31	0.30	4.13	0.22	4.13	0.22	4.31	0.30
4	4.35	0.29	4.11	0.22	4.11	0.22	4.35	0.29	4.35	0.29
5	4.78	0.15	4.78	0.15	4.78	0.15	4.14	0.41	4.14	0.41
6	4.44	0.20	4.44	0.20	4.16	0.26	3.96	0.40	3.96	0.40
7	-	-	-	-	-	-	-	-	-	-
8	4.14	0.19	4.14	0.19	3.85	0.20	3.85	0.20	3.85	0.20

Table 5.2: SLOC Trigger Efficiency Parameters, Threshold = 4.2 GeV/c

5.3 Veto Wall

As mentioned in chapter 2, the Veto Wall (VW) was used in the trigger event selection to veto events in which bremsstrahlung photons, produced by high energy muons traveling parallel to the beam, created fake high p_T signals. To veto the event, the signals from all counters in each VW plane were OR'ed, and the OR from both planes were put in coincidence (see equation 3.5). If the signals from both planes were in coincidence, a 150 ns-wide pulse reflecting this condition was set in anticoincidence with the interaction signal at the pretrigger level.

	Region 1		Region 2		Region 3		Region 4		Region 5	
Octant	τ	σ	τ	σ	τ	σ	τ	σ	τ	σ
1	-	-	-	-	-	-	-	-	-	-
2	3.36	0.15	3.21	0.19	3.52	0.32	3.52	0.32	3.52	0.32
3	3.65	0.31	3.65	0.31	3.42	0.26	3.42	0.26	3.65	0.31
4	3.68	0.32	3.56	0.25	3.56	0.25	3.68	0.32	3.68	0.32
5	4.04	0.20	4.04	0.20	4.04	0.20	3.64	0.41	3.64	0.41
6	3.80	0.25	3.80	0.25	3.58	0.23	3.37	0.32	3.37	0.32
7	-	-	-	-	-	-	-	-	-	-
8	3.57	0.24	3.57	0.24	3.32	0.25	3.33	0.37	3.33	0.37

Table 5.3: SLOC Trigger Efficiency Parameters, Threshold = 3.6 GeV/c

	Region 1		Region 2		Region 3		Region 4		Region 5	
Octant	τ	σ	τ	σ	τ	σ	τ	σ	τ	σ
1	3.04	0.22	3.16	0.14	2.96	0.25	2.96	0.25	2.96	0.25
2	2.65	0.18	2.58	0.21	2.90	0.30	2.90	0.30	2.90	0.30
3	2.98	0.23	2.98	0.23	2.82	0.27	2.82	0.27	2.98	0.23
4	3.05	0.28	2.92	0.20	2.92	0.20	3.05	0.28	3.05	0.28
5	3.44	0.20	3.44	0.20	3.44	0.20	2.88	0.30	2.88	0.30
6	3.17	0.21	3.17	0.21	3.00	0.25	2.80	0.30	2.80	0.30
7	3.03	0.28	3.03	0.28	3.03	0.28	3.34	0.31	3.34	0.31
8	2.70	0.27	2.96	0.17	2.70	0.27	2.70	0.27	2.70	0.27

Table 5.4: SLOC Trigger Efficiency Parameters, Threshold = 3.0 GeV/c

Using the information stored by the Minnesota latches, and applying a software simulation of the VW requirement in the offline analysis, no events were found where

a coincidence existed between the two VW planes within a period from ~ 20 ns before to ~ 110 ns after the interaction. Further studies showed that the trigger was sensitive to muons occurring earlier than 20 ns, and which were not vetoed by the VW signal. In addition, as described in chapter 3, there were gaps between counters in each of the VW planes. In cases where the muon went through one of such gaps a coincidence did not exist, and the event was not vetoed by the trigger.

The muon bremsstrahlung photons present a major source of background to the direct photon signal. To measure the muon contamination in our data sample, studies were carried out using the photon information from EMREC. The data stored in the Minnesota latches provided a 300 ns-wide window centered around the interaction time. A logical software VWS was used as the vetoing condition in the offline analysis. To generate this condition, all time ticks in the available window were used, and the counters from both veto wall planes in the quadrants geometrically corresponding to the triggering EMLAC quadrant were OR'ed. If during the 300 ns window any of the counters in either veto wall quadrant had registered a hit in the Minnesota latches, VWS was set to 1. Otherwise it was set to 0.

Two of the photon parameters reconstructed, directionality and photon arrival time, have proved to be useful in the muon studies. Directionality (δ_R) is a measurement of the photon trajectory inside the EMLAC. δ_R is determined from the energy deposition in the front and back sections of the electromagnetic calorimeter and is defined as

$$\delta_R = R_f - \frac{Z_{front}}{Z_{back}} R_b \tag{5.3}$$

where R_f and R_b are the reconstructed front and back radial positions of the energy

centroids. Z_{front} and Z_{back} are the longitudinal positions, relative to the target, of the front layers of the front and back sections of the EMLAC, with values of 900 cm and 918.5 cm respectively. The second term in equation (5.3) is the projection of the back radial position to the front section. Because of the focusing of the radial strips in the EMLAC, particles traveling parallel to the beam will have a larger δ_R than those originated at the target, since for parallel trajectories $R_f \approx R_b$. Figure 5.4 illustrates this concept.

A correlation between directionality and VW hits can be observed in the scatter plots shown in figures 5.5 and 5.6, where directionality has been plotted as a function of p_T for the highest p_T photon in the triggering quadrant. Figure 5.5 corresponds to the cases in which any of the counters of the VW quadrant, geometrically corresponding to the triggering quadrant, had a hit during the 300 ns window. This plot shows that the photons tend to have large directionalities while, as shown in figure 5.6, the directionality is primarily centered on zero in those events in which no VW hit was registered. From these two plots it can be seen that a good fraction of the high p_T photons have trajectories parallel to the beam.

The photon arrival time calculated based on the TVC information, was used to study the "out-of-time" events, and their correlation with muons (a complete description of the calculation of the photon time of arrival can be found in the PhD dissertation by Eric J. Prebys of the University of Rochester[29]). Figure 5.7 shows the arrival time distribution of the highest p_T photon in the triggering quadrant. In figure 5.7(a), it was required that no VW hits had been registered during the 300 ns window (VWS=0), while 5.7(b) shows the time distribution for those events in which a VW hit was observed (VWS=1). Notice the large peak present in figure

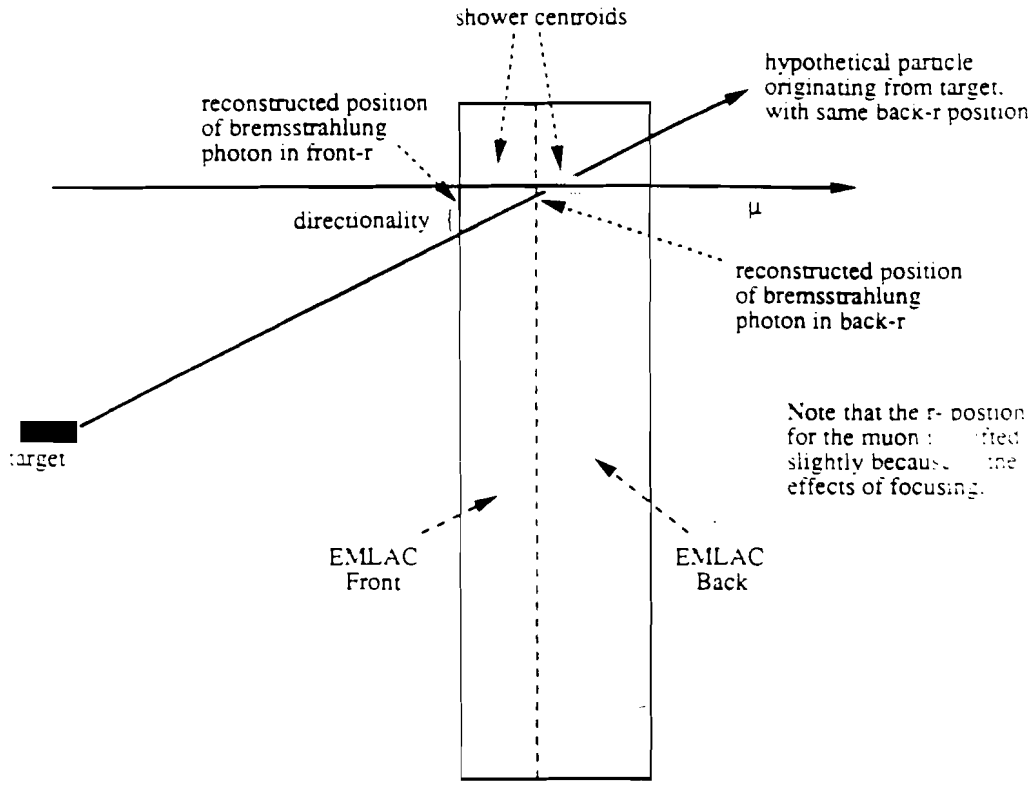

Figure 5.4: Concept of photon directionality. A particle traveling parallel to the beam, such as a muon-bremsstrahlung photon, will have a larger directionality than a photon originating at the target.

5.7(b) for times earlier than 25 ns, and its absence in figure 5.7(a). One can infer from this observation that early muons were responsible for a good number of the triggers. The distribution observed at positive arrival times, can be related to inefficiencies resulting from requiring a coincidence between the two VW planes to veto the event at the pretrigger level.

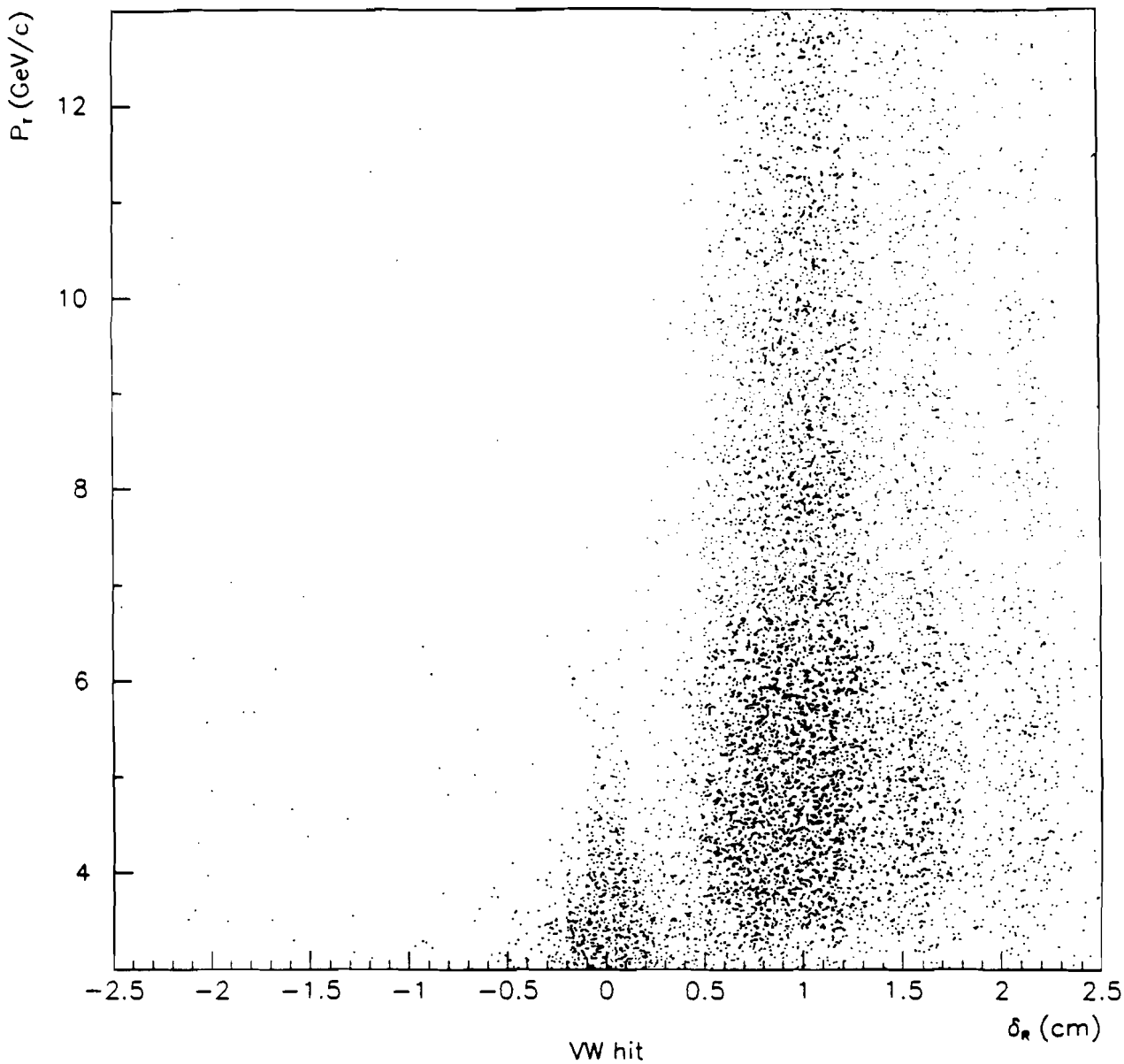

Figure 5.5: Photon P_T distribution vs directionality for events in which the veto wall quadrant, geometrically corresponding to the triggering quadrant, had a signal. A substantial number of photons, including the majority of the high p_T photons, have large directionalities, indication of objects not originated in the target.

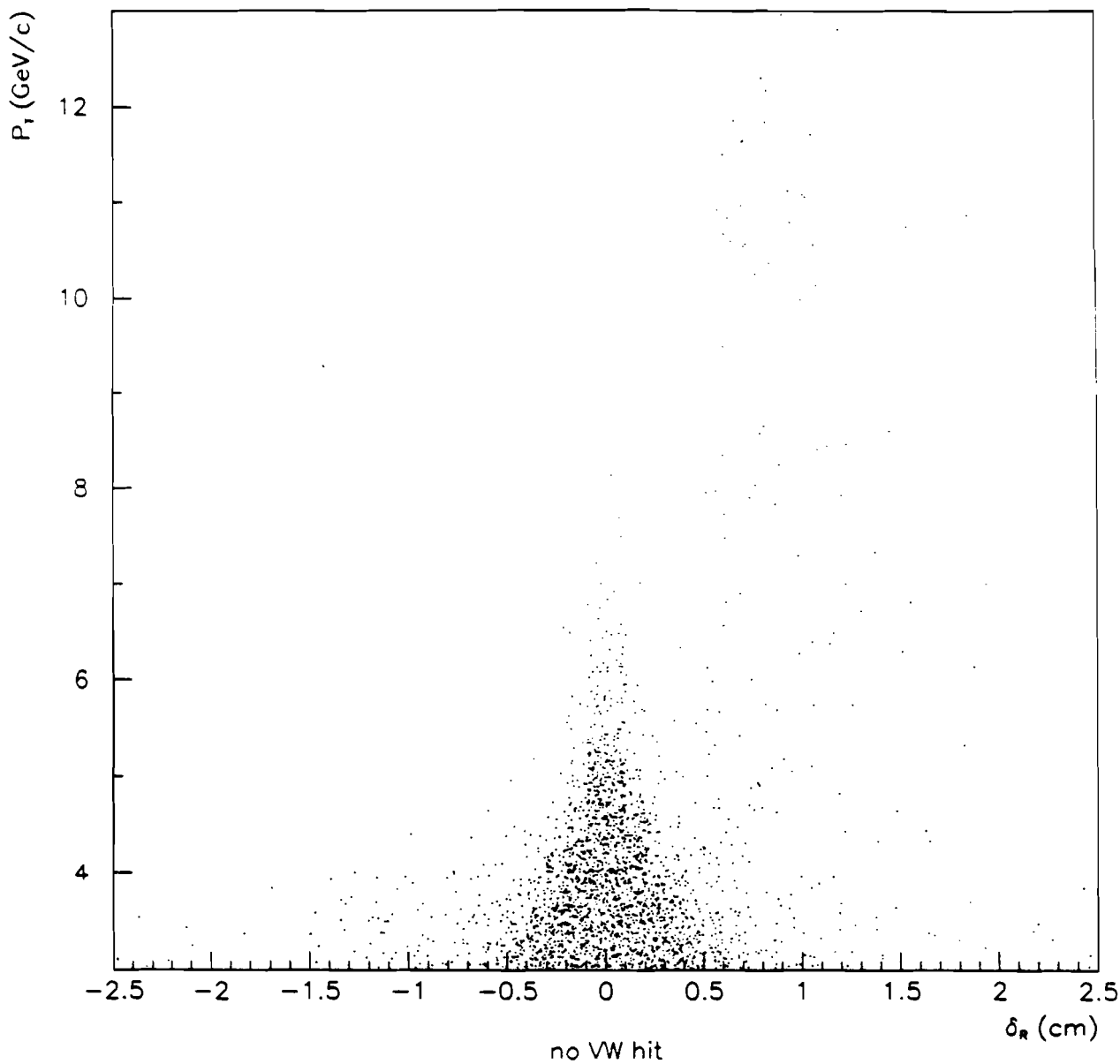

Figure 5.6: Photon P_T distribution vs directionality for events in which the veto wall quadrant corresponding to the triggering quadrant did not have a signal. The band of large directionality photons observed in figure 5.5 is not present here.

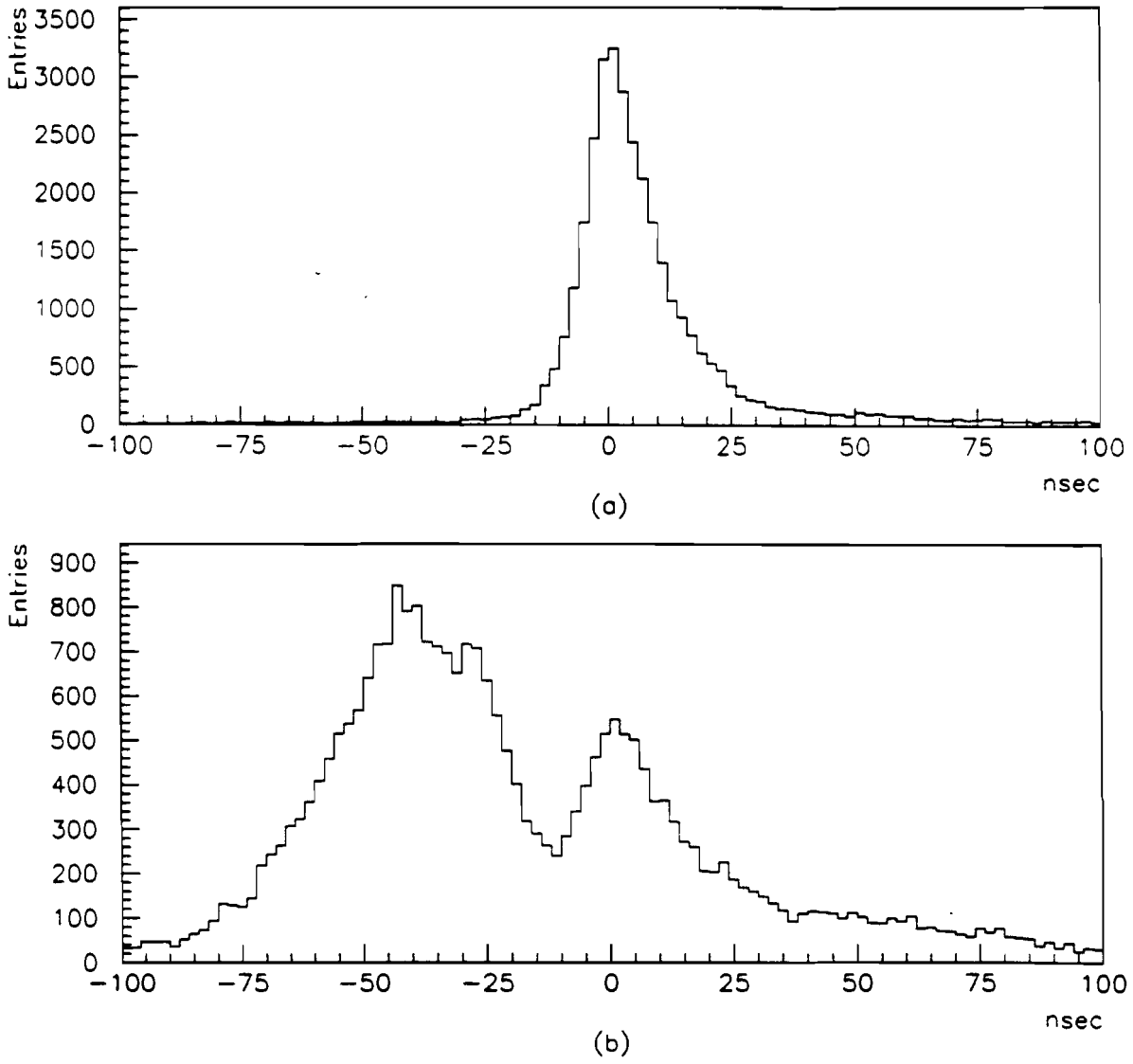

Figure 5.7: Photon arrival time distribution. (a) events in which the veto wall did not have a signal in the quadrant corresponding to the triggering EMLAC quadrant, and (b) events in which the veto wall had a signal in the quadrant corresponding to the triggering quadrant.

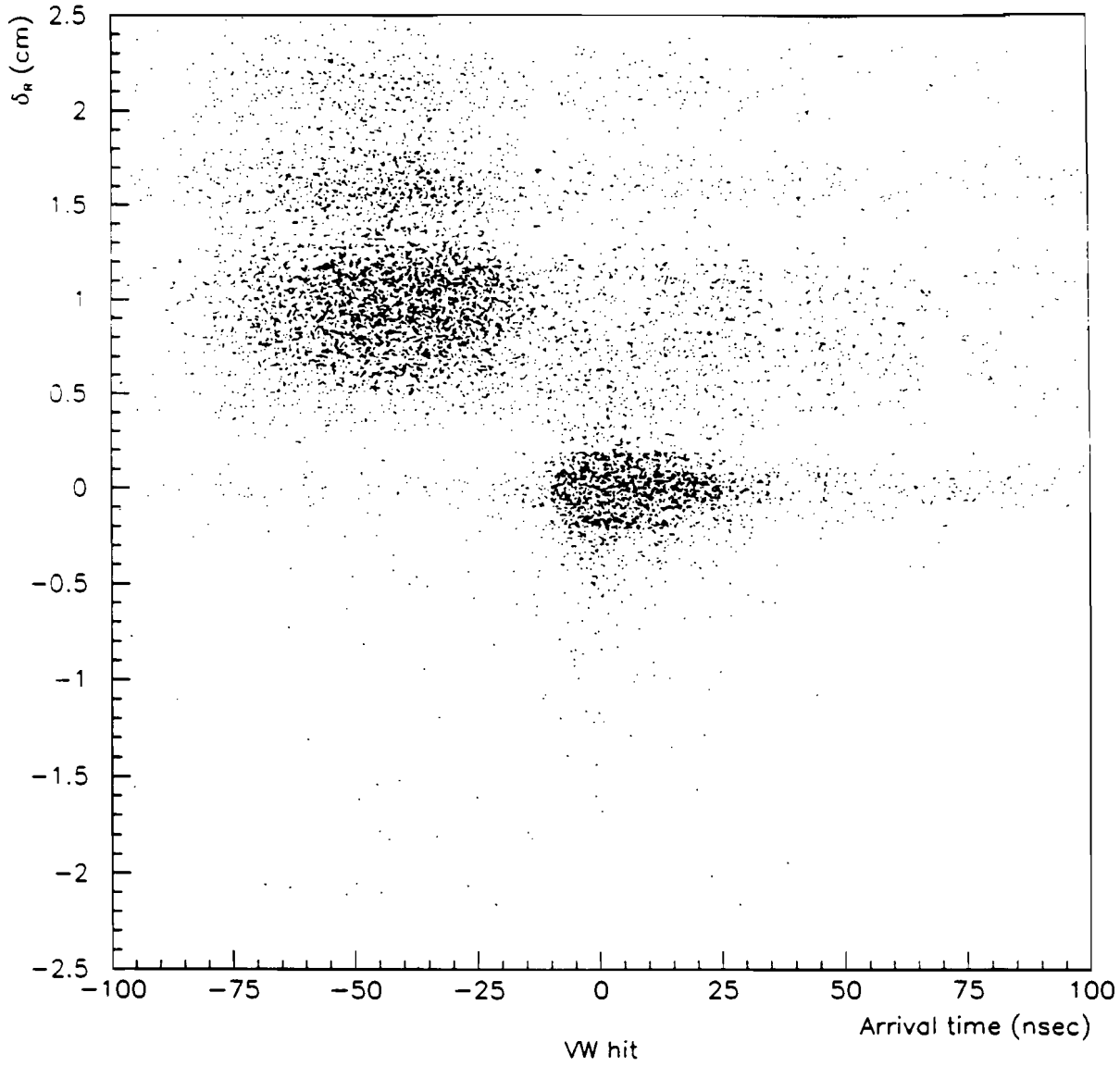

Figure 5.8: Photon arrival time vs directionality for events in which the veto wall had a signal in the quadrant corresponding to the triggering EMLAC quadrant.

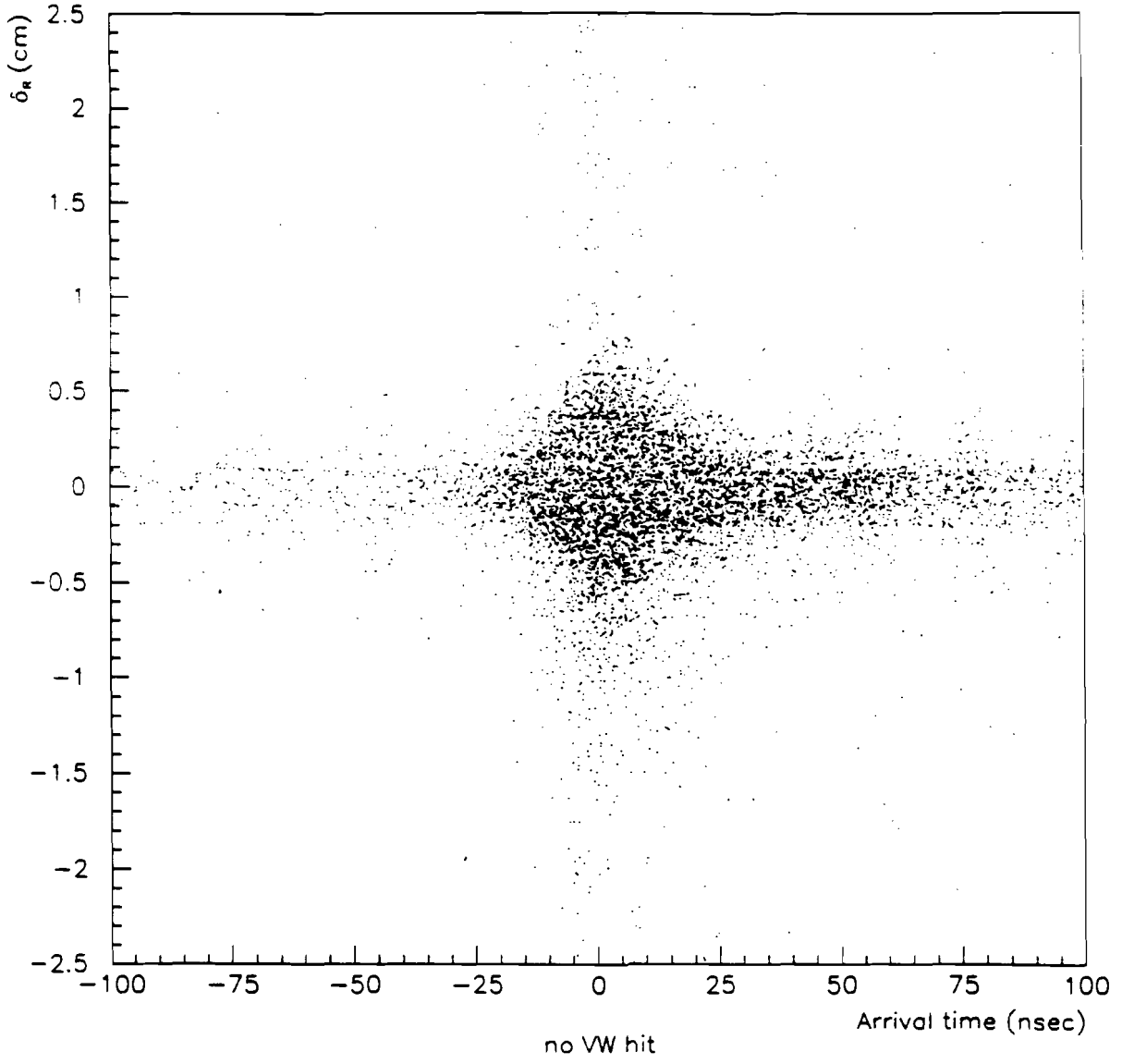

Figure 5.9: Photon arrival time vs directionality for events in which no signals were observed in the veto wall quadrant corresponding to the triggering EMLAC quadrant.

The correlation between photon arrival time and directionality can be seen in the scatter plots in figures 5.8 and 5.9. These figures show that in those events in which there was a VW hit, a large fraction of the photons have large directionalities and are also out of time, consistent with the assumption that they are bremsstrahlung photons produced by muons traveling parallel to the beam.

In conclusion, it appears that the VW information presents a good tool in the reduction of the muon background to the direct photon signal, by applying a software VW cut to eliminate muon-induced events.

6. DATA ANALYSIS

About 800 6250-bpi magnetic tapes of data were written during the 1987-1988 experimental run, approximately 500 of which were processed in the ACP system using MAGIC. During the first pass of processing, all variables thought to be useful for understanding the operation of the software and hardware were written to tape. During the second pass the data set size was compressed by removing all but essential physics quantities. The data taken during the experimental run was divided into sets, depending on conditions such as beam polarity, changes in the target, or special conditions in the spectrometer. Table 5.1 summarizes the data sample available for this analysis. This table shows the total number of events written to tape for each set, along with the beam polarity and the target type.

Set	Beam Polarity	Target	Triggers	Run Number
A	Negative	Cu + Be	786K	2852-3036
B	Positive	Cu + Be	440K	2588-2670
C	Positive	Cu + Be	1,225K	2387-2586
D	Negative	Be	1,247K	2062-2382
E	Positive	Be	1,508K	1728-2007
F	Positive	C	161K	1672-1719

Table 6.1: Breakdown of the E706 data sample.

The secondary tapes were subsequently split into separate data streams, according to hardware and software trigger type selections. The data used in this analysis includes only those events selected by LAC triggers. These events were split into three streams, according to the highest p_T measured for the event for single photons and for all photon pairs. All events in which the highest p_T found was less than 3 GeV/c were rejected. The three output streams, labeled "PT3", "PT4", and "PT5", were assigned to events in which the highest p_T was at least 3 GeV/c, 4 GeV/c, and 5 GeV/c respectively.

The data sample was further reduced after rejecting runs for different reasons. All runs from set B were excluded because of problems in the tracking system. Only runs in which the single local trigger (SLOC) was implemented were used.* This particular selection excluded all of set F and part of set E. Also, according to the SLOC trigger thresholds used at different times, only data from the PT3 stream was used for set A, and from the PT4 stream for sets C, D, and E.

Other considerations, based on a detailed study performed to eliminate unreliable data, were used in the event selection. About 5% of the data was rejected based on results from this study, such as runs in which the trigger behavior was unusual, or the behavior of some detector was unreasonable. In some instances, one or more of the EMLAC octants was not functioning properly. Runs were not rejected in these cases, but only data from the functioning parts was considered and the proper corrections applied.

---

* Using only events in which the SLOC trigger was satisfied was necessary due to the hardware problems found in the LGHI and LGLO triggers (see chapter 5), in addition to not having a clear understanding of their performance.

6.1 Event Selection

Once the runs to be analyzed had been selected, three cuts were imposed on the events to insure the quality of the data. One of the main concerns was to eliminate muon-triggered events, thus minimizing the background from muon bremsstrahlung photons to the direct photon signal. As described in the previous chapter, the veto wall information proved to be a good tool for this purpose. Every event was examined to determine if any of the counters of the veto wall quadrant geometrically corresponding to the triggering EMLAC quadrant, had a signal within the 300 ns time window centered around the time of the interaction. If that was the case, the event was rejected.

From the events not rejected by the veto wall cut, only those in which the vertex was found in the target region were kept. This requirement was imposed to ensure that the interaction had effectively occurred between the incoming beam particle and the beryllium or copper targets. Finally, if any of the EMLAC quadrants had an anomalously large amount of energy in one view which did not correlate with energy from another view in the formation of a photon, the event was rejected. The presence of a large amount of uncorrelated energy was an indication of a failure in the reconstruction process. The maximum amount of uncorrelated energy allowed for the event was 10 GeV.

Table 6.2 summarizes the effects of the selection criteria applied to the data. Column 1 shows the number of events remaining after the run selection criteria were applied. Column 2 indicates the number of events from column 1 which remained after the veto wall cut was applied. In column 3, the number of events in column 2 which satisfied the vertex cut is indicated, and in column 4, the final number of

Set	Run Selection	Veto Wall	Vertex	Unc Energy
A ($P_T \geq 3\,GeV/c$)	305,869	183,462	143,133	134,879
C ($P_T \geq 4\,GeV/c$)	195,031	46,110	36,973	34,904
D ($P_T \geq 4\,GeV/c$)	157,827	56,311	45,631	42,600
E ($P_T \geq 4\,GeV/c$)	150,920	39,079	26,898	24,608
Total	809,647	324,962	252,635	236,991

Table 6.2: Summary of events remaining after applying the rejection cuts.

events accepted after the uncorrelated energy cut is shown. Studies were performed to estimate the necessary corrections to compensate for the loss of good events to the rejection cuts applied.

6.2 π° Signal Definition

In each event, photons were paired with the other photons and their four momentum vectors added.* Figure 6.1 shows the mass spectrum for $\gamma\gamma$ pairs with $p_T > 3.5\,GeV/c$. Peaks around the π° and η meson masses are clearly visible. At the early stages of the analysis, the position of the π° peak in the $M_{\gamma\gamma}$ distribution was calculated for each octant to establish the relative energy scale between octants. Based on the position of the peaks, an energy correction factor was determined for each octant to bring the π° mass into agreement with the accepted value of 135 MeV, thus establishing the absolute energy scale of the EMLAC. These energy corrections were applied in this data analysis.

* π°'s decay primarily to $\gamma\gamma$ pairs ($\sim$98.8%).

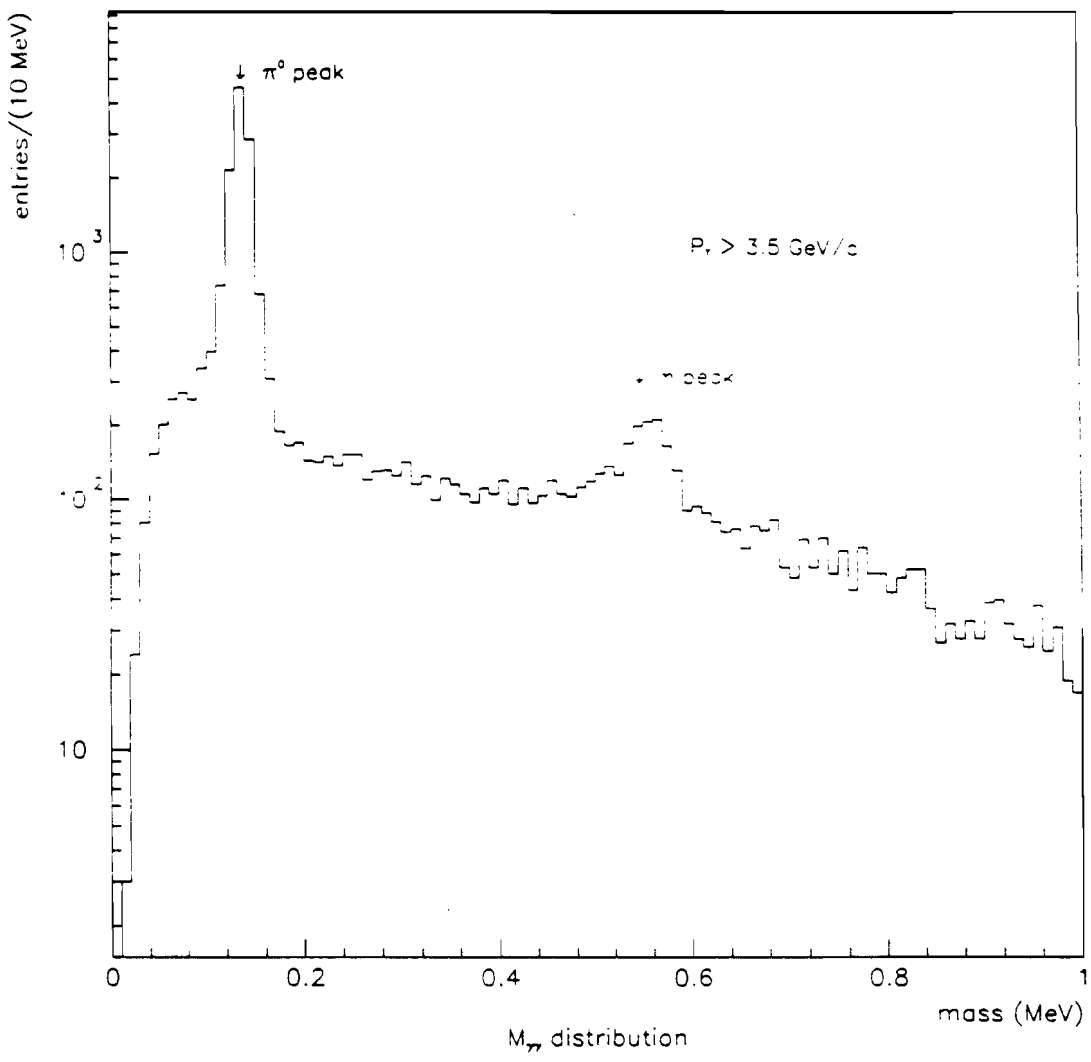

Figure 6.1: Mass distribution for $\gamma\gamma$ pairs with $P_T >$ 3.5 GeV/c. The π^0 and η mass peaks are clearly visible.

A π^0 candidate was defined as a $\gamma\gamma$ pair whose invariant mass was in the range $110\,\text{MeV} \leq M_{\gamma\gamma} \leq 160\,\text{MeV}$. Sidebands were defined to estimate the background to the π^0 signal. $\gamma\gamma$ pairs with a mass $M_{\gamma\gamma}$ between 75 and 100 MeV or between

170 and 195 MeV, were considered sideband pairs. To correct a distribution from background effects, the distribution of interest was obtained for $\gamma\gamma$ pairs in the π^0 mass region, and for $\gamma\gamma$ pairs in the sideband regions. The latter was then subtracted from the former to obtain the background corrected distribution.

The dependence of the π^0 mass (M_{π^0}) on the radial position is shown in figure 6.2. A dip is observed in this plot at ~ 40 cm. This dip is due to the improper reconstruction of the photon energy at the inner/outer Φ boundary. Photons near this boundary tend to deposit energy in both Φ views. When the fraction of energy deposited in one view is not large enough to be properly reconstructed and correlated, it will be lost and the photon energy reconstructed will be smaller than it would be otherwise. A correction for this effect was obtained by generating Monte Carlo photons near this boundary. The correction did not completely take care of the effect, and an additional correction to the π^0 mass was applied as a function of p_T and the distance to the inner/outer Φ boundary, for π^0s with radial positions between 35 and 45 cm. The distribution for radii larger than ~ 60 cm decreases gradually, and discontinuities are clear. This behavior is not clearly understood at this time, but appears to be related to the parametrization of the photon shower due to some additional radiation length that was not properly taken into account. The discontinuity at 80 cm is not fully understood yet, but appears to be related to the breaking of the radial view into inner and outer R sections for readout purposes, which occurs at this radius. The effects of these energy fluctuations on the measurement of the cross sections will be described in the following chapter.

Figure 6.3 shows the azimuthal dependence of the π^0 mass. Due to the presence of insensitive regions used by the structural support plates of the detector, energy

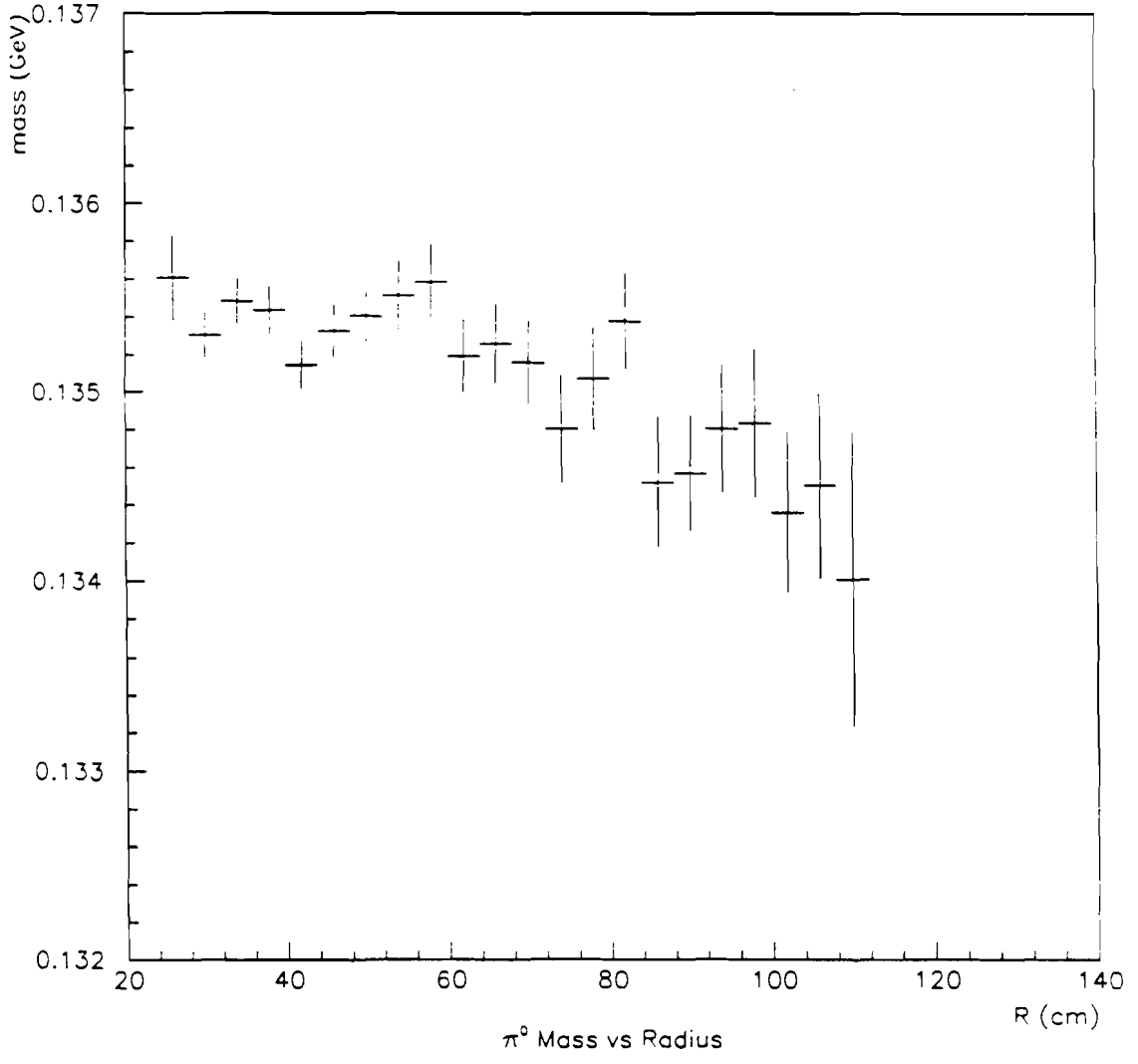

Figure 6.2: Radial position dependence of the reconstructed π° mass.

losses occurred at the quadrant boundaries and therefore a fiducial cut was imposed to remove photons reconstructed in those areas. The jump in the center of the distribution is due to the loss of photon energy in the octant boundary. Losses at the boundary between octants in a quadrant are due mainly to reconstruction effects:

when the shower energy is shared by two views, some of the energy in both views falls below threshold and is lost in the correlation procedure. The sharing of energy between octants also affected the LAC triggers since they were sensitive only to the deposition of energy in the individual octant. In the case of the SLOC trigger, when the decay photons from the π° fell in different octants the trigger was less efficient detecting the π° than when both photons fell in the same octant. Fiducial cuts were also imposed in the octant boundaries to help remove the effects. The overall fiducial cuts imposed in the selection process were as follows: photons for which the reconstructed radial position R_γ was not in the region $24\,\mathrm{cm} \leq R_\gamma \leq 138\,\mathrm{cm}$ or which were less than three centimeters away from the quadrant radial boundary were not used. In addition, only $\gamma\gamma$ pairs made up by photons which fell in the same octant, and at least 3 cm away from the octant boundary, were considered π° candidates.

As mentioned in chapter one, due to biases introduced by the geometrical acceptance and the energy reconstruction efficiency, detectors are less efficient in the detection of π°s with large asymmetric decays. Figure 6.4(a) shows the asymmetry distribution for $\gamma\gamma$ pairs in the π° mass region. The same distribution is shown in figure 6.4(b) for $\gamma\gamma$ pairs in the sideband regions. The π° asymmetry distribution, with background subtracted, is shown in figure 6.5. This distribution is basically flat for asymmetry values of up to 0.75, at which point it falls rapidly. For this reason, only $\gamma\gamma$ pairs with an asymmetry of less than 0.75 were used in the definition of the π° signal.

Figure 6.6 shows the $M_{\gamma\gamma}$ distribution in the π° mass region, for $\gamma\gamma$ pairs with $p_T \geq 3\,\mathrm{GeV/c}$. The dotted line has the asymmetry cut applied. Notice how a good

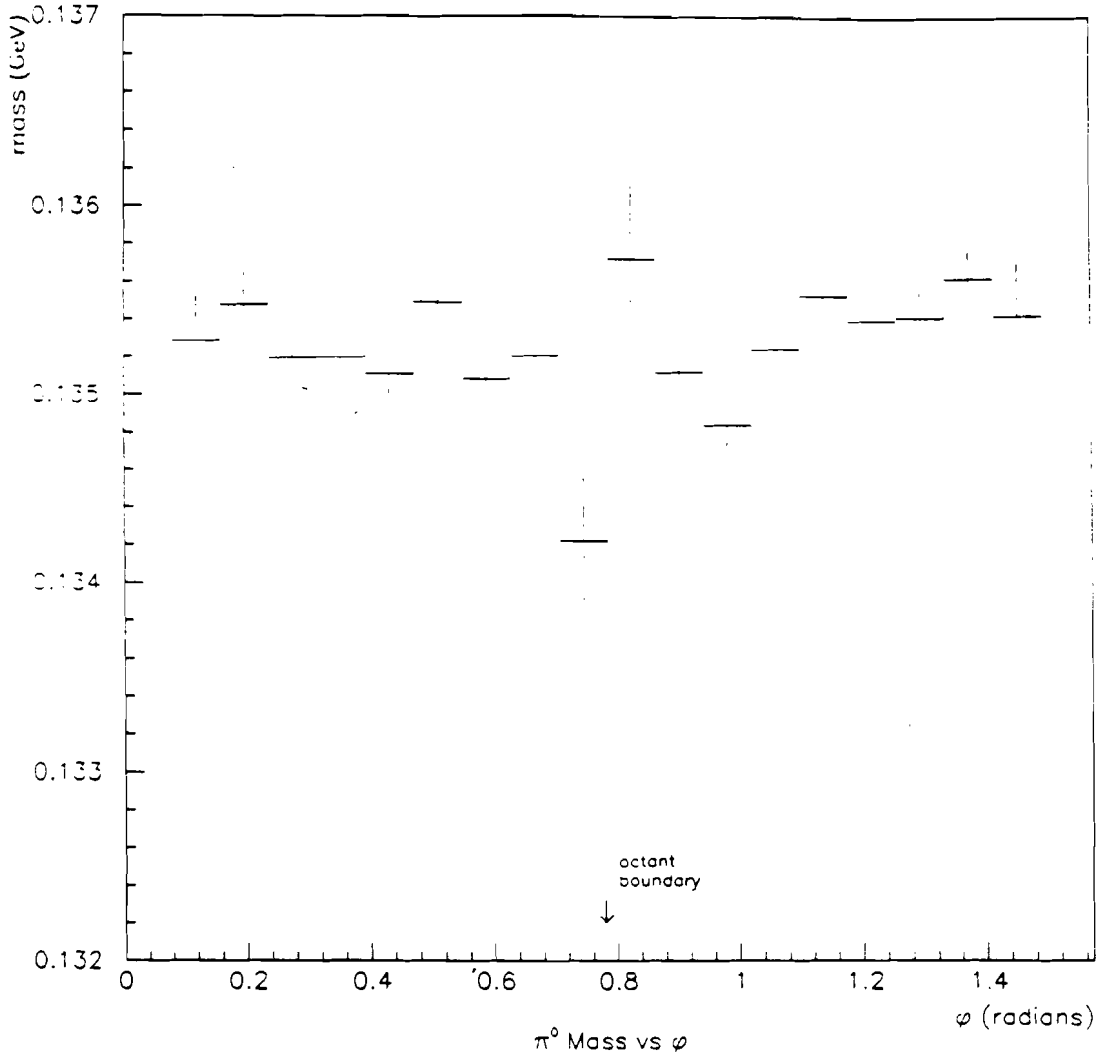

Figure 6.3: Azimuthal distribution of the reconstructed π^0 mass. The dips observed are due to energy losses at the quadrant and octant boundaries.

fraction of background goes away when the asymmetry requirement is applied.

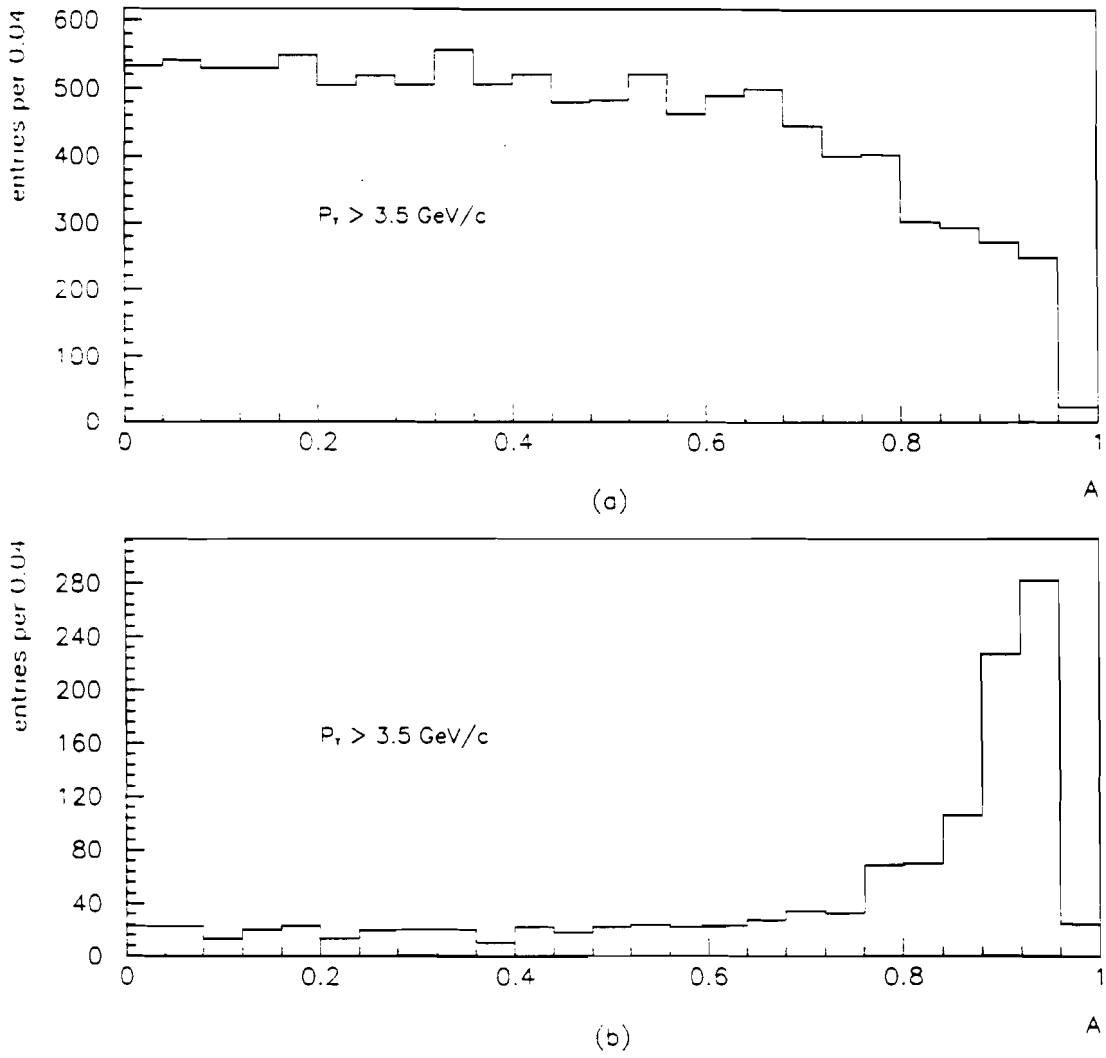

Figure 6.4: Asymmetry distribution for (a) $\gamma\gamma$ pairs in the π° mass peak region, and (b) $\gamma\gamma$ pairs in the sideband region. A p_T cut of 3.5 GeV/c was required in both cases.

6.3 Monte Carlo

The Monte Carlo software package developed for experiment E706, made use

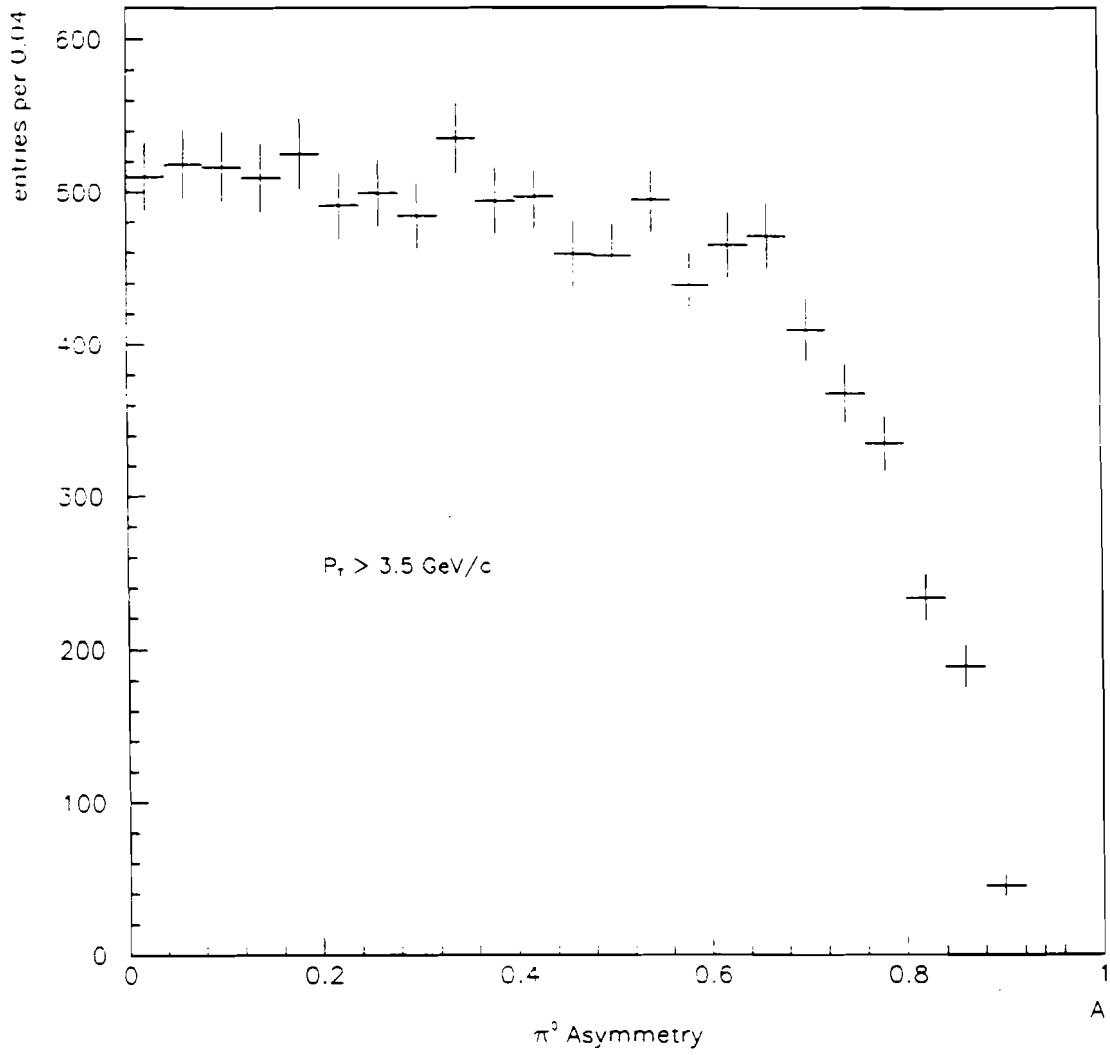

Figure 6.5: π^0 asymmetry distribution with background subtracted. A p_T cut of 3 GeV/c has been imposed.

of GEANT[30] and was formatted according to MAGIC. Embedded within it are other Monte Carlo programs for simulation of electromagnetic showers (EGS) and hadronic showers (GEISHA). The use of GEANT in the Monte Carlo allowed for a

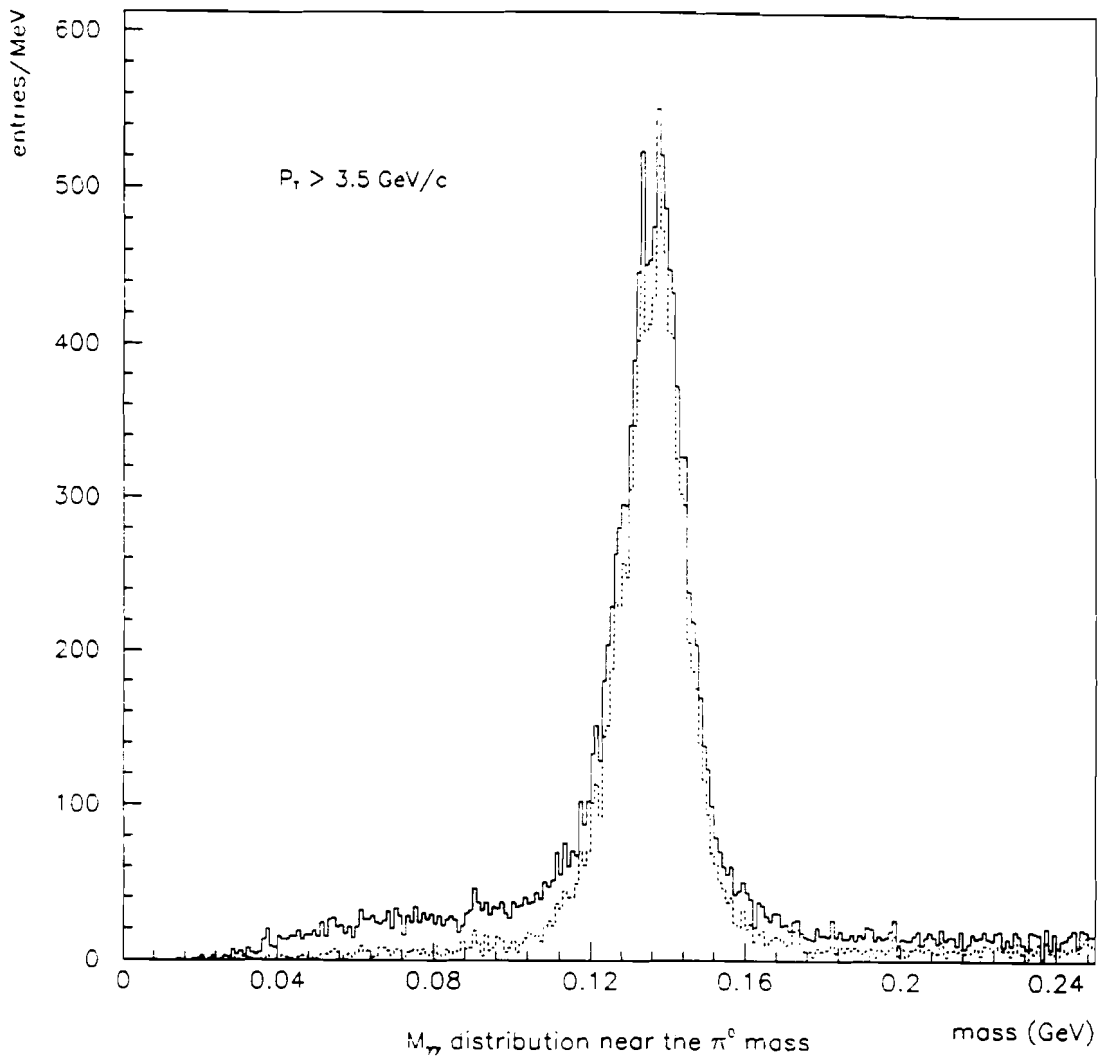

Figure 6.6: $M_{\gamma\gamma}$ distribution in the M_{π^0} region for $P_T \geq 3\,\mathrm{GeV/c}$. The dotted line includes only $\gamma\gamma$ pairs whose asymmetries are smaller than 0.75. Notice how a good fraction of the background is removed by the asymmetry requirement.

complete software simulation of the E706 spectrometer. Event topologies could be studied by two different methods. One was to allow each particle to interact through the spectrometer, treating the particles produced in this interactions in the same fashion. The second method was to make use of parametrizations to simulate the response of the different detectors, greatly reducing the amount of computer time

involved in the process. Parametrizations were obtained from full event simulation studies, and were used in studies which required high statistics.

6.4 π° Cross Section Calculation

The invariant cross section per nucleon, can be expressed as a function of transverse momentum (p_T) and rapidity (y) by the following recipe:

$$E\frac{d\sigma}{d^3p} = \frac{1}{N_t B_{in} 2\pi p_T}\frac{dN(p_T, y)}{dp_T dy} \tag{6.1}$$

where B_{in} is the number of incident beam particles, $dN/dp_T dy$ is the differential event distribution, and N_t is the number of target nucleons per unit area and is given by

$$N_t = \rho l N_A n_A / A \tag{6.2}$$

where ρ is the density of the target (in gm/cm^3), l is the thickness of the target (in cm), N_A is Avogadro's number, A is the atomic weight, and n_A is the number of nucleons. For the extraction of the cross section from the data sample, each π° event was weighed to correct for the efficiencies involved in the selection of the event, namely, trigger efficiency, geometric acceptance of the EMLAC, photon reconstruction efficiency, and vertex determination. The following paragraphs describe the determination of the different corrections, and the final calculation of the cross section distribution.

Trigger Efficiency Correction

To determine the correction related to the trigger efficiency, the reconstructed R-view energy of all photons in the π° octant was deposited back into the corresponding EMLAC strips. Following the procedure described in chapter 5, the

energy in the strips was used to measure the global p_T in each of the pretrigger regions, and the highest local p_T deposition in each of the 5 SLOC trigger radial regions. Characteristics of the trigger such as, for example, groups of strips which were known to be dead for triggering purposes during a number of runs, or octants which were not implemented in the trigger,* were taken into account in the calculation of the "triggering" p_T. If one (or both) of the photons in the $\gamma\gamma$ pair had fallen in one of the known dead regions, a trigger efficiency of zero was given for the event.

Using the functional form given in equation 5.1 and the parameters obtained from the fits described in chapter 5, the efficiencies corresponding to the global p_T in the two pretrigger regions were determined. The two efficiencies were combined to give the overall pretrigger efficiency

$$\varepsilon_{\text{pret}} = 1. - \left(1. - \varepsilon^{\text{in}}_{\text{pret}}\right) \times \left(1. - \varepsilon^{\text{out}}_{\text{pret}}\right) \tag{6.3}$$

where $\varepsilon^{\text{in}}_{\text{pret}}$ and $\varepsilon^{\text{out}}_{\text{pret}}$ are the efficiencies in the inner and outer pretrigger regions respectively.

The calculation of the SLOC trigger efficiency was performed in a similar fashion. In this case, the trigger efficiency was determined for each of the 5 SLOC trigger regions, according to the highest local p_T deposition measured for each region, and the largest of the 5 efficiencies was used as the SLOC trigger efficiency $\varepsilon_{\text{SLOC}}$. The total trigger efficiency was then the product of the pretrigger and the SLOC trigger

* As mentioned in chapter 5, octants 1 and 7 were not in the SLOC trigger for a good portion of the experimental run due to hardware problems. Data from these octants were considered only for those runs in which the lowest SLOC trigger threshold was used.

efficiencies, i.e.,

$$\varepsilon_{trg} = \varepsilon_{pret} \times \varepsilon_{SLOC} \tag{6.4}$$

Based on the results from the efficiency measurements for the SLOC trigger, and the parameters obtained from the fits, a minimum p_T threshold was assigned to every SLOC trigger region in each octant, below which the trigger was not considered reliable to give an appropriate trigger weight. Because the thresholds in the different regions and octants were not the same, contributions to the p_T ranges near threshold varied from region to region. To compensate for these differences and for the presence of "dead" regions and the absence of octants in the trigger system, a weight w_{oct} was applied to each event. This weight was defined by

$$w_{oct} = \frac{8}{N_{live}(r, p_T)} \tag{6.5}$$

where $N_{live}(r, p_T)$ was the number of octants in which neither photon would have fallen in a "dead" area, and whose allowed threshold in the region corresponding to r was below the given p_T value.

EMLAC Acceptance and Photon Reconstruction Efficiency Corrections

To calculate the geometrical acceptance, π^oMonte Carlo events were generated in a grid of p_T and rapidity points, one thousand events per point. The grid consisted of P_T values from 3.0 to 10.0 GeV/c, in intervals of 0.5 GeV/c, and rapidity (y) values from -0.8 to 0.8 in 0.2 intervals. The π^os were generated at random azimuthal angles, and were allowed to decay isotropically to two photons. The geometrical acceptance for each point in the p_T–y grid, was calculated by finding the fraction of the number of generated π^os whose two photons fell within the fiducial

region of a single octant. Only π°s with asymmetry less than 0.75 were used in the acceptance calculation. Table 6.3 lists the acceptance measured for each of the points in the grid. The acceptance correction for the event ($\varepsilon_{acc}(y, p_T)$), at given y and p_T values, was determined by a two-dimensional interpolation of the values in this table.

$P_T \downarrow \backslash\ y \rightarrow$	-0.8	-0.6	-0.4	-0.2	0.0	0.2	0.4	0.6	0.8
3.0	0.81	.78	0.77	0.75	0.73	0.72	0.68	0.63	0.60
3.5	0.81	0.80	0.79	0.77	0.75	0.72	0.69	0.65	0.62
4.0	0.82	0.81	0.81	0.78	0.76	0.73	0.69	0.65	0.64
4.5	0.83	0.82	0.80	0.79	0.77	0.74	0.70	0.67	0.64
5.0	0.83	0.82	0.81	0.79	0.77	0.75	0.72	0.67	0.64
5.5	0.84	0.83	0.81	0.79	0.78	0.75	0.72	0.68	0.65
6.0	0.84	0.83	0.81	0.78	0.78	0.75	0.72	0.68	0.65
6.5	0.85	0.83	0.82	0.80	0.78	0.75	0.72	0.69	0.65
7.0	0.84	0.83	0.82	0.81	0.80	0.76	0.72	0.69	0.66
7.5	0.85	0.84	0.83	0.80	0.78	0.77	0.73	0.68	0.66
8.0	0.86	0.85	0.83	0.81	0.79	0.76	0.73	0.69	0.67
8.5	0.86	0.84	0.83	0.81	0.79	0.76	0.73	0.69	0.67
9.0	0.86	0.85	0.83	0.81	0.79	0.76	0.74	0.70	0.67
9.5	0.86	0.85	0.84	0.81	0.80	0.77	0.74	0.70	0.67
10.0	0.86	0.84	0.83	0.82	0.80	0.77	0.73	0.70	0.68

Table 6.3: EMLAC geometric acceptance for π°s as a function of p_T and rapidity.

The reconstruction efficiency calculation was performed using Monte Carlo (MC) generated π° events. It was found that in our energy ranges, the recon-

struction efficiency for π°s is basically independent of p_T and rapidity, depending only on the photon multiplicity in the octant.[31] Table 6.4 lists the numbers used in the calculation of the reconstruction efficiency (ε_{rec}) for each event. The errors quoted in this table are poissonian.

Photon Multiplicity	Reconstruction Efficiency	Fraction of MC Events (%)
< 2	0.0	1.05
2	0.965 ± 0.004	71.84
3	0.929 ± 0.010	20.14
≥ 4	0.848 ± 0.023	6.97

Table 6.4: EMLAC reconstruction efficiency for π°s as a function of photon multiplicity.

Vertex Determination and Photon Conversions

A correction related to the efficiency of the vertex finding algorithm, was applied in each event. This correction was of the form[32]

$$w_{vtx} = 1.0019 - 0.0079 \times V_z \tag{6.6}$$

where V_z is the reconstructed position of the vertex along the beam line.

A correction ε_{conv} was applied to take into account the losses of π°s due to photon conversions in the target. ε_{conv} was a function of the vertex position V_z, and corresponded to the probability that neither of the decay photons converted in the target region.

Beam Count †

The Live Triggerable Beam (LTB), or number of incident beam particles which could have had a "clean" interaction in the target when the trigger system was able to perform the event selection, was determined from the information stored in the trigger scalers. LTB was given by

$$\mathrm{LTB}(\mathrm{p_T}) = \mathrm{LB} \times \eta_{el} \times \eta_{lt} \tag{6.7}$$

with the three quantities in the product defined as follows:

- LB: is the number of beam particles which went through the hole in the BH counter when all the computers were ready for the event selection,*
- η_{el}: is the fraction of interactions not rejected by the EARLY/LATE filter. It is calculated as the ratio of interactions for which both CLEAN_EARLY and CLEAN_LATE signals were generated, to the total number of interactions (INT) defined, during the time the COMP_RDY gate was enabled.
- η_{lt}: this number measures the fraction of time during which the trigger would have been able to select an event. This trigger live time is given by

$$\eta_{lt} = \mathrm{LT} \times (1 - \mathrm{V_{dt}}) \tag{6.8}$$

where LT is the total number of PRETRIG and NOPRET signals generated, divided by the total number of LINT1's, and corresponds to the fraction of

† Some of the terminology used here relates to chapter 3, in which a description of the trigger event selection has been presented.

* Recall that only those interactions correlated to beam particles that satisfied this requirement were used in the event selection.

time the trigger was not busy processing an interaction. V_{dt} is the trigger dead time due to the presence of any of the vetoing signals in the pretrigger. Since the EARLYPT veto was applied in an octant by octant basis, V_{dt} was calculated for each octant separately.

The p_T dependence of LTB, is related to the fact that p_T cuts were imposed according to the measured SLOC trigger threshold. Accordingly, for a given p_T region, the value of LTB was integrated only over runs in which that p_T was above the minimum allowed value.

The beam count $B_i(p_T)$ used for the determination of the cross section was defined as

$$B_i(p_T) = LTB \times \eta_{abs} \times B_f \tag{6.9}$$

where η_{abs} is the probability that a beam particle was not absorbed between the beam counters and the target of interest. As mentioned in chapter 2, the helium pressure in the Cherenkov detector was set to tag minority particles (K^-/π^+) in the negative/positive beam. For the reactions of interest in this analysis, events in which a beam particle had been tagged as a minority particle were rejected, provided the information from the Cherenkov logic was deemed reliable. B_f gives the fraction of beam particles which would not have been tagged as minority particles (see table 2.1). In those cases in which the Cherenkov information was not reliable, no events were rejected and B_f had a value of 1. The values of η_{abs} and B_f for the different reactions, are given in table 6.5 An additional small correction had to be applied to the beam count for some runs. This correction was required, because the scaler information for the last spill was not written to tape when the run ended in the middle of the spill.

Cross Section Distribution

A weighed π° count was calculated for selected p_T bands and rapidity regions. The weighed sum is defined as

$$N_w^{unc}(p_T, y) = \frac{1}{\Delta y \Delta p_T} \sum_{i=1}^{N_{\gamma\gamma}} \frac{w_i}{p_{Ti}} \tag{6.10}$$

where $N_{\gamma\gamma}$ is the number of $\gamma\gamma$ pairs which satisfied all the conditions to be π° candidates, whose p_T was within the band limits p_T^{lo} and p_T^{hi}, and with rapidity within the rapidity region boundaries. Δp_T and Δy are the widths of the p_T band and the rapidity region, and are approximations of dp_T and dy in equation(6.1).

$$\Delta p_T = p_T^{hi} - p_T^{lo} \tag{6.11}$$

$$\Delta y = y^{hi} - y^{lo} \tag{6.12}$$

w_i is the weight applied to the event, and is given by

$$w_i = \frac{w_{oct} w_{vtx}}{\varepsilon_{trg} \varepsilon_{acc} \varepsilon_{rec} \varepsilon_{conv}} \tag{6.13}$$

A weighed count ($N_w^{sb}(p_T, y)$) was obtained for $\gamma\gamma$ pairs whose mass fell within the sideband regions. N_w^{sb} was subtracted from N_w^{unc}, and an additional global correction was applied to the difference, to obtain the corrected π° sum, i.e.,

$$N_w^{corr}(p_T, y) = \frac{C}{2\pi} \left(N_w^{unc}(p_T, y) - N_w^{sb}(p_T, y) \right) \tag{6.14}$$

Parameter	$\pi^- + Be$	$\pi^- + Cu$	p + Be	p + Cu
η_{abs}				
(Be + Cu target)	0.949	0.986	0.934	0.981
(Be only target)	0.957	-	0.942	-
B_f	0.986	0.986	0.942	0.942
Double Occupancy	0.98	0,98	0.98	0.98
Photon Conversion	1.076	1.076	1.076	1.076
Asymmetry cut correction	1.33	1.33	1.33	1.33
Uncorrelated Energy correction	1.04	1.04	1.04	1.04
Veto Wall cut correction	1.11	1.11	1.10	1.10
Tail loss correction	1.04	1.04	1.04	1.04
C (total correction)	1.69	1.69	1.68	1.68
$N_t \times 10^{-24}$	4.445	0.869	4.445	0.869

Table 6.5: Process dependent parameters used in the evaluation of the cross sections.

The overall correction factor C is a combination of the following: (1) the correction for double occupancy, to take into account cases in which two beam particles arrived simultaneously, (2) the asymmetry correction for cutting $\gamma\gamma$ pairs with asymmetry larger than 0.75, (3) the correction for conversions of the decay photons downstream of the target, (4) the correction for the loss of good events to the

veto wall, vertex, and uncorrelated energy cuts described in section 6.1 and, (5) a correction for losses of π°s due to the mass cuts imposed in the π°definition. The values of these corrections and C are given in table 6.5.

Finally, the π° experimental cross section per nucleon corresponding to (6.1), is measured as

$$E\frac{d\sigma}{d^3p} = \frac{1}{N_t B_{in}(p_T)} N_w^{corr}(p_T, y) \tag{6.15}$$

Results from this data analysis are presented in the following chapter.

7. RESULTS

Distributions of the form in equation 6.16 have been obtained for the following processes:

$$\pi^- + \mathrm{Be} \rightarrow \pi^\circ + \mathrm{X} \tag{7.1}$$

$$\mathrm{p} + \mathrm{Be} \rightarrow \pi^\circ + \mathrm{X} \tag{7.2}$$

$$\pi^- + \mathrm{Cu} \rightarrow \pi^\circ + \mathrm{X} \tag{7.3}$$

$$\mathrm{p} + \mathrm{Cu} \rightarrow \pi^\circ + \mathrm{X} \tag{7.4}$$

The results of these measurements, and comparisons between them to examine nuclear and beam dependence, are presented in the following sections along with comparisons with QCD predictions.

7.1 Cross Section Measurements

The inclusive differential cross sections per nucleon for π° production in processes (7.1)–(7.4), have been measured over various rapidity and p_T intervals. For the two reactions in which the interaction occurred in the beryllium target ((7.1) and (7.2)), the cross sections were measured over seven rapidity intervals, in sections of 0.2 units, to cover the range $-0.7 < y < 0.7$. For the other two cases, due to statistical limitations, the same rapidity range was divided into only three

Interval	P_T^{lo} (GeV/c)	P_T^{hi} (GeV/c)
ΔP_1	3.25	3.5
ΔP_2	3.5	3.75
ΔP_3	3.75	4.0
ΔP_4	4.0	4.25
ΔP_5	4.25	4.5
ΔP_6	4.5	4.75
ΔP_7	4.75	5.0
ΔP_8	5.0	5.5
ΔP_9	5.5	6.0
ΔP_{10}	6.0	7.0
ΔP_{11}	7.0	8.0
ΔP_{12}	8.0	10.0

Table 7.1: P_T intervals used in the cross section measurement

regions. The three rapidity regions are: $-0.7 < y < -0.2$, $-0.2 < y < 0.2$, and $0.2 < y < 0.7$.

The binning on p_T was done according to table 7.1, and the p_T ranges covered were defined according to the process. For the $\pi^- + \mathrm{Be}$ case, measurements were performed for p_T values between 3.25 and 10 GeV/c, and for the $\pi^- + \mathrm{Cu}$ cross sections, the measurements were restricted to p_T values between 3.25 and 8 GeV/c. For the proton data the cross section measurements were performed for p_T values in the range $4 < p_T < 8$ GeV/c. The results obtained for the four processes in the different rapidity and p_T bins are given in tables 7.2–7.5. The average p_T value for each p_T interval is indicated in the second column in each table. The errors quoted

P_T range	$< P_T >$	$-0.7 < y < -0.5$	$-0.5 < y < -0.3$	$-0.3 < y < -0.1$
ΔP_1	3.36	14926.4 ± 1822.7	30693.1 ± 2834.9	41102.9 ± 3036.1
ΔP_2	3.61	9145.9 ± 1168.9	17147.8 ± 1839.7	21198.1 ± 1853.1
ΔP_3	3.86	5675.3 ± 727.8	8929.3 ± 1014.1	9613.9 ± 1020.1
ΔP_4	4.11	2245.5 ± 232.9	3929.7 ± 461.9	4554.8 ± 439.9
ΔP_5	4.36	1716.9 ± 187.6	1884.4 ± 242.6	2576.3 ± 212.8
ΔP_6	4.61	799.3 ± 144.7	1434.8 ± 192.4	1301.0 ± 203.7
ΔP_7	4.86	469.8 ± 82.1	603.3 ± 84.8	687.7 ± 101.3
ΔP_8	5.19	306.8 ± 55.7	347.4 ± 47.9	303.8 ± 34.7
ΔP_9	5.71	45.9 ± 12.7	106.3 ± 21.2	101.7 ± 18.9
ΔP_{10}	6.32	11.3 ± 4.2	12.88 ± 4.14	14.38 ± 4.49
ΔP_{11}	7.43	0.82 ± 0.82	1.66 ± 1.66	0.53 ± 1.68
ΔP_{12}	8.42	0.40 ± 0.40	-	-
	$-0.1 < y < 0.1$	$0.1 < y < 0.3$	$0.3 < y < 0.5$	$0.5 < y < 0.7$
ΔP_1	48801.9 ± 2652.6	51062.5 ± 2232.5	61587.3 ± 2646.6	53920.8 ± 2244.4
ΔP_2	21967.2 ± 1312.5	21829.8 ± 1061.2	26191.9 ± 1349.4	24546.4 ± 11[illegible].8
ΔP_3	9799.8 ± 684.5	11036.9 ± 657.3	11444.0 ± 710.8	11703.1 ± 709.4
ΔP_4	5562.5 ± 385.7	5988.0 ± 332.1	5725.4 ± 299.4	5974.4 ± 316.3
ΔP_5	3050.2 ± 233.0	3079.1 ± 200.2	2877.5 ± 239.1	2888.9 ± 215.4
ΔP_6	1452.8 ± 129.4	1559.6 ± 139.8	1772.1 ± 146.8	1354.3 ± 136.6
ΔP_7	941.3 ± 89.3	832.4 ± 77.1	866.3 ± 80.8	871.2 ± 99.3
ΔP_8	410.3 ± 39.4	397.8 ± 36.2	383.9 ± 35.0	238.3 ± 31.1
ΔP_9	113.4 ± 20.0	135.7 ± 18.9	86.4 ± 17.0	91.8 ± 17.5
ΔP_{10}	27.64 ± 6.34	10.12 ± 3.39	10.07 ± 3.89	9.65 ± 3.87
ΔP_{11}	1.77 ± 1.25	2.11 ± 1.51	1.02 ± 1.02	2.13 ± 1.51
ΔP_{12}	0.55 ± 0.55	0.83 ± 0.59	-	-

Table 7.2: Invariant differential inclusive cross section per nucleon for the process $\pi^- + \mathrm{Be} \rightarrow \pi^\circ + \mathrm{X}$. The units are pbarn/GeV^2/nucleon.

P_T range	$< P_T >$	$-0.7 < y < -0.5$	$-0.5 < y < -0.3$	$-0.3 < y < -0.1$
ΔP_4	4.11	1840.6 ± 268.4	3797.63 ± 445.6	4114.9 ± 377.0
ΔP_5	4.36	1599.7 ± 278.7	1739.59 ± 304.3	1977.8 ± 190.7
ΔP_6	4.61	777.8 ± 110.1	1069.32 ± 152.5	1163.8 ± 130.0
ΔP_7	4.86	521.1 ± 91.0	570.32 ± 74.9	542.8 ± 63.2
ΔP_8	5.19	143.1 ± 29.6	245.17 ± 35.4	224.6 ± 28.7
ΔP_9	5.69	35.8 ± 13.5	53.09 ± 11.4	100.6 ± 15.4
ΔP_{10}	6.32	4.77 ± 2.15	11.80 ± 3.61	11.6 ± 3.65
ΔP_{11}	7.41	1.43 ± 1.40	0.85 ± 0.85	0.76 ± 0.76
ΔP_{12}	8.92	–	–	–
	$-0.1 < y < 0.1$	$0.1 < y < 0.3$	$0.3 < y < 0.5$	$0.5 < y < 0.7$
ΔP_4	4466.5 ± 359.8	4684.6 ± 329.8	3948.8 ± 290.5	4205.3 ± 304.1
ΔP_5	2419.1 ± 204.4	2230.1 ± 171.4	2102.4 ± 171.9	1348.4 ± 139.2
ΔP_6	1095.1 ± 94.3	1064.7 ± 86.4	1205.9 ± 115.6	792.7 ± 82.1
ΔP_7	554.8 ± 56.6	632.7 ± 59.9	411.9 ± 48.9	288.2 ± 40.0
ΔP_8	251.7 ± 25.6	199.6 ± 23.5	158.4 ± 20.8	123.4 ± 18.0
ΔP_9	73.9 ± 13.0	62.9 ± 11.6	51.4 ± 10.6	24.5 ± 8.9
ΔP_{10}	10.29 ± 3.28	12.14 ± 3.26	10.33 ± 3.14	4.90 ± 2.21
ΔP_{11}	–	1.24 ± 0.88	–	–

Table 7.3: Invariant differential inclusive cross section per nucleon for the process $p + Be \rightarrow \pi^0 + X$. The units are pbarn/GeV^2/nucleon.

in these tables are statistical.

Cross Section Parametrization

The experimental results for the inclusive differential cross sections per nucleon

P_T range	$< P_T >$	$-0.7 < y < -0.2$	$-0.2 < y < 0.2$	$0.2 < y < 0.7$
ΔP_1	3.36	27017.6 ± 3913.4	54135.6 ± 5030.3	45775.4 ± 2905.2
ΔP_2	3.61	13914.3 ± 2119.4	21035.0 ± 1804.4	28439.7 ± 1854.0
ΔP_3	3.86	9837.7 ± 1789.2	11310.2 ± 1228.6	12391.5 ± 1138.2
ΔP_4	4.12	3179.0 ± 523.9	5580.5 ± 703.0	5684.4 ± 667.8
ΔP_5	4.38	2970.9 ± 781.3	3023.5 ± 489.5	3060.5 ± 412.4
ΔP_6	4.60	1037.5 ± 277.7	1688.6 ± 331.4	1063.8 ± 268.7
ΔP_7	4.83	596.5 ± 183.2	550.7 ± 186.3	890.6 ± 212.9
ΔP_8	5.18	286.5 ± 90.4	464.0 ± 116.6	227.5 ± 70.0
ΔP_9	5.74	60.1 ± 34.8	159.5 ± 66.3	71.4 ± 36.2
ΔP_{10}	6.40	23.31 ± 16.5	13.92 ± 13.92	17.01 ± 12.04
ΔP_{11}	7.19	7.59 ± 7.59	7.33 ± 7.33	-

Table 7.4: Invariant differential inclusive cross section per nucleon for the process $\pi^- + \mathrm{Cu} \rightarrow \pi^\circ + \mathrm{X}$. The units are pbarn/GeV^2/nucleon.

P_T range	$< P_T >$	$-0.7 < y < -0.2$	$-0.2 < y < 0.2$	$0.2 < y < 0.7$
ΔP_4	4.12	2636.2 ± 567.2	4790.3 ± 493.9	4671.7 ± 427.2
ΔP_5	4.36	1913.8 ± 335.6	2102.4 ± 305.0	2378.5 ± 271.2
ΔP_6	4.61	1106.0 ± 203.4	1142.3 ± 218.4	1069.0 ± 173.8
ΔP_7	4.89	518.8 ± 145.9	551.3 ± 144.3	545.0 ± 123.9
ΔP_8	5.18	183.2 ± 51.9	273.0 ± 69.3	209.8 ± 49.7
ΔP_9	5.69	42.5 ± 24.8	183.7 ± 56.0	20.57 ± 20.96
ΔP_{10}	6.27	28.11 ± 12.85	36.2 ± 16.3	-
ΔP_{11}	7.34	-	6.63 ± 6.63	-

Table 7.5: Invariant differential inclusive cross section per nucleon for the process $\mathrm{p} + \mathrm{Cu} \rightarrow \pi^\circ + \mathrm{X}$. The units are pbarn/GeV^2/nucleon.

for processes (7.1) and (7.2), presented in tables 7.2 and 7.3, were fitted to the form

$$E\frac{d\sigma}{d^3p} = C\frac{(1 - x_D)^m}{P_T^n} \tag{7.5}$$

with

$$\begin{aligned} x_D &= \sqrt{x_T^2 + (x_F - x_o)^2} \\ x_T &= \frac{2p_T}{\sqrt{s}} \\ x_F &\sim x_T \sinh y \end{aligned} \tag{7.6}$$

where y is the rapidity and x_F is the Feynman x in the center of mass. The cross section values were integrated over the corresponding p_T and rapidity intervals, and the resulting values were used in the fit. Table 7.6 shows the results of the fits for the two processes.

Process	m	n	x_o	C
$\pi^- + Be \rightarrow \pi^o + X$	5.87 ± 0.52	9.52 ± 0.29	0.066 ± 0.007	26.26 ± 7.46
$p + Be \rightarrow \pi^o + X$	6.81 ± 0.55	9.72 ± 0.29	0.01 ± 0.01	35.22 ± 9.84

Table 7.6: Parameters for the fits of the experimental cross sections.

Cross Section Distributions

Figures 7.1–7.3 show the cross section distributions as a function of p_T for processes (7.1)–(7.3) respectively, for each of the rapidity intervals mentioned above. The distributions in each figure, except for the topmost, have been successively scaled down by factors of 10. The dashed lines are representations of the functional form (7.5), integrated over the appropriate p_T and rapidity intervals. It can be seen

from these figures that the shape of the cross sections in each process, is essentially independent of the rapidity range.

The cross sections as a function of rapidity for different p_T intervals, for interactions between beryllium and π^- and protons, are shown in figures 7.4 and 7.5. The dashed lines correspond to the functional form in the corresponding intervals. The deviations from the fit are more obvious in the rapidity distributions, especially in the negative rapidity regions. The reason for this behavior is not clearly understood at this point, although it appears to be correlated to the energy scale fluctuations mentioned in chapter 6. Table 7.7 lists the π° measured for the seven rapidity intervals used in the distributions above. These values were determined by obtaining the mass distribution for each rapidity bin after applying the corrections described in chapter 6. It can be seen from these values that the mass tends to be lower at negative rapidities ($\sim 1\%$) and higher ($\sim 2\%$) at positive rapidities, with the best agreement in the central region. A 1% fluctuation in the π° mass translates into a fluctuation of approximately 10% in the cross section, in addition to more subtle effects in the background subtraction. Studies are being performed at this point to efficiently handle these scale fluctuations.

Comparing figures 7.4 and 7.5, one can observe that the $\pi^- + \mathrm{Be}$ distribution peaks at a value of ~ 0.3 units of rapidity, while the $\mathrm{p} + \mathrm{Be}$ distribution peaks at a value of ~ 0.05. This behavior can be explained by the presence of one more valence quark in the proton than in the π^-. Kinematically this corresponds to a higher fraction of the hadron momentum being carried by the parton in the π^-, which translates into a boost in the forward region with respect to the proton.

Figures 7.6–7.9 show the p_T distributions of the differential cross sections for the

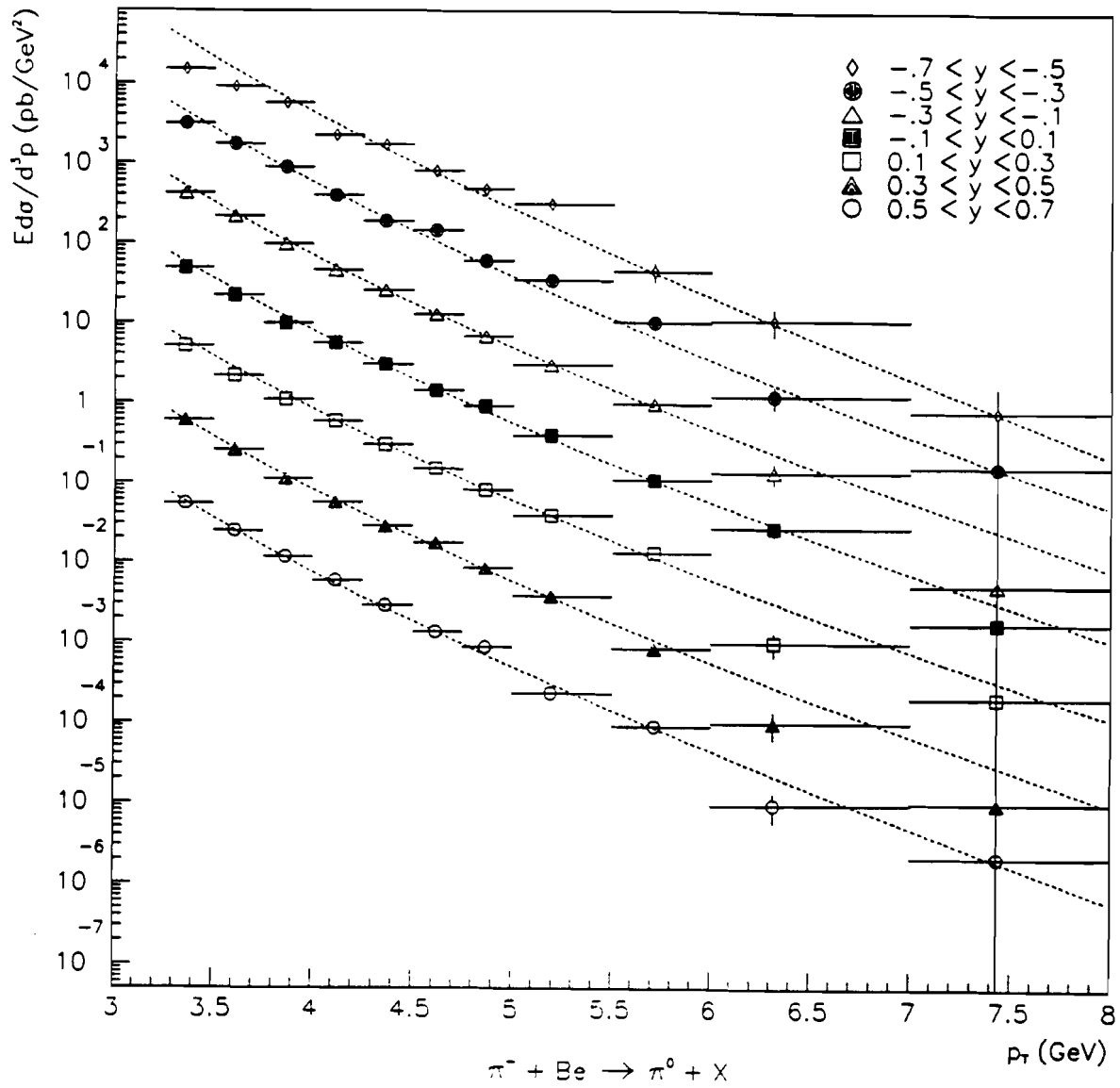

Figure 7.1: Invariant differential inclusive cross sections per nucleon as a function of p_T for the process $\pi^- + \mathrm{Be} \rightarrow \pi^0 + X$ for different rapidity regions. The distributions are successively scaled down by powers of 10. The dashed lines correspond to the function in equation (7.5), integrated over the corresponding rapidity and p_T intervals.

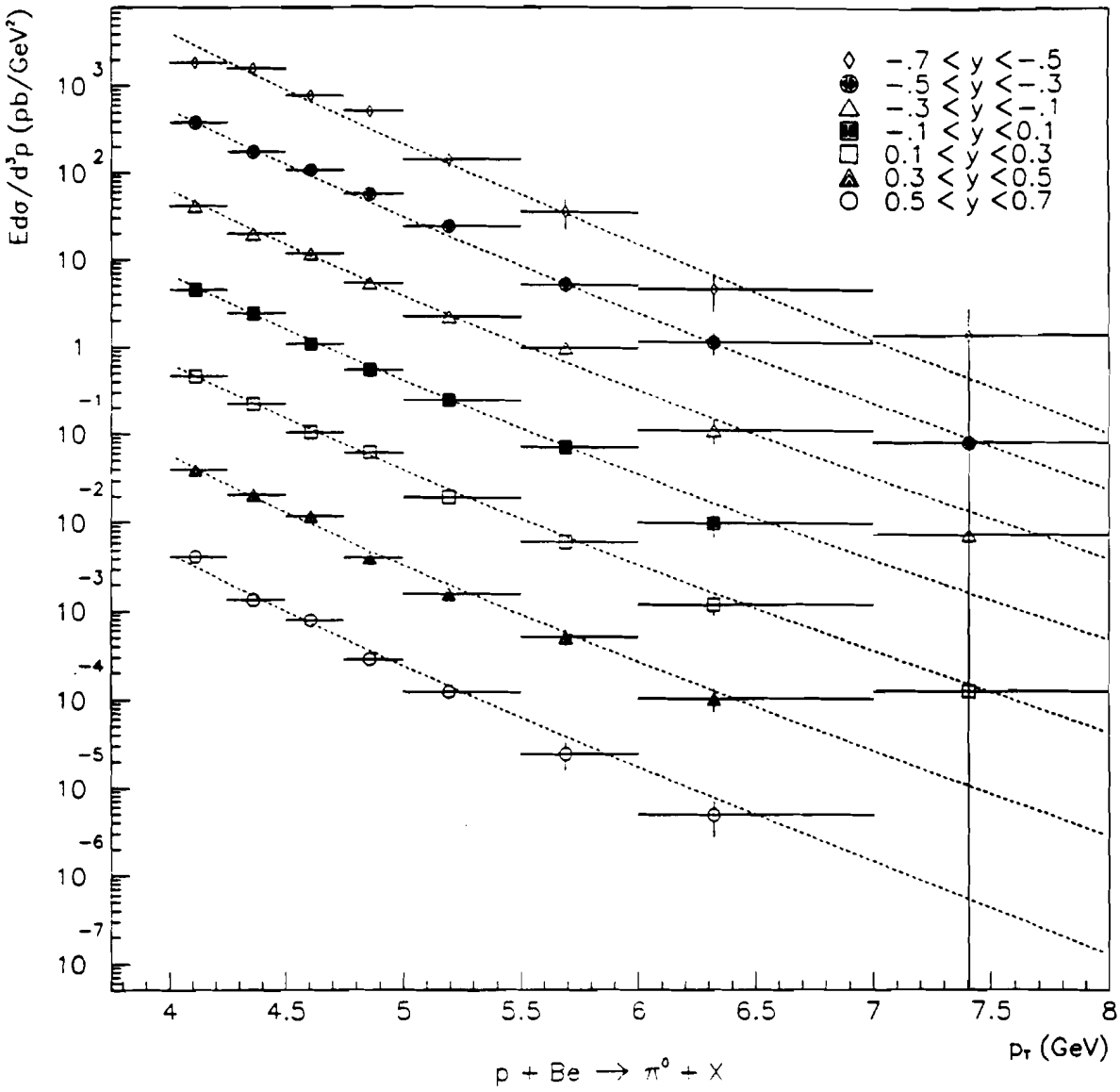

Figure 7.2: Invariant differential inclusive cross sections per nucleon as a function of p_T for the process $p + Be \rightarrow \pi^0 + X$ for different rapidity regions. The distributions are successively scaled down by powers of 10. The dashed lines correspond to the function in equation (7.5), integrated over the corresponding rapidity and p_T intervals.

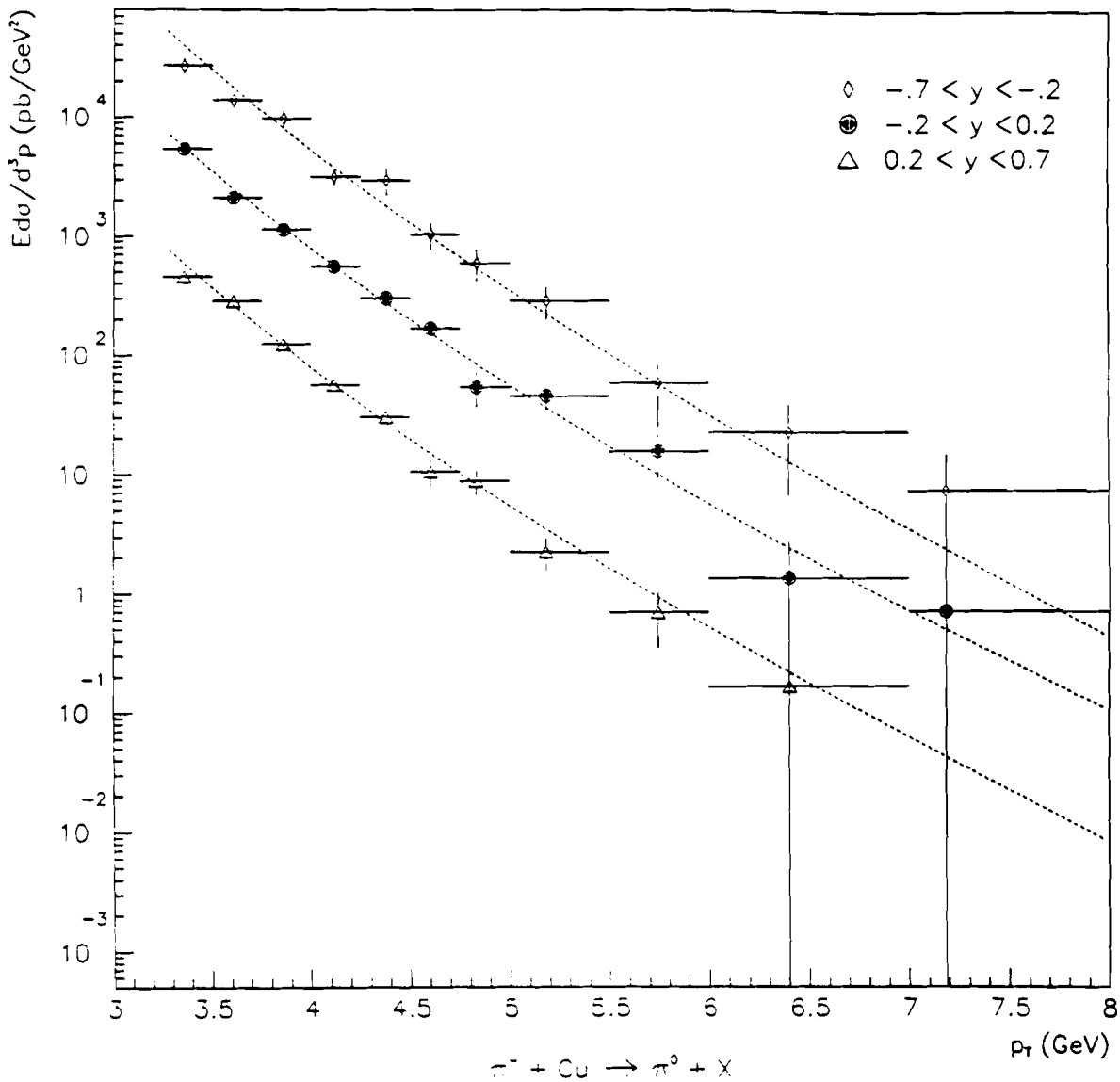

Figure 7.3: Invariant differential inclusive cross section per nucleon as a function of p_T for the process $\pi^- + \mathrm{Cu} \rightarrow \pi^0 + \mathrm{X}$, for different rapidity regions. The distributions are successively scaled down by powers of 10. The dashed lines correspond to the function in equation (7.5), integrated over the corresponding rapidity and p_T intervals.

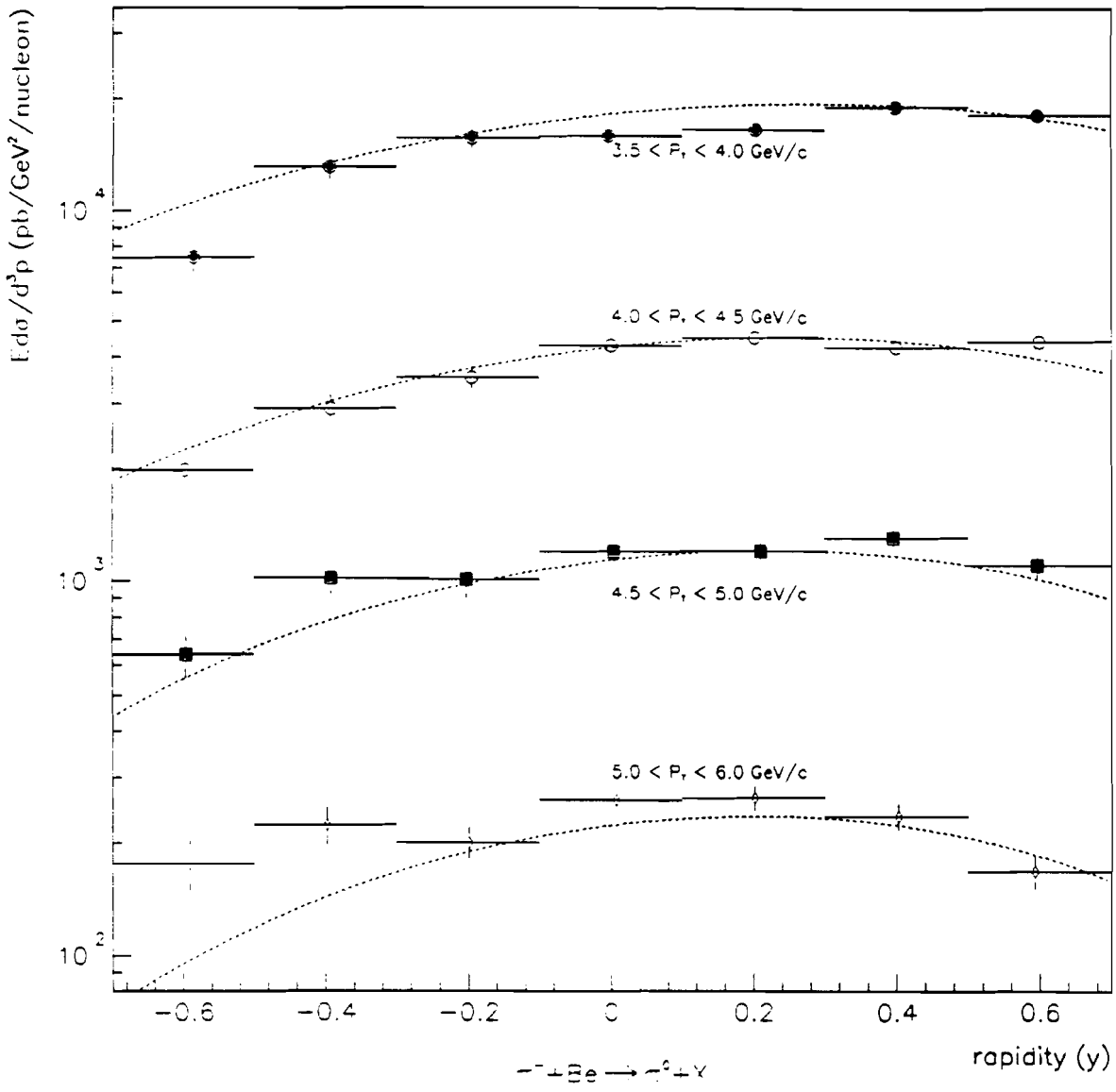

Figure 7.4: Invariant differential inclusive cross section per nucleon as a function of rapidity (y) for the process $\pi^- + \mathrm{Be} \rightarrow \pi^\circ + \mathrm{X}$, for different p_T intervals. The dashed lines correspond to the function in equation (7.5), integrated over the corresponding rapidity and p_T intervals.

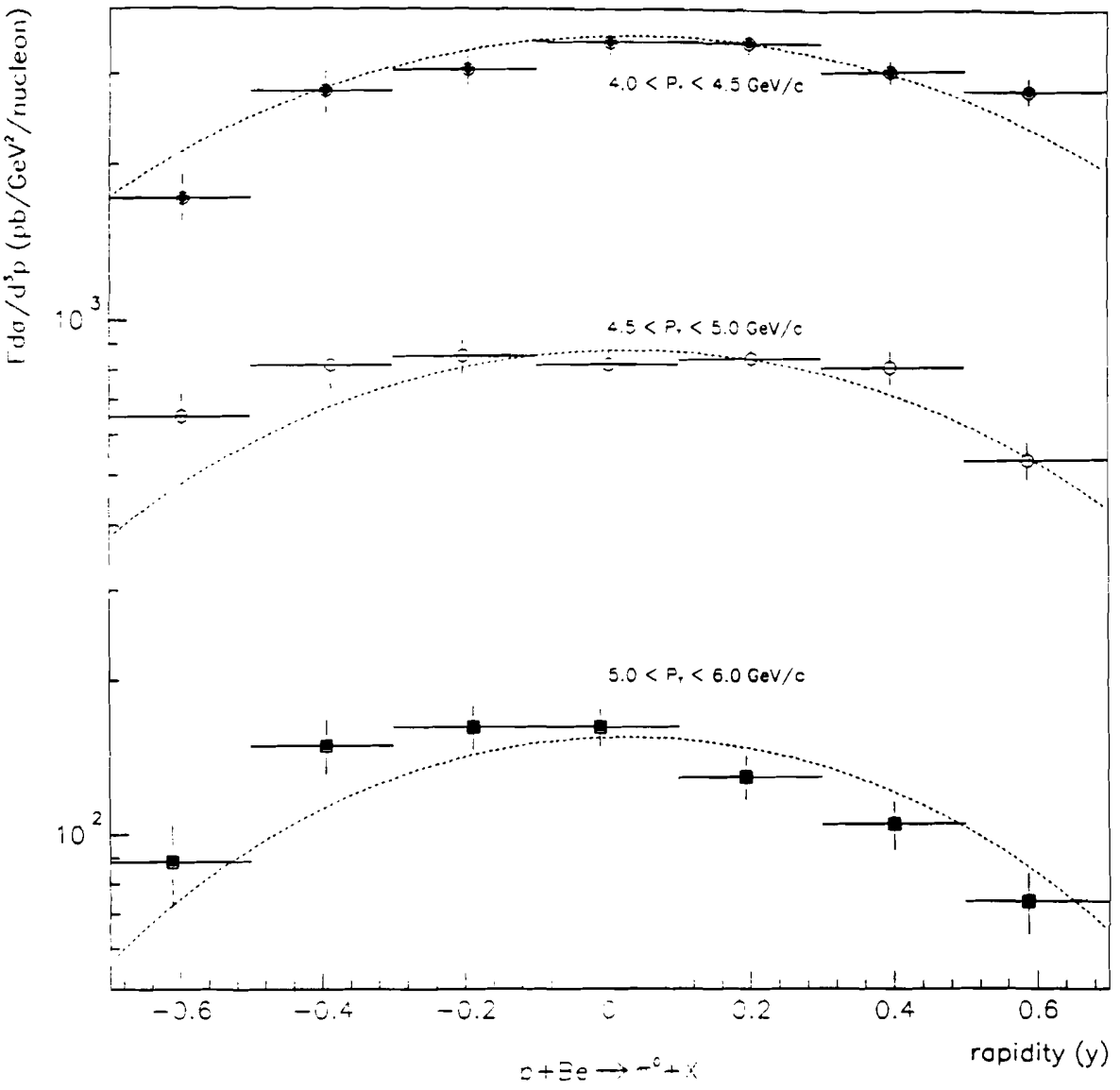

Figure 7.5: Invariant differential inclusive cross section per nucleon as a function of rapidity (y) for the process $p + Be \rightarrow \pi^0 + X$, for different p_T intervals. The dashed lines correspond to the function in equation (7.5), integrated over the corresponding rapidity and p_T intervals.

rapidity	M_{π° (MeV)	$M_{\pi^\circ}/135\,\mathrm{MeV}$
$-0.7 < y < -0.5$	133.2	0.99
$-0.5 < y < -0.3$	133.9	0.99
$-0\ 3 < y < -0.1$	135.7	1.01
$-0.1 < y < 0.1$	136.3	1.01
$0.1 < y < 0.3$	135.7	1.01
$0.3 < y < 0.5$	137.9	1.02
$0.5 < y < 0.7$	138.2	1.02

Table 7.7: π° mass as a function of rapidity.

four processes (7.1)–(7.4), integrated over the full rapidity range ($-0.7 < y < 0.7$). The functional form in (7.5), integrated over the corresponding p_T and rapidity intervals, has been superimposed in each case. These distributions will be used in the measurement of the nuclear and beam dependence of the cross sections, described in the following sections.

7.2 Nuclear Dependence

It is interesting to measure the ratio of the cross sections for π° production from beryllium and from copper, to establish the dependence on A. By measuring the ratio between the cross sections, and assuming a scaling of the cross section per nucleus of the form A^α instead of A, one can determine the nuclear dependence of the cross section (see section 1.3). If instead of using cross sections per nucleus one uses cross sections per nucleon in the calculation of the ratio, equation (1.11) can

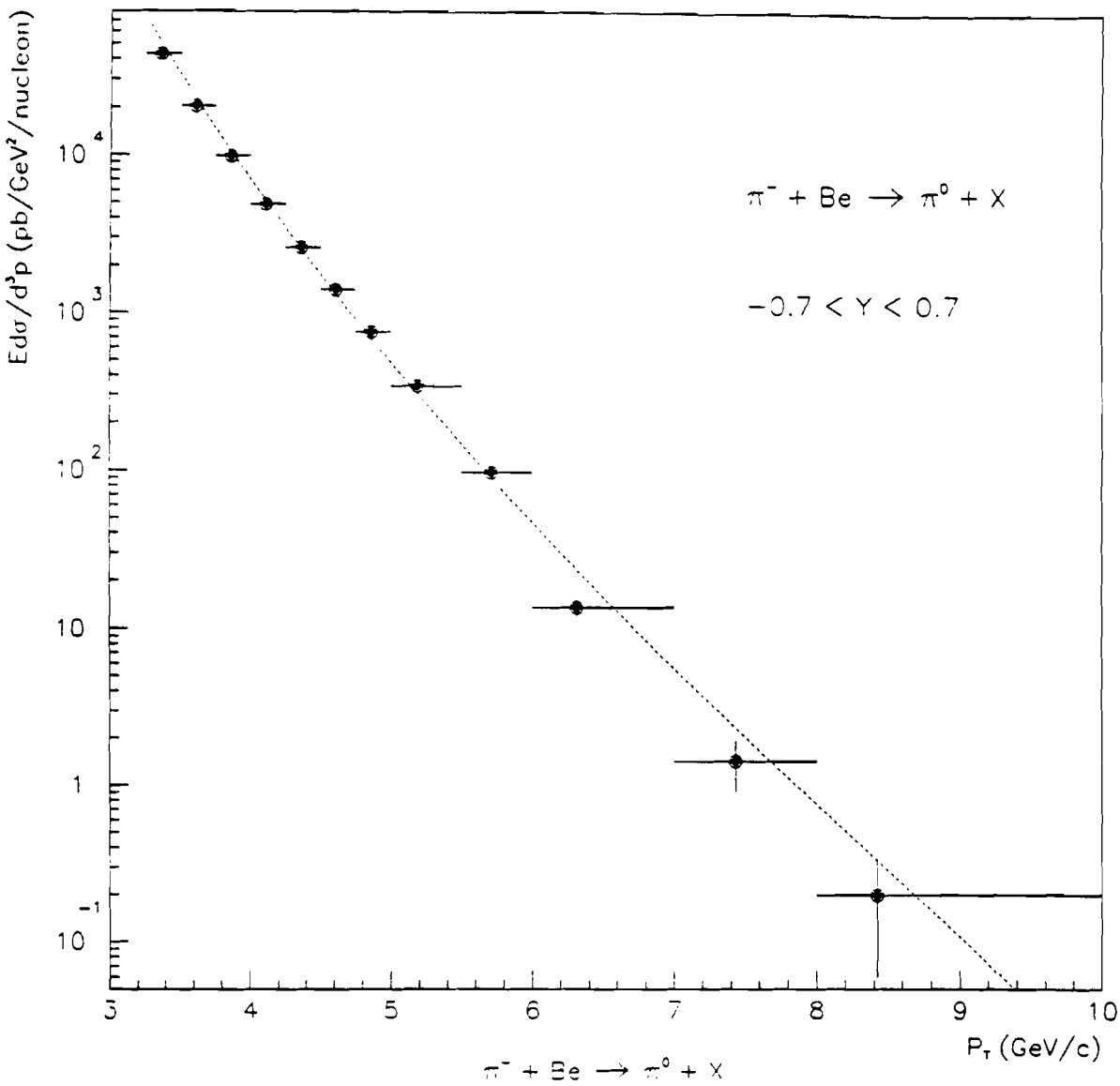

Figure 7.6: Invariant differential inclusive cross section per nucleon as a function of p_T for the process $\pi^- + \mathrm{Be} \rightarrow \pi^0 + X$ integrated over the interval $-0.7 < y < 0.7$. The dashed line corresponds to the function in equation (7.5), integrated over the corresponding rapidity and p_T intervals.

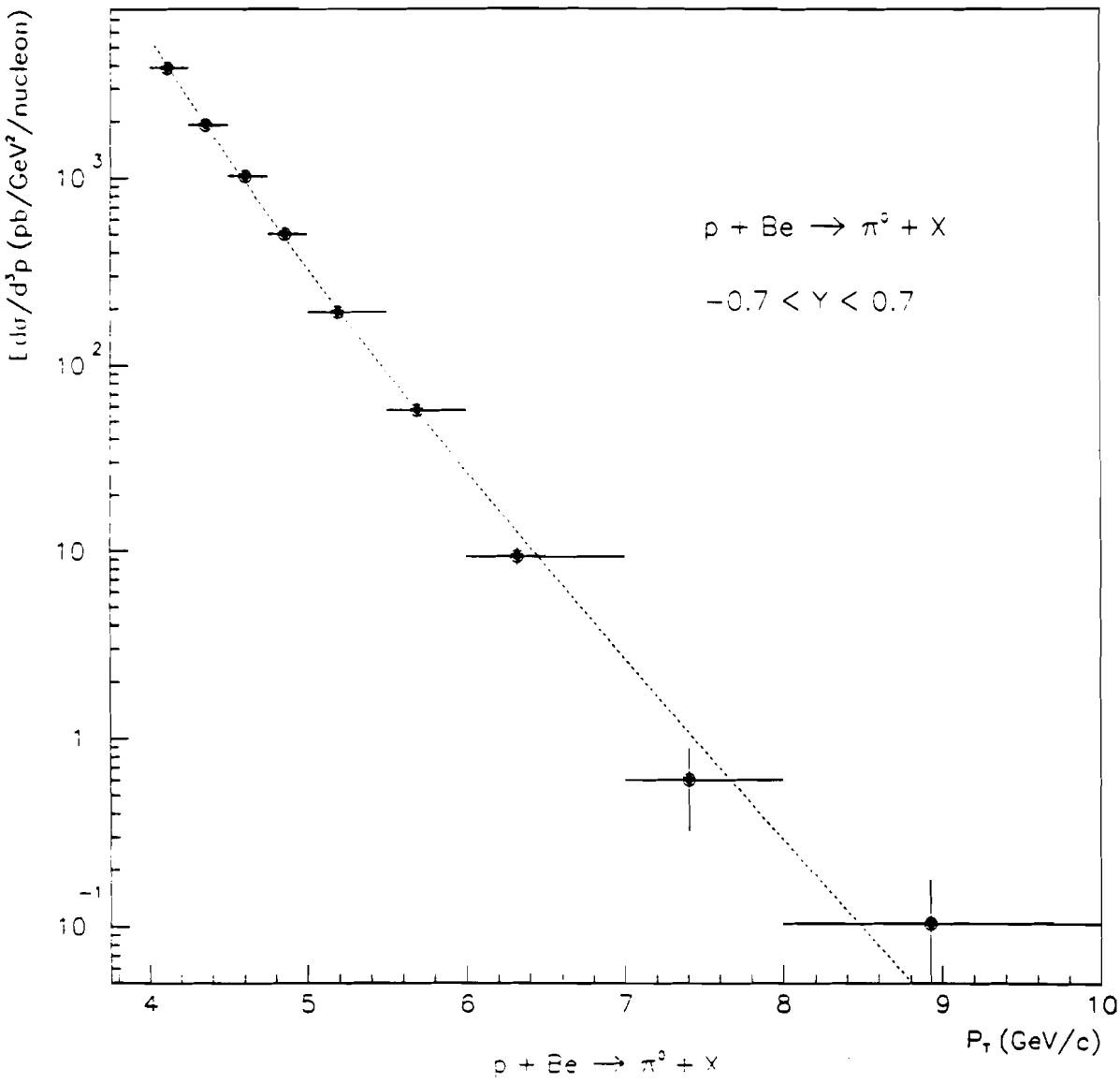

Figure 7.7: Invariant differential inclusive cross section per nucleon as a function of p_T for the process $p + Be \rightarrow \pi^0 + X$ integrated over the interval $-0.7 < y < 0.7$. The dashed line corresponds to the function in equation (7.5), integrated over the corresponding rapidity and p_T intervals.

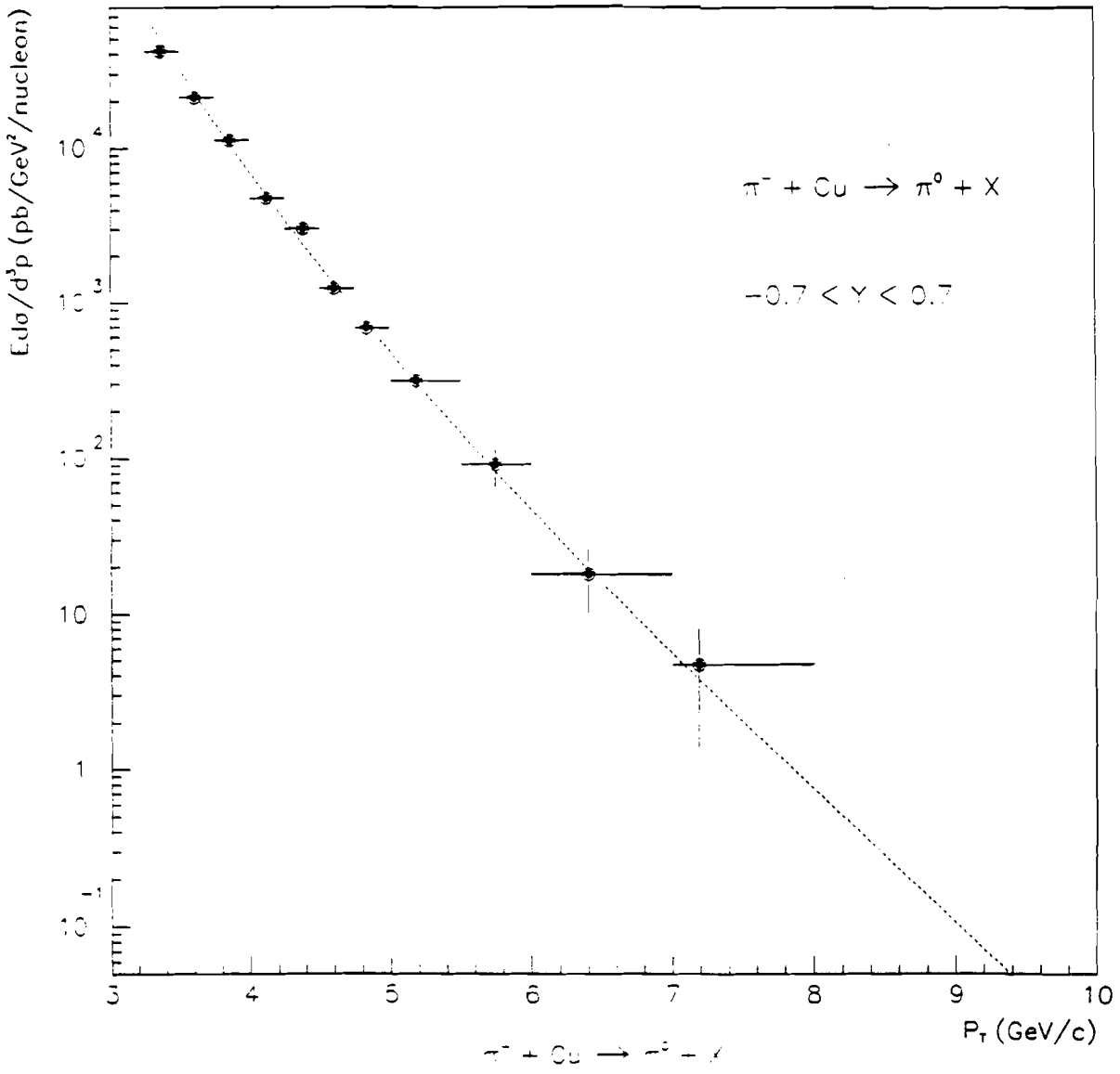

Figure 7.8: Invariant differential inclusive cross section per nucleon as a function of p_T for the process $\pi^- + Cu \rightarrow \pi^0 + X$, integrated over the interval $-0.7 < y < 0.7$. The dashed line corresponds to the function in equation (7.5), integrated over the corresponding rapidity and p_T intervals.

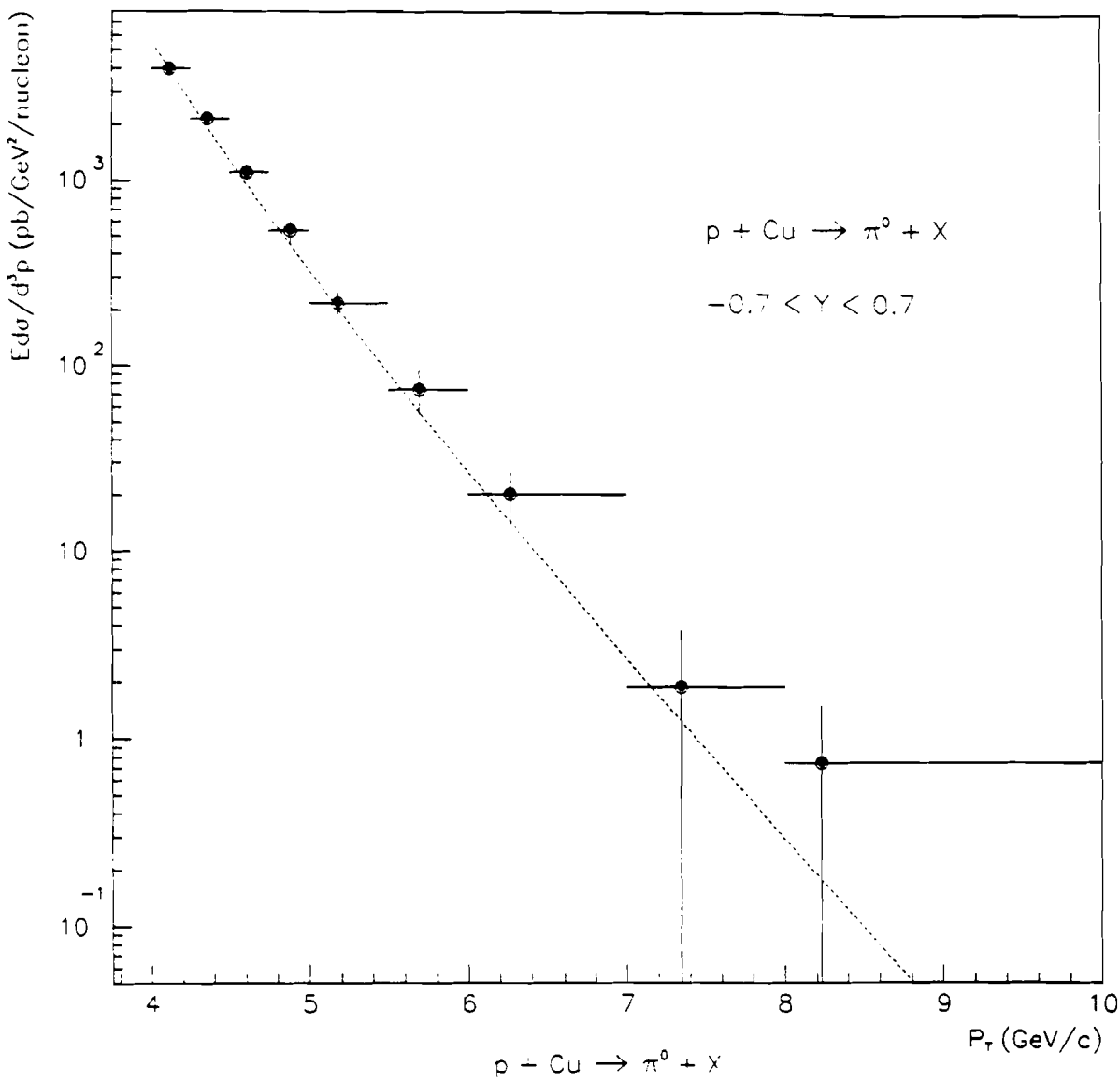

Figure 7.9: Invariant differential inclusive cross section per nucleon as a function of p_T for the process $p + Cu \rightarrow \pi^0 + X$, integrated over the interval $-0.7 < y < 0.7$. The dashed line corresponds to the function in equation (7.5), integrated over the corresponding rapidity and p_T intervals.

be substituted by

$$\frac{\sigma(Be)}{\sigma(Cu)} = \left(\frac{A_{Be}}{A_{Cu}}\right)^{\alpha-1} \tag{7.7}$$

and the value of α will be

$$\alpha = 1 + \frac{\ln\left(\sigma(\mathrm{Be})/\sigma(\mathrm{Cu})\right)}{\ln\left(\mathrm{A_{Be}}/\mathrm{A_{Cu}}\right)} \tag{7.8}$$

where σ(Be) and σ(Cu) are the cross sections per nucleon for interactions in the given target. Values of α have been calculated for proton and π^- cross sections, in different p_T and rapidity intervals.

Figure 7.10(a) shows the distribution for α as a function of p_T for the π^- beam cross sections. The corresponding distribution for proton beam data is shown in figure 7.10(b). In both cases, the cross sections were integrated and averaged over rapidity in the interval $-0.7 < y < 0.7$. The values of α for the different p_T intervals are listed in table 7.8. The dependence of α on rapidity was also measured for both π^- and proton data. Three rapidity regions were examined: $-0.7 < y < -0.2$, $-0.2 < y < 0.2$, and $0.2 < y < 0.7$. The measurements were performed over three p_T intervals for π^- beam, and two p_T intervals for proton beam data. The values of α for each region are given in table 7.9

7.3 Beam Dependence of the Cross Sections

The ratio of the π^0 invariant differential cross sections per nucleon for $\pi^- + \mathrm{Be}$ and $\mathrm{p} + \mathrm{Be}$ is shown in figure 7.11. The cross sections used in the ratio where measured over rapidities between -0.7 and 0.7. The ratio of the fits for the two processes has been superimposed in this plot. The deviations from the curve can be related to fluctuations in the $\pi^- + \mathrm{Be}$ distribution, as observed in figure 7.6.

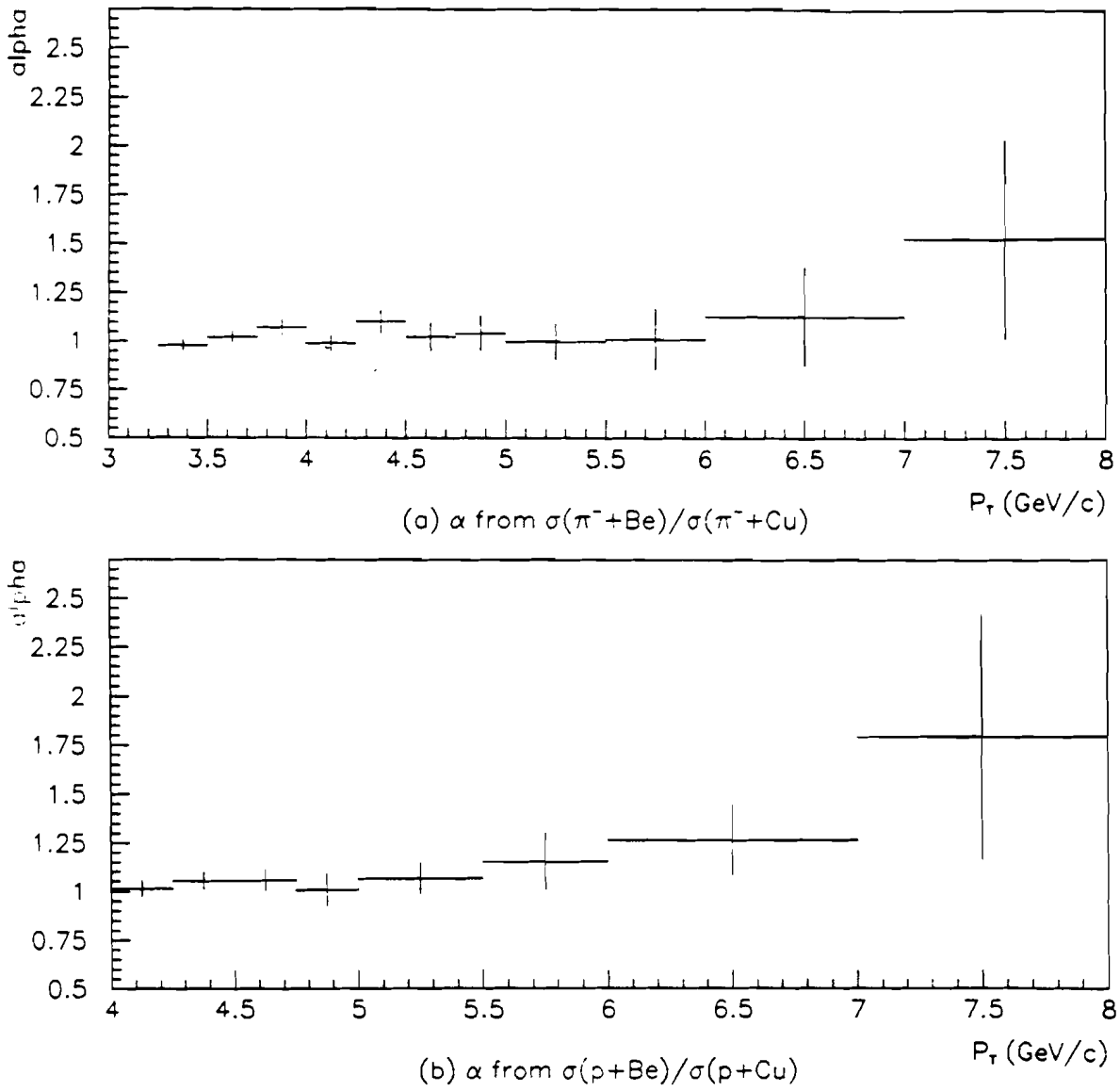

Figure 7.10: α as a function of p_T: (a) determined from the ratio $\sigma(\pi^- + \mathrm{Be})/\sigma(\pi^- + \mathrm{Cu})$; (b) determined from the ratio $\sigma(\mathrm{p} + \mathrm{Be})/\sigma(\mathrm{p} + \mathrm{Cu})$.

P_T range	α from π^- data	α from proton data
ΔP_1	0.98 ± 0.03	-
ΔP_2	1.02 ± 0.03	-
ΔP_3	1.07 ± 0.04	1.01 ± 0.04
ΔP_4	0.99 ± 0.04	1.05 ± 0.05
ΔP_5	1.10 ± 0.06	1.06 ± 0.06
ΔP_6	1.02 ± 0.07	1.01 ± 0.08
ΔP_7	1.04 ± 0.09	1.07 ± 0.08
ΔP_8	1.00 ± 0.09	1.15 ± 0.15
ΔP_9	1.01 ± 0.16	1.26 ± 0.18
ΔP_{10}	1.13 ± 0.25	1.79 ± 0.63
ΔP_{11}	1.53 ± 0.51	1.58 ± 0.63

Table 7.8: α dependence on p_T, obtained using cross sections integrated and averaged over the range $-0.7 < y < 0.7$.

y range	α from π^- data		
	$3.5 < P_T < 4.0$	$4.0 < P_T < 4.5$	$4.5 < P_T < 7.0$
$-0.7 < y < -0.2$	1.04 ± 0.07	1.12 ± 0.09	1.08 ± 0.09
$-0.2 < y < 0.2$	1.00 ± 0.04	0.97 ± 0.06	1.07 ± 0.07
$0.2 < y < 0.7$	1.06 ± 0.03	0.97 ± 0.05	0.93 ± 0.08
	α from proton data		
$-0.7 < y < -0.2$	-	1.07 ± 0.10	1.05 ± 0.07
$-0.2 < y < 0.2$	-	0.95 ± 0.08	1.09 ± 0.07
$0.2 < y < 0.7$	-	1.13 ± 0.06	1.03 ± 0.06

Table 7.9: α dependence on rapidity for different p_T regions.

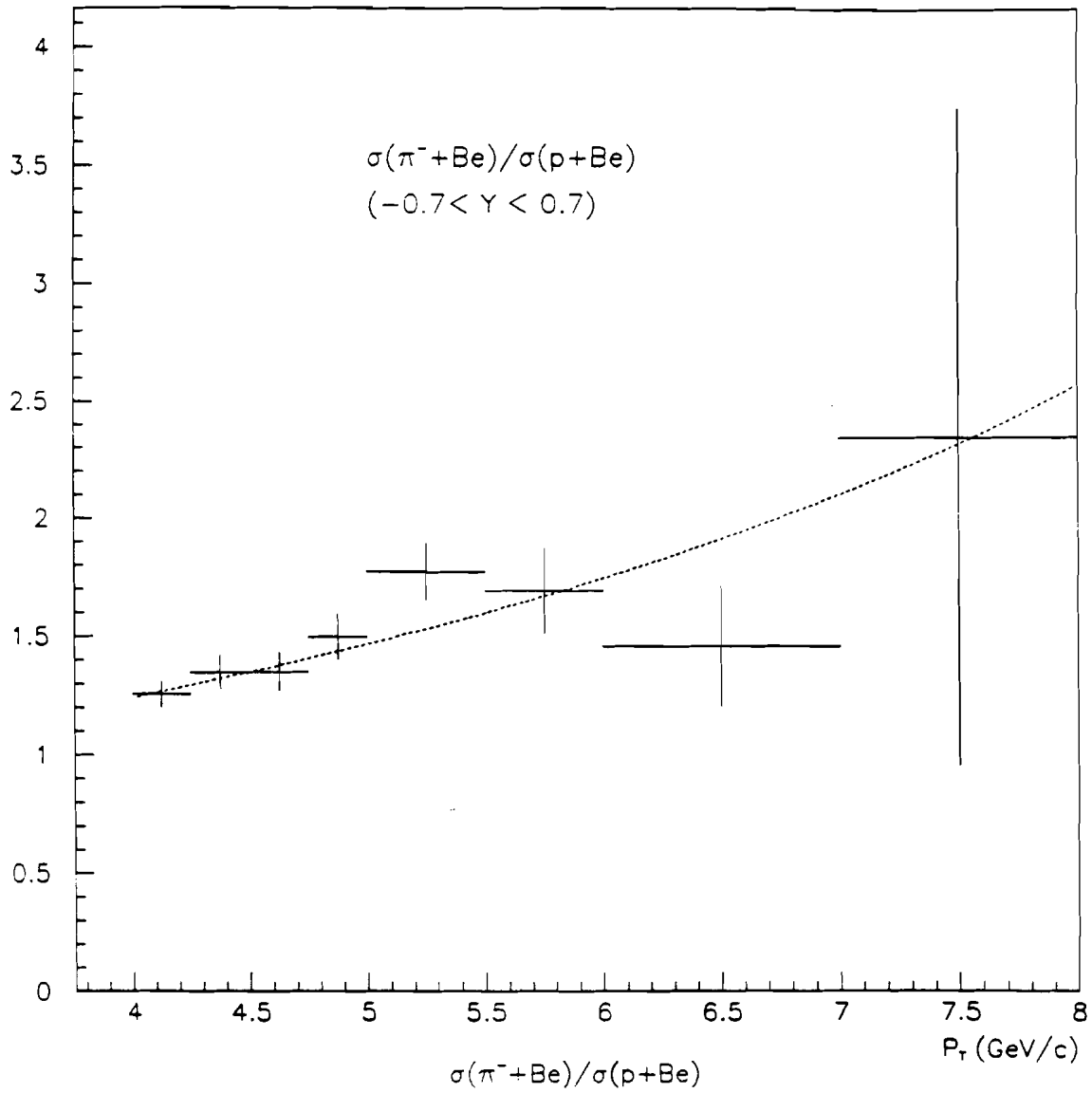

Figure 7.11: Beam dependence of the cross section as a function of p_T, determined from the ratio $\sigma(\pi^- + \mathrm{Be})/\sigma(\mathrm{p} + \mathrm{Be})$. The cross sections were measured over the interval $-0.7 < y < 0.7$. Superimposed is the ratio of the fits for the two processes.

It can be seen that the ratio in the p_T range included, is larger than 1 and increases as a function of p_T. As mentioned for the rapidity distributions, there is one more quark in the proton than in the π^-, and therefore, the individual partons in the latter will have a larger fraction of the momentum than those in the proton.* Thus, π^0s produced by incident π^-s will tend to have higher p_T than those produced by incident protons, in agreement with the ratio being larger than 1. The increase as a function of p_T is related to the contribution from the $u\bar{u}$ annihilation diagram in the $\pi^- + \mathrm{Be}$ process and which does not exist in the proton interactions.

7.4 Comparison with Theoretical Predictions

Differential cross sections for π^0 production in processes (7.1) and (7.2) have been calculated from QCD predictions, using a program provided by Jeff Owens. This program integrates inclusive differential cross sections for single hadron production using the "leading-log" approximation (see equation 1.2). The structure functions used in the integration are the standard Duke-Owens set 1 for nucleons,[33] and Owens set 1 for pions.[34] These functions use a value of Λ of 200 MeV. The fragmentation functions were determined by Owens.[35]

Distributions have been obtained for the standard choices $Q^2 = P_T^2$ and $Q^2 = 0.25P_T^2$, with no k_T smearing included. As mentioned in chapter 1, the value of α_s and the distribution and fragmentation functions depend on the choice of Q^2. Figures 7.12 and 7.13 show a comparison of the QCD predictions with the data. The fits to the experimental cross sections have been superimposed in these plots. It appears that the data tends to be in better agreement with the predictions for

* Recall that for both positive and negative data, 530 GeV/c incident beams were used

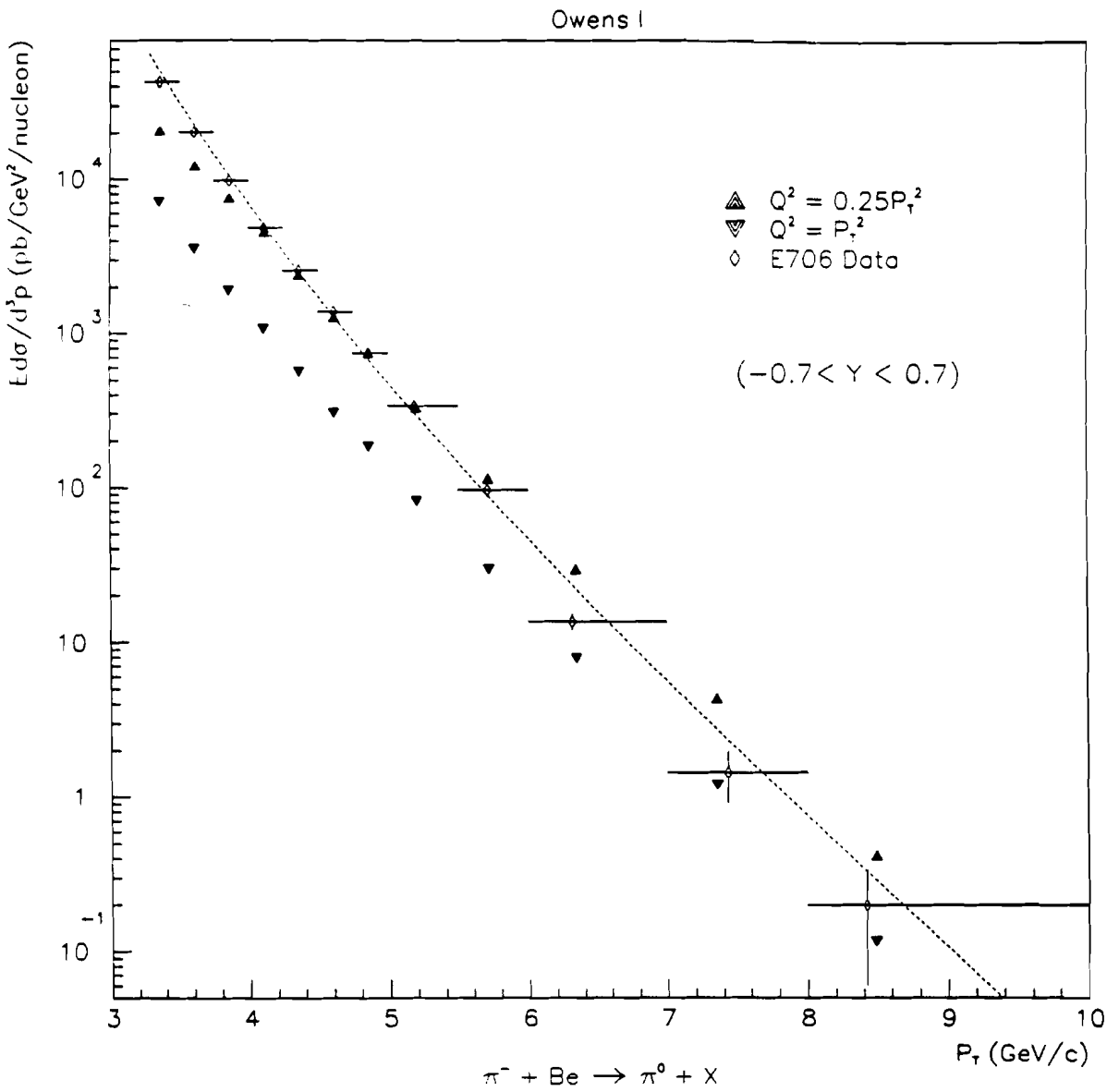

Figure 7.12: Comparison of π^0 data from interactions between π^- and beryllium with QCD predictions. Owens set 1 with $\Lambda = 200\,\mathrm{GeV}$ was used, with $Q^2 = P_T^2$ and $Q^2 = 0.25P_T^2$.

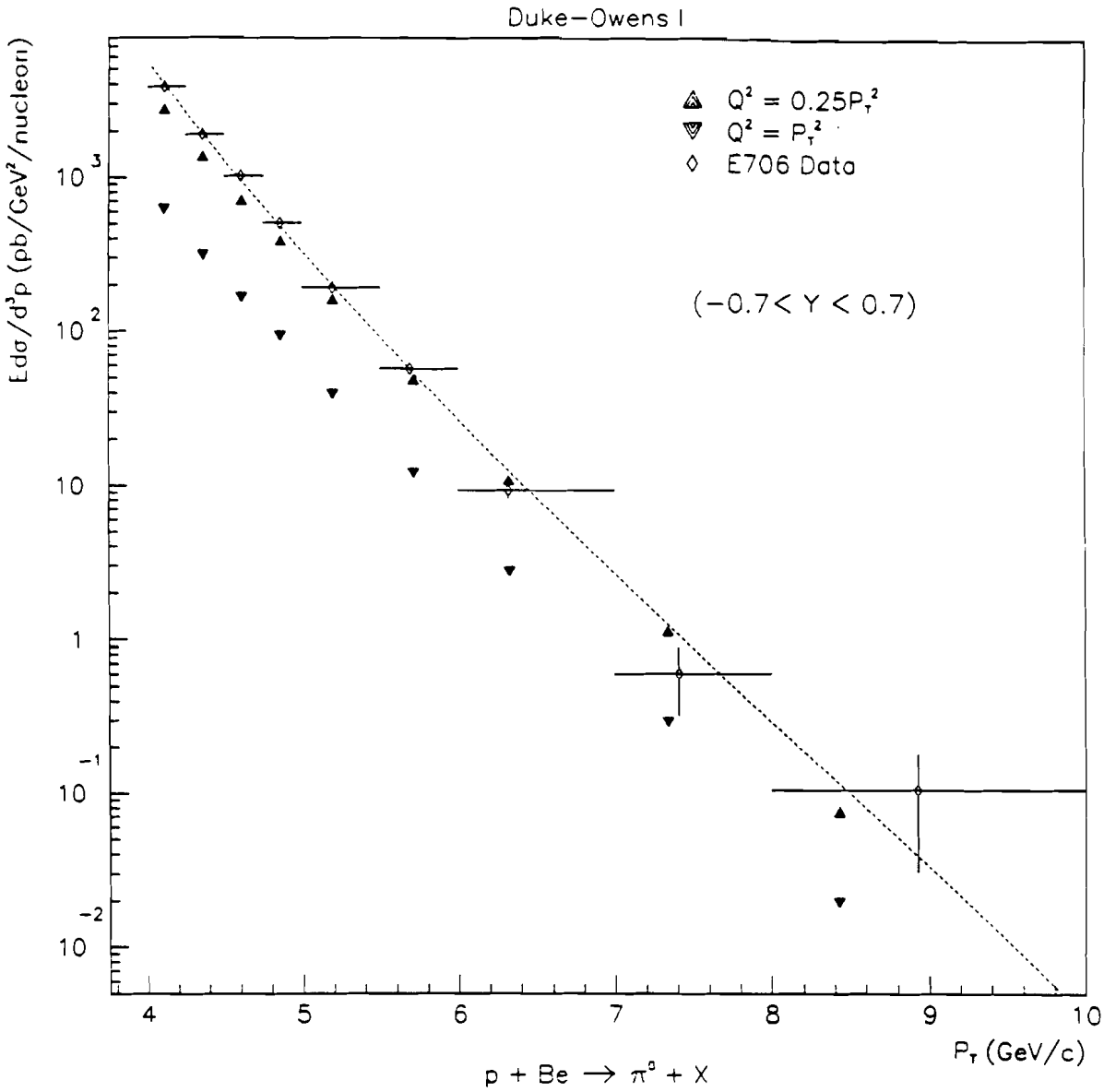

Figure 7.13: Comparison of π^0 data from interactions between protons and beryllium with QCD predictions. Duke–Owens set 1 with $\Lambda = 200\,\mathrm{GeV}$ was used, with $Q^2 = P_T^2$ and $Q^2 = 0.25P_T^2$.

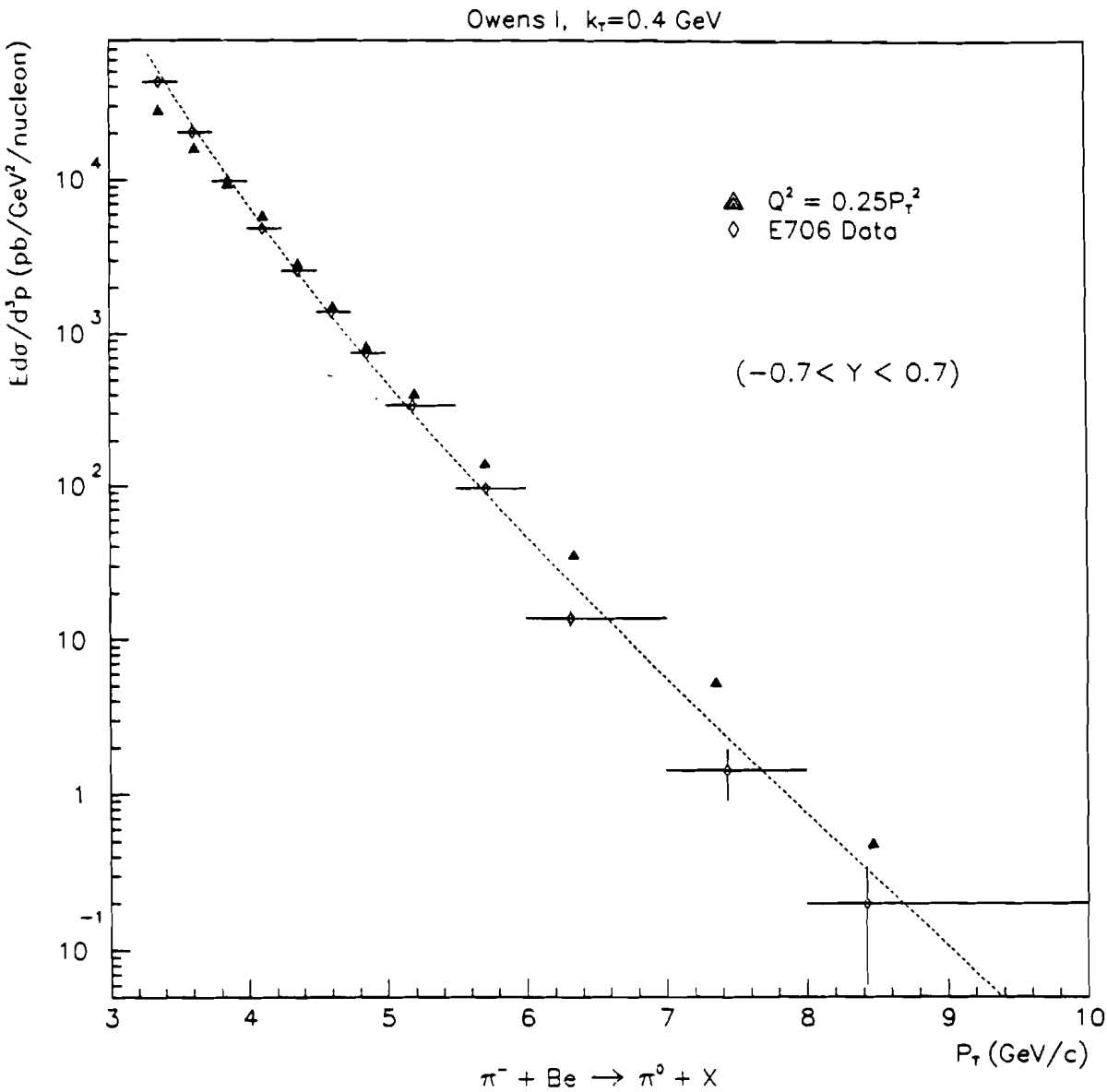

Figure 7.14: Comparison of π^0 data from interactions between π^- and beryllium with QCD predictions. Owens set 1 with $\Lambda = 200\,\text{GeV}$ was used, with $Q^2 = P_T^2$ and $Q^2 = 0.25P_T^2$. A value of 0.4 GeV for k_T has been used to include smearing contributions.

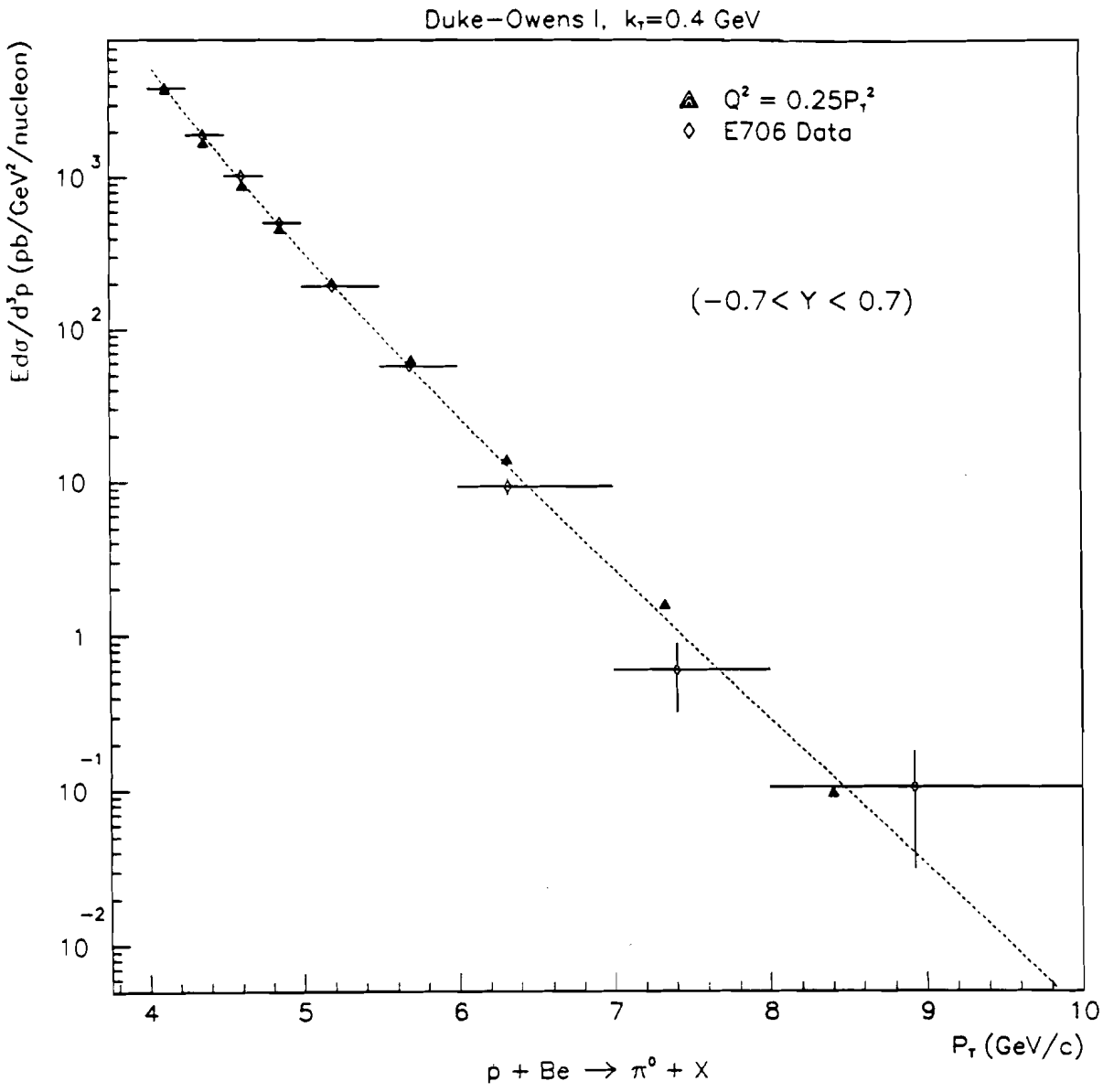

Figure 7.15: Comparison of π^0 data from interactions between protons and beryllium with QCD predictions. Duke–Owens set 1 with $\Lambda = 200\,\mathrm{GeV}$ was used, with $Q^2 = P_T^2$ and $Q^2 = 0.25P_T^2$. A value of 0.4 GeV for k_T has been used to include smearing contributions.

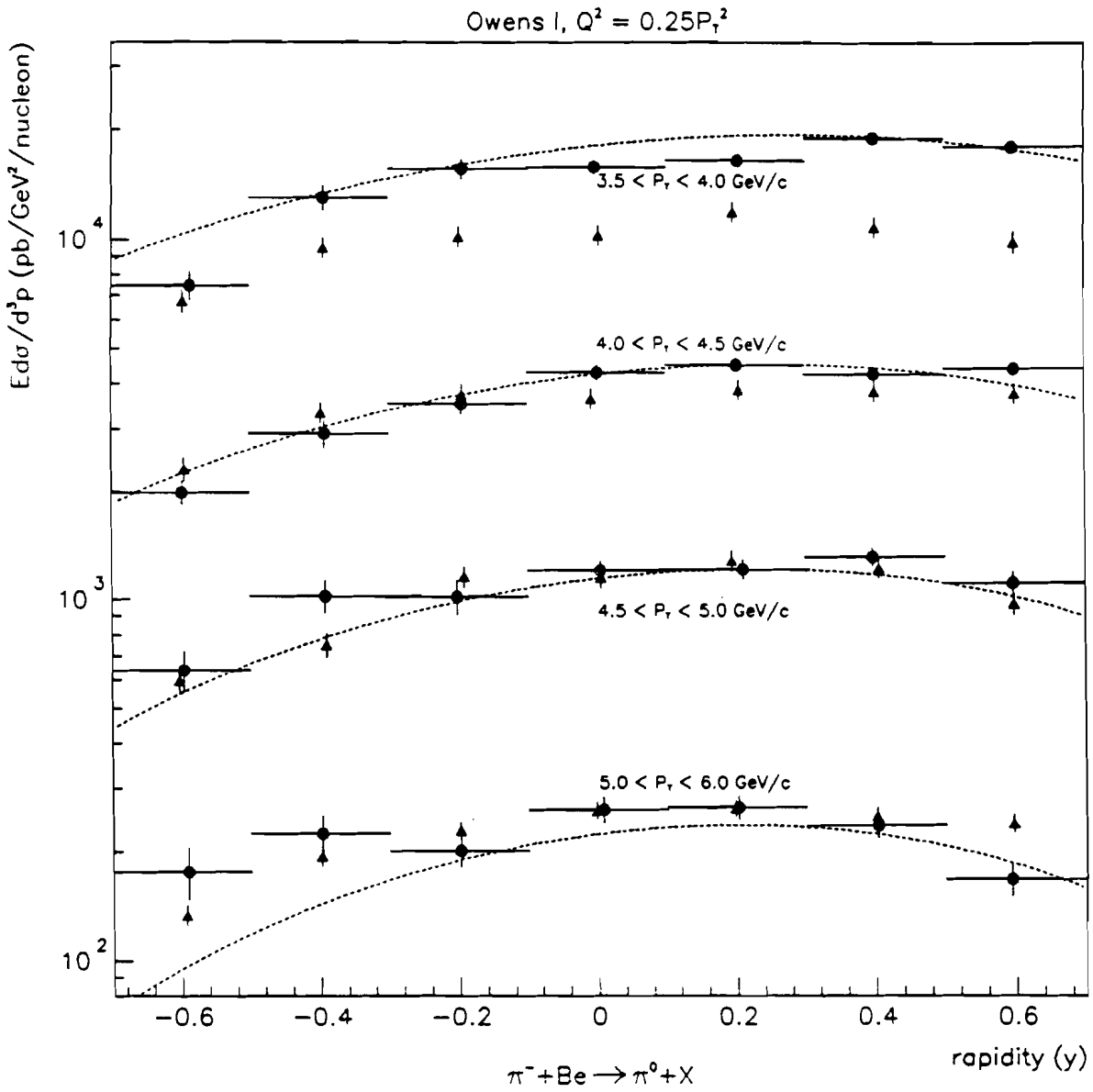

Figure 7.16: Comparison of π^0 data from interactions between π^- and beryllium with QCD predictions as a function of rapidity. Owens set 1 with $\Lambda = 200\,\mathrm{GeV}$ was used, with $Q^2 = P_T^2$ and $Q^2 = 0.25P_T^2$. The solid dots are the data points and the triangles are the values from QCD predictions.

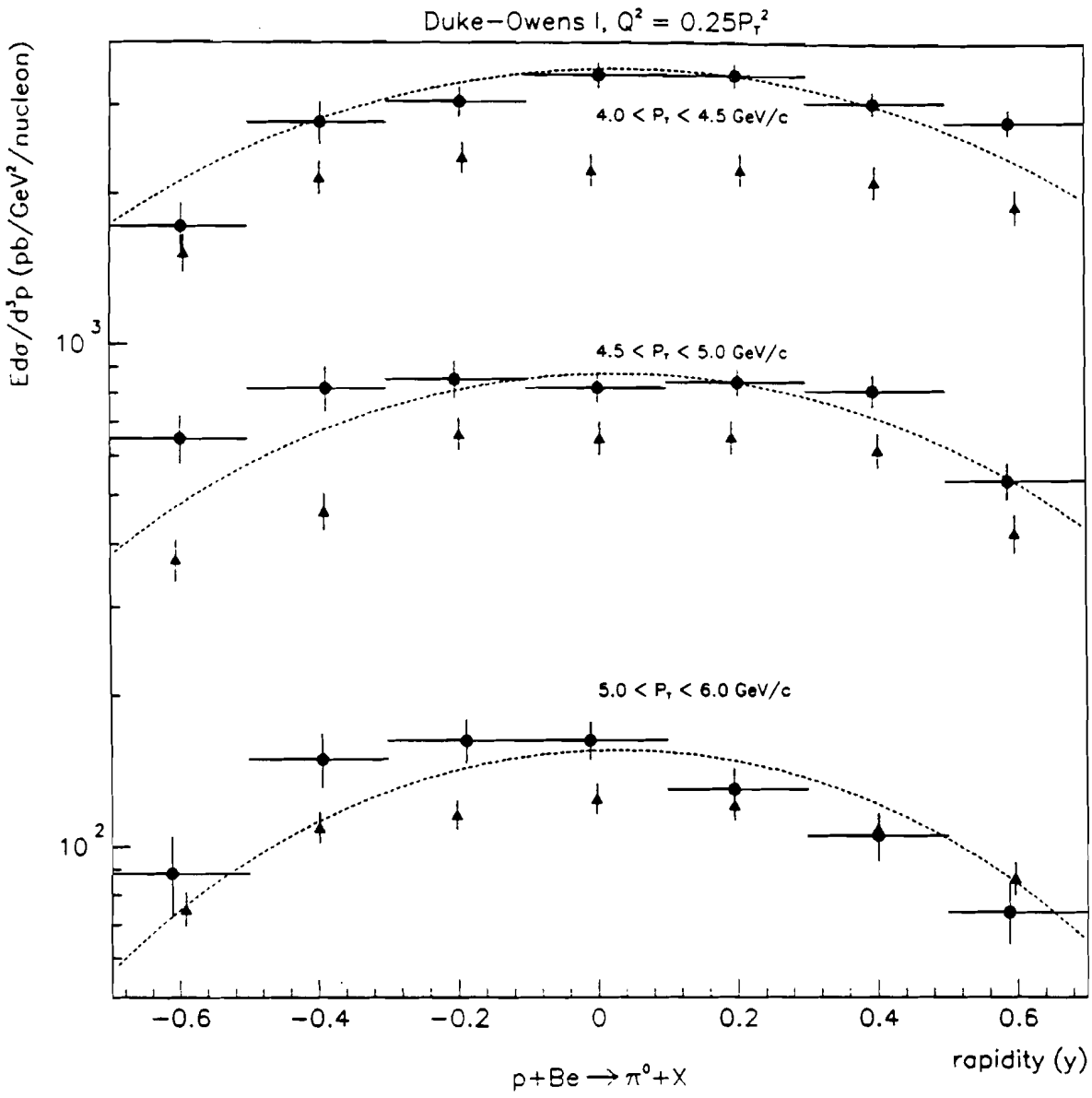

Figure 7.17: Comparison of π^0 data from interactions between protons and beryllium with QCD predictions as a function of rapidity. Duke–Owens set 1 with $\Lambda = 200$ GeV was used, with $Q^2 = P_T^2$ and $Q^2 = 0.25P_T^2$. The solid dots are the data points and the triangles are the values from QCD predictions.

$Q^2 = 0.25P_T^2$. However, the cross section for $\pi^- + Be$ decreases more rapidly as a function of p_T than the the predicted distribution, with the best agreement observed for p_T values between 4 and 6 GeV. In the proton case, a better agreement is observed in the slopes of the two distributions, but the data is approximately a factor of 1.4 higher than the predicted values.

Figures 7.14 and 7.15 show a comparison between the data and the predictions from QCD for which smearing contributions have been included, using a value of 0.4 GeV for k_T. It can be observed that while a better agreement between the data and the QCD predictions is achieved for proton results, such is not the case for the results from π^- data. Finally, comparisons between the experimental results and the distributions from QCD predictions as a function of rapidity are shown in figures 7.16 and 7.17. In these plots, the solid points correspond to the experimental results, the triangles show the predicted values, and the curves correspond to the fits of the function in (7.5) obtained from the data. The similarity of the shape of the rapidity distributions is clear in these two figures but, as seen in the p_T distributions, differences in the magnitudes of the cross sections for $p_T < 4.0$ GeV/c in the π^- data, and for all p_T's in the proton data, are clearly seen.

7.5 Summary

Results on the performance of the trigger during the 1987-88 experimental run of experiment E706 have been presented. The data collected during the run has been analyzed to measure the inclusive differential cross sections for π^0 production in interactions between 530 GeV/c incident proton and π^- beams and copper and beryllium targets.

The invariant differential inclusive cross sections for $\pi^- + \mathrm{Be}$ and $\pi^- + \mathrm{Cu}$ were measured for different rapidity and p_T intervals covering the kinematic range $3.25 < p_T < 10\,\mathrm{GeV/c}$ and $|y| < 0.7$. No significant dependence of the shape of the p_T distributions on the rapidity region was observed. Distributions as a function of rapidity were measured for four p_T intervals. These distributions were observed to peak at ~ 0.3 units of rapidity. The kinematic range for p + Be and p + Cu covered the same range as for π^-, but the transverse momentum was limited to values between 4.0 and 10 GeV/c. The p_T distributions did not show a dependence on the rapidity, and the rapidity distributions peaked at around 0.04.

Cross sections integrated and averaged over the full rapidity range ($-0.7 < y < 0.7$), were measured for the two nuclear targets for both proton and π^- data. These cross sections were used to calculate the nuclear dependence of the π^0 production, measured in terms of A^α. No real deviations from unity were found for α. The values of α measured in our kinematic range for the π^-–related processes was 1.01 ± 0.02, and for the proton case the value measured was 1.04 ± 0.03.

The ratio of the cross sections for π^- and p interactions was also measured for the range $4 < p_T < 8\,\mathrm{GeV}$ and $-0.7 < y < 0.7$. The ratio between the two cross sections was found to be larger than unity and increased with increasing p_T, in agreement with expectations based on the quark content of the proton and the π^-.

Finally, the cross sections for π^0 production in $\pi^- + \mathrm{Be}$ and $\mathrm{p} + \mathrm{Be}$ interactions was compared to QCD predictions using the leading-log approximation. In all cases, a value of 200 meV was used for Λ, and functions for two values of Q^2 were examined. For the π^- process the results indicate an agreement between QCD and the data, for $Q^2 = 0.25 P_T^2$ and $k_T = 0$ in the region $4 < p_T < 6\,\mathrm{GeV}$, although the experimental

cross section appears to decrease more rapidly with increasing p_T than the QCD predicted distribution. The results from the proton process show a good agreement with the predictions for $Q^2 = 0.25P_T^2$ and $k_T = 0.4\,\mathrm{GeV/c}$. Distributions as a function of rapidity were also compared. The shape of the distributions look very similar, but the magnitudes are in disagreement. Since the form of the momentum transfer scale is not determined by theory, one could in principle find an optimized function of Q^2 that would agree with the experimental results, but the meaning of such optimization perhaps would not be very clear. Once higher order corrections are available, the dependence of the functions on Q^2 will be more constrained and the meaning of the choice of the Q^2 dependence more obvious.

REFERENCES

1. J. F. Owens, *Rev. of Mod. Phys.* **59** (1987), 465.
2. H. Boggild, T. Ferbel, *Annual Review of Nuclear Science* **24** (1974), 451.
3. E. L. Berger, E. Braaten and R. D. Field, *Nucl. Phys.* **B239** (1984), 52-92.
4. T. Ferbel and W. R. Molson, *Rev. Mod Phys.* **56** (1984), 181.
5. T. Ferbel, Proceedings of Physics in Collision, Capri, (1988).
6. J. Huston, "The Production of High p_T Photons and Lepton Pairs", (1990)
7. I. Kourbanis, "The A–dependence of Leading Particle Production by 800 GeV Protons", PhD dissertation, Northeastern University (1989).
8. E. Engels Jr. *et al.*, *NIM* **A226** (1984), 59-62, *NIM* **A253** (1987), 523-529.
9. ZIPTRAK Manual, FNAL Computing Department, publication PN267.0
10. K. Hartman, "Hadronic Production of π° Pairs and Associated Event Structure", PhD Dissertation, Pennsylvania State University (1989).
11. CAMAC Instrumentation and Interface Standards, IEEE 1982, ISBN 0-471-89737-X.
12. W. E. Desoi, "Construction and Operation of a Liquid Argon Calorimeter for Use in Experiment E–706 at the Fermi National Accelerator Laboratory", PhD Dissertation, University of Rochester (1990).
13. J.Huston *et al.*, "Performance of a Large Liquid Argon Calorimeter for Measurement of the Position, Energy and Direction of Electromagnetic Showers at High Luminosities", submitted to XXIV International Conference on High Energy Physics.

14. C. Lirakis, "A Study of High Transverse Momentum η production in 530 GeV/c Hadronic Interactions", PhD Dissertation, Northeastern University, (1989).

15. G. Fanourakis, "Direct Photon Studies, Current Status of Experiment E706 (Fermilab)", E706 internal note # 164, Jan 26,1988.

16. E. Prebys and F. Lobkowicz, "High Voltage Dependance of Signals in the LAC", E706 internal note # 163, Oct 5,1989.

17. D. Skow, "A Study of η Meson Production at 530 GeV/c", PhD Dissertation, University of Rochester, (1990).

18. R. Benson, "Characteristics of Forward Energy Production in Proton–Nucleus and Pion-Nucleus Collisions at $\sqrt{S} = 31.5\,\mathrm{GeV}$", PhD Dissertation, University of Minnesota, (1990).

19. VAXONLINE System,FNAL Computing Department, publication PN252.

20. Bison Interrupt and Gate Control, FNAL Computing Department, publication HN-3.2.

21. H. J. Klein and J. Zoll, PATCHY reference manual, CERN Computer Centre program library, Oct. 1983.

22. R. Brun, M. Goossens and J. Zoll, ZEBRA user guide, CERN Computer Centre program library DD/EE/85-6.

23. J. Zoll, ZEBRA reference manuals, CERN Computer Centre program library.

24. A. Sinanidis, "Particles Produced in Association with High Transverse Momentum Single Photons and π°s in Hadronic Collisions", PhD Dissertation, Northeastern University, (1989).

25. S. Easo, "Structure of Events Containing Direct Photon or Neutral Pion in Hadronic Interactions", PhD Dissertation, Pennsylvania State University, (1989).

26. S. Mani, private communication.

27. J. P. Mansour, "High Transverse Momentum π° Production from π^{-} and p beams at 530 GeV/c on Be and Cu", PhD Dissertation, University of Rochester, (1989).

28. R. Brun, F. Bruyant, M. Maire, A. C. McPherson and P. Zanarini, GEANT3 User's guide, CERN Data Handling Division, DD/EE/84-1, 1987.

29. Eric J. Prebys, "A Study of High Transverse Momentum Direct Photon Production from Copper and Beryllium Targets with 530 GeV/c Incident π^{-} and Proton beams", PhD Dissertation, University of Rochester, (1990)

30. R. Brun, F. Bruyant, M. Maire, A. C. McPherson and P. Zanarini, GEANT3 User's Guide, CERN Data Handling Division,DD/EE/84-1, 1987

31. J. P. Mansour, private communication

32. D. W. Weerasundara, private communication.

33. D. W. Duke and J. F. Owens, *Phys. Rev. D* **30** (1984), 49.

34. J. F. Owens, *Phys. Rev. D* **30** (1984), 943.

35. J. F. Owens, *Phys. Rev. D* **19** (1979), 3279.

VITAE

The author was born in Medellin, Colombia, on May 20, 1960. He began undergraduate studies at the Universidad Nacional in Bogota, Colombia, and received the Bachelor of Science degree in Physics and Mathematics from Austin Peay State University in 1983. He commenced his graduate work at Northeastern University in 1983 and received a Master of Science degree in 1985. During his graduate work, the author has received support from teaching and research assistanships, and has been at Fermilab since 1985.